# ABSTRACT

LI, XIN. A Quantum Monte Carlo Study of Atomic Fermi Gas. (Under the direction of Lubos Mitas.)

Quantum Monte Carlo provides a powerful and accurate numerical strategy to study the many-body physics, with its well known accuracy to the treatment of correlation which is most of the time not accessible to the analytical calculation for the strongly correlated system. Diffusion Monte Carlo is very accurate in treating the system ground state properties, with the only approximation being the fixed-node approximation. The success of the experimental availability of cold atom gas and tunable interaction through Feshbach resonance developed in recently years has provided great opportunities for studies of the many-body effect and correlation in these systems. Diffusion Monte Carlo is very suitable to study the ground state property of the atomic Fermi gas system with varying geometry, interaction strength and external potential and make direct comparisons with experiments and to test our understanding of fundamental theories for these systems.

After the introduction of basic concept and theory of quantum Monte Carlo and atomic Fermi gas system, we study the two component atomic Fermi gas at unitary limit in the periodic box using variational and diffusion Monte Carlo methods. By tuning the scattering length to infinity and extrapolating the effective range of the interacting potential close to zero, we find the Bertsch parameter drops approximately 5% compared to the previous Monte Carlo study without the effective range extrapolation. To examine the size of the fixed-node error, we also carried out released-node diffusion Monte Carlo calculations. We find the fixed-node error for the smallest system of four atoms is marginal. We calculate the ground state properties for a larger system of sixty-six atoms. We calculate pair correlation function and one-body and two-body density matrices, from which we extract the condensate fraction. We find that more than half of the atoms are involved in pairing. We also analyse the nodal surface properties for the system in BCS, unitary and BEC regime and extract Tan's constant from calculated results.

After the calculation of atomic Fermi gas in the periodic box, we extend our simulation in isotropic and anisotropic harmonic traps. We elucidate the discrepancies between calculations from various simulation results in the literature for the atomic Fermi gas in isotropic harmonic traps. Furthermore, we study the ground state energy, density profile and nodal surface properties for the atomic Fermi gas in both isotropic and squeezed harmonic traps. We find the Bertsch parameter in the isotropic trap to be 0.65(1) and for the squeezed trap $\omega_\perp/\omega_z = 1/25$ to be 0.70(1). Our results can be compared with experimental data and used as benchmark for cold atom experiments with similar set up.

© Copyright 2012 by Xin Li

All Rights Reserved

A Quantum Monte Carlo Study of Atomic Fermi Gas

by
Xin Li

A dissertation submitted to the Graduate Faculty of
North Carolina State University
in partial fulfillment of the
requirements for the Degree of
Doctor of Philosophy

Physics

Raleigh, North Carolina

2012

APPROVED BY:

| | |
|---|---|
| Dean Lee<br>Co-chair of Advisory Committee | Kazufumi Ito |
| Thomas Schaefer | Lubos Mitas<br>Chair of Advisory Committee |

## DEDICATION

To my parents: Li, Delin and Mao, Juxiang

# BIOGRAPHY

The author was born in Wuwei, a small town in An'hui province in south-east China in 1983. Since 1986, he had been raised in Urumuqi, Xinjiang province in north-west China, where he attended No. 57 Junior School, No. 12 Middle School and No. 1 Middle School. The author received B.S. degree in physics in Peking University, Beijing in 2005, and M.S. and M.A. degrees in physics and statistics in North Carolina State University, Raleigh in 2007 and 2008. The author finished his Ph.D. in physics in 2012.

## ACKNOWLEDGEMENTS

First, I would like to thank my advisers Prof. Lubos Mitas and Prof. Dean Lee for their enthusiastic guidance and support over such a long period of time. This thesis would never exist without their supervision and help. I am grateful for countless discussions with Dr. Mitas when I learned so many new things and for the suggestions and opinions for almost every details of my research. I am deeply influenced by the way how Dr. Mitas approaches a new problem and builds the solution from the scratch, and I hope I would do the same in my future study. I am grateful for Dr. Lee for picking the subject to study for me in which he definitely knew the opportunity to make advancement. And I benefit tremendously from numerous discussions with him for his insight and clear way of thinking.

I would like to thank Prof. Thomas Schaefer and Prof. Kazufumi Ito for being my committee members and for suggestions and comments for the improvement of my work, which are of great importance to gain further insight on the subject of study and which make this thesis much better than its original form.

I would like to thank every member in our quantum Monte Carlo group, in Center for High Performance Simulation (CHiPS) and in Physics Department, North Carolina State university, for providing an environment that stimulates conversation and discussion. Especially, I would like to thank former post-docs in our group, Dr. Jindrich Kolorenc, for various discussion on the subject of the quantum Monte Carlo in general and for teaching me many technical details of the simulations. I also thank Dr. Michal Bajdich for helping me understand the structure of the Pfaffian wave function code and for figuring out many bugs in my own code which I had a really hard time to dig out.

Finally, I would like to thank my parents. None of my achievement would ever be possible without their constant encouragement, support and love.

# TABLE OF CONTENTS

**List of Tables** . . . . . **vii**

**List of Figures** . . . . . **viii**

**Chapter 1 Introduction** . . . . . **1**
1.1 Atomic Fermi gas experiments . . . . . 3
1.2 BCS-BEC Crossover and Unitary limit . . . . . 4
1.2.1 Unitary limit and the Bertsch parameter . . . . . 5
1.2.2 A brief review of BCS theory . . . . . 7

**Chapter 2 Quantum Monte Carlo methods** . . . . . **13**
2.1 Metropolis algorithm . . . . . 13
2.2 Variational Monte Carlo . . . . . 15
2.3 Diffusion Monte Carlo . . . . . 17
2.3.1 Fixed-node approximation . . . . . 18
2.3.2 Fixed-node diffusion Monte Carlo with importance sampling . . . . . 19
2.3.3 Released-node diffusion Monte Carlo . . . . . 22
2.4 Reptation Monte Carlo . . . . . 25
2.5 Wave functions, observables and estimators . . . . . 28
2.5.1 Trial wave functions . . . . . 28
2.5.2 Mixed, Pure and Growth Estimators . . . . . 33
2.5.3 Pair correlation function . . . . . 35
2.5.4 One-body and two-body density matrices . . . . . 36
2.6 Optimization method . . . . . 41
2.7 Summary . . . . . 43

**Chapter 3 Theory of unpolarized Fermi gas** . . . . . **44**
3.1 Two-body scattering . . . . . 44
3.1.1 General theory . . . . . 44
3.1.2 Scattering of Pöschl-Teller potential . . . . . 46
3.2 Equation of state for BCS and BEC regime . . . . . 46
3.3 Fermi gas in the harmonic trap . . . . . 47
3.3.1 Ideal Fermi gas in the harmonic trap . . . . . 47
3.3.2 Interacting Fermi gas in the harmonic trap . . . . . 49
3.4 Summary . . . . . 50

**Chapter 4 QMC study of unpolarized Fermi gas at Unitary limit** . . . . . **52**
4.1 Simulation setup . . . . . 52
4.2 QMC results . . . . . 53
4.2.1 Ground state energy . . . . . 53
4.2.2 Released-node DMC results for 4 and 14 unpolarized atoms . . . . . 59
4.2.3 Pair correlation function . . . . . 62

4.2.4 One-body, two-body density matrices and condensate fraction . . . . . 64
4.2.5 Nodal surface of BCS, unitary limit and BEC results . . . . . 67
4.3 Extraction of Tan's constant . . . . . 67
4.4 Conclusion . . . . . 69

**Chapter 5 Unpolarized Fermi gas in isotropic and anisotropic harmonic traps 71**
5.1 Simulation setup . . . . . 72
5.2 QMC results . . . . . 73
5.2.1 Four-atom system results . . . . . 73
5.2.2 Energy . . . . . 73
5.2.3 Density profile . . . . . 77
5.2.4 Nodal surface . . . . . 81
5.3 Conclusion . . . . . 81

**Chapter 6 Summary and future work . . . . . 85**
6.1 Summary . . . . . 85
6.2 Future work . . . . . 86

**References . . . . . 88**

**Appendices . . . . . 93**
Appendix A Conversion factor table for unpolarized Fermi gas . . . . . 94
Appendix B Energy of non-interacting Fermi gas in isotropic and anisotropic harmonic traps . . . . . 96

# LIST OF TABLES


Table 1.1 The Bertsch parameter $\xi$ from both experimental measurements and numerical calculations. . . . . 8

Table 4.1 Effective range extrapolation of Bertsch parameter from DMC results for 4, 14, 38 and 66 atoms . . . . . 56

Table 5.1 DMC energies of unpolarized Fermi gas in isotropic harmonic traps with atom number N and varing effective range. Energies are in unit of $\omega_z$. . . . 74

Table 5.2 Energies of unpolarized Fermi gas in isotropic harmonic traps with atom number N and effectivive range extrapolated energy results $E_{\text{ext}}$, previous DMC and Lattice results(quoting the absolute value of the errorbars) and correlated Gaussian(CG) results. Energies are in unit of $\omega_z$. . . . . 75

Table 5.3 Energies of unpolarized Fermi gas in anisotropic harmonic trap with atom number N and effective range extropolated energy $E_{\text{ext}}$ with frequency ratio $\omega_\perp/\omega_z = 1/\sqrt{30}$. Energies are in the unit of $\omega_z$. . . . . 75

Table 5.4 Energies of unpolarized Fermi gas in anisotropic harmonic trap with atom number N and effective range extropolated energy $E_{\text{ext}}$ with frequency ratio $\omega_\perp/\omega_z = 1/30$. Energies are in the unit of $\omega_z$. . . . . 75

Table 5.5 Energies of unpolarized Fermi gas in anisotropic harmonic trap with atom number N and effective range extropolated energy $E_{\text{ext}}$ with frequency ratio $\omega_\perp/\omega_z = 1/25$. Energy are in the unit of $\omega_z$. . . . . 76

Table A.1 Conversion factor for unpolarized Fermi gas. For simplicity, the calculation is performed in a periodic box with size $L = 1$ . . . . . 95

Table B.1 Energy of N non-interacting unpolarized Fermi atoms in isotropic harmonic trap ($\hbar = 1$, $\omega_x = \omega_y = \omega_z = \omega$). . . . . 97

Table B.2 Energy of N non-interacting unpolarized Fermi atoms in anisotropic harmonic trap ($\hbar = 1$, $\omega_x = \omega_y = \omega_\perp \ll \omega_z$). . . . . 97

# LIST OF FIGURES

Figure 1.1 The two channel model for Feshbach resonance[32]. The resonance happens when two atoms collides in the open channel resonantly couple to the closed channel with bound state energy $E_c$, which can be magnetically tuned. . . . . 4

Figure 1.2 Scattering length dependence of the magnetic field for $^6$Li. The broad Feshbach resonance occurs at $B_0 \approx 834G$[18], and a narrow Feshbach(not shown in the graph) occurs at $B_0 \approx 543G$. . . . . 5

Figure 1.3 Graphic illustration of the BCS-BEC crossover. On the left side is the weakly interacting BCS regime, where the weak interaction doesn't admit a bound state for two atoms and the s-wave scattering length $a_s$ is negative. The size of weakly attracted atoms with opposite spin and momentum is much larger than the interparticle spacing $r_s$. In the middle is the unitary limit, where two atoms are just start to bound and $a_s \to \infty$, the system loses all the length scale except for $r_s$. The right side is the BEC rigem, where the atoms with different spins form tightly bounding molecules. The depth of the potential and therefore the strength of the interaction is controlled through the magnetic field in Feshbach resonance, as shown in Figure 1.2. . . . . 6

Figure 1.4 The quasi-particle excitation spectrum for a normal state and BCS superfluidity state. The left part is the normal state without the gap, and the right part is the superfluid state, with the quasi-particle pairing gap $\Delta$, formed by the attractive interaction. . . . . 12

Figure 2.1 An illustration of released-node method. Originally all the walkers with positive sign and negative sign are restricted in their respective nodal pocket, and the energy is the same as bosonic system with the same node constrains, as shown on the upper panel of the graph. As the released-node process starts, the original nodal surface opens up gaps and walkers can now pass through different nodal pockets. During this process, which eventually projects to the bosonic ground state of the system, the fermionic signal can be picket up. . . . . 23

Figure 2.2 A graphic illustration of the RMC method. The dots represent sampling points in the RMC method. In the sampling process, randomly pick one direction(as illustrated on the graph), propose the move and if accepted, delete the sampling on the other end, and add the new sampling point in the selected direction in front of the old point. . . . . 27

Figure 4.1 The ground state and first excited state in a periodic box using direct diagonalization method. $f_1(r)$ is the ground state and $f_2(r)$ is the first excited state. The three curves for each state represents (100), (110) and (111) direction in the box. The solution converges as the number of basis sets($\sin(r)$ and $\cos(r)$) increase up to 30000. . . . . 54
Figure 4.2 Optimized pair orbitals of $\phi_a$ and $\phi_b$ for construction of BCS wave function, the left panel shows the two pairing orbitals normalized in the head part, while the right panel shows the pair orbitals normalized from the tail part. . . . . 55
Figure 4.3 VMC and DMC calculation for the four-atom system using different pair orbitals and with or without Jastrow factor. The three wave functions yield almost identical DMC energy, indicating the accuracy of the calculation is very high. The statistical error bars are smaller than the symbol size. . . . . 56
Figure 4.4 Three independent methods used for calculation $\xi_{2,2}$[17]. Upper left panel is the linear extrapolation of the effective range of the DMC results for the unpolarized four- atom system, by extrapolating the effective range of the potential to 0, the Bertsch parameter of four-atom system is found to be 0.212(2). Upper right panel is the results from direct diagonalization of Hamiltonian, which yields results of 0.211(2) and 0.210(2). Lower left panel is the results of the lattice Monte Carlo results, which gives result 0.206(9). . . . . 57
Figure 4.5 Linear extrapolation of the effective range of the DMC results for 4, 14, 38 and 66 atoms. By extrapolating the effective range of the potential to 0, $\xi_{2,2}, \xi_{7,7}, \xi_{19,19}, \xi_{33,33}$ are found to be 0.212(2), 0.407(2), 0.409(3), 0.398(3) respectively. . . . . 58
Figure 4.6 The pair orbitals and FN-DMC and RN-DMC energies of the 4-atom unitary system with $R_{\text{eff}}/r_s = 0.06397$. The upper row shows the pair orbitals with the lowest (left), intermediate (middle) and optimal (right) accuracy with regard to the variational optimization. The lower row shows the corresponding DMC energies as functions of the projection time starting from the variational estimate. Note that the resolution of the left and right panels differs by an order of magnitude. The vertical grey lines indicate the instant of the nodal release. . . . . 59
Figure 4.7 Evolution of the DMC energies for the 14-atom system with the best optimized BCS-Jastrow wave function(left) and Slater-Jastrow wave function(right). The runs are for $R_{\text{eff}}/r_s = 0.2$. For the BCS-Jastorw wave function, no statistically significant energy drop is observed after the nodal release that is indicated with the vertical dotted line. For the Slater-Jastrow function, the RN-DMC drops are significant, the parameter $\xi_{7,7}$ drops by $\approx 0.015$ within $E_F t \approx 0.2$ after the nodal release. . . . . 61

Figure 4.8 Pair correlation function for unpolarized 66 atom system with $R_{\text{eff}}/r_s = 10$, the left panel is the same spin pair correlation function $g^{\uparrow\uparrow}(r)$ and the right panel is the opposite spin pair correlation function $g^{\uparrow\downarrow}(r)$. The results indicate effective range extropolation has little effect on $g^{\uparrow\uparrow}(r)$, and there's enhancement at short distance $r \approx 0$ for $g^{\uparrow\downarrow}(r)$ with smaller effective interaction range. . . . . 63
Figure 4.9 The one-body density matrix for 66 atoms calculated from the FN-DMC mixed estimator, the one-body density matrix change relatively small with respect to the effective range extrapolation. . . . . 65
Figure 4.10 The two-body density matrix for 66 atoms calculated from the FN-DMC mixed estimator. The condensate fraction converges to 0.56(1) for $R_{\text{eff}}/r_s \leq 0.05$ for the effective range extrapolation. . . . . 66
Figure 4.11 Three-dimensional subsets of the nodal hypersurfaces for three types of wave functions and corresponding phases in the 14-atom system. The node is obtained by scanning the simulation cell with a pair of spin-up and spin-down atoms sitting on the top of each other while keeping the rest of the atoms at fixed positions (tiny spheres). From the left to the right, the columns show the nodal surfaces of the wave functions corresponding to the free Fermi gas, the unitary limit and the BEC side of the crossover. The lower row displays the same surfaces rotated by 45 degrees around the $z$-axis. . . . . 68

Figure 5.1 DMC energy of unpolarized four-atom system in harmonic trap with two different trial wave function with effective range of the interaction extrapolated to zero. The extrapolated Bertsch's parameter reads 0.629(1). 74
Figure 5.2 Energy v.s. number of atoms for the unpolarized Fermi gas in isotropic harmonic trap. The data is listed in Table 5.2. The DMC calculation results shows clear improvement over previous ones due to better choice of wave function. . . . . 76
Figure 5.3 Bertsch parameter $E/E_{\text{NI}}$ for unpolarized Fermi gas at unitary limit in isotropic and anisotropic harmonic trap. . . . . 78
Figure 5.4 Density profile for unpolarized Fermi gas in isotropic harmonic trap. 'NI' stands for the non-interacting density profile, 'Unitary' for the density profile at unitary limit. The solid line is from QMC simulation and the dashed line is from the LDA. . . . . 79
Figure 5.5 Projected density profile for unpolarized Fermi gas in isotropic and anisotropic harmonic traps. 'NI' stands for non-interacting density profile, shown as the solid line. 'Unitary' stands for the unitary limit density profile, shown as the dashed line. The densities are projected onto the x-y plane. . . . . 80
Figure 5.6 The nodal surface for non-interacting and unitary Fermi gas in isotropic harmonic trap. The figures on the left are for the non-interacting Fermi gas, and the figures on the right are for the unitary Fermi gas. The lower panel are the same graphs rotated by 45 degrees along z-axis. . . . . 82

Figure 5.7 The nodal surface for non-interacting and unitary Fermi gas in anisotropic harmonic trap with $\omega_\perp/\omega_z = 1/\sqrt{30}$. The figures on the left are for the non-interacting Fermi gas, and the figures on the right are for the unitary Fermi gas. The lower panel are the same graphs rotated by 45 degrees along z-axis. . . . . 83
Figure 5.8 The nodal surface for non-interacting and unitary Fermi gas in anisotropic harmonic trap $\omega_\perp/\omega_z = 1/25$. The figures on the left are for the non-interacting Fermi gas, and the figures on the right are for the unitary Fermi gas, The lower panel are the same graphs rotated by 45 degrees along z-axis. Due to a weaker constrain on the x-y plane, the gas extended further on x-y plane compared with Fig. 5.7, as can be identified by the larger range of the nodal surface in the box. . . . . 84

# Chapter 1

# Introduction

The discovery of fermionic systems and illumination of their properties accompany some of the most wonderful advancements in physics in the past century. These systems can exhibit a variety of phases and properties with different nature of interaction (such as attractive or repulsive, short range or long range) in different dimensions (1D, 2D or 3D) and span across many subfield of physics. Seeking both qualitative and quantitative description and understanding of the fermionic system would therefore be crucial to advance our understanding of the basic laws of nature.

The basic theoretical framework for the weakly interacting fermionic system is the celebrated Landau-Fermi liquid theory[54, 55, 56]. The success of the theory has been verified experimentally in various systems such as conduction by electrons in simple metals or properties of normal phase of liquid $^3$He. By introducing the concept of quasiparticle in Fermi liquid theory, which transform the interacting particle system to an almost non-interacting quasi-particle system, one can label the quasiparticles with the same quantum number such as momentum $\mathbf{k}$ and spin $\sigma$, and the system ground state properties such as ground state energy or transport properties such as electric or thermal conductivity are then determined by the behavior of these quasi-particles.

The idea of Fermi liquid theory is valid when the quasiparticle life time is much longer than the typical time scale of the interaction. However, for various strongly interacting or strongly correlated systems, these criteria will not be satisfied. For example, when interaction is attractive, the particles near the Fermi surface instead of interacting weakly and being stable, will start to form Cooper pairs and the resulting ground state will become superfluid or superconductor. Such phases have been found in superfluid $^3$He[68], high Tc superconducting metals[13], and in recent 10 years, the atomic Fermi gas[51, 67], which result in much broader interests due to their connections to both condensed matter physics and to nuclear and high energy physics, which hypothesize about the existence of superfluid nuclear matter[35] and color superfluidity

in dense quark matter[3].

Due to the feasibility of tuning the interaction between different components in the trapped atomic Fermi gas through Feshbach resonance[40, 41], a thorough understanding of the atomic Fermi gas will hopefully shed new lights on our understanding of superconductivity and superfluidity for the fermionic systems in general. The usefulness of the Fermi gas lies in the fact that all the parameters like temperature, density, interaction strength are tunable. Hence, they became "Physical labs" for various fermionic systems that people are interested in. In this thesis, we are especially interested in the ground state properties of such Fermi systems including energy, density profile, momentum distribution, etc. Besides the quantities that can be measured explicitly in the experiment, we will also explore the nodal surface features of the ground state wave functions, through which the high accuracy of the calculated results will be further analyzed.

The structure of thesis will be organized as follows.

1. In the rest of the introduction, we will discuss some basic facts about atomic gas experiments, followed by a short introduction of the BCS-BEC crossover and unitary limit. We will also summarize various methods and results for the Bertsch's parameter and include a short introduction of the standard BCS thoery. BCS theory replaces the Fermi liquid thoery for atomic gas experiments and it is also the starting point of our simulations.

2. In Chpater 2, we will review the major tool for numerical simulation of the atomic Fermi gas: Quantum Monte Carlo. Following the discussion, the main algorithms of variational Monte Carlo(VMC), diffusion Monte Carlo (DMC) and reptation Monte Carlo(RMC) and the basic idea of Released-node diffusion Monte Carlo(RN-DMC) will be introduced. The observables that are collected by the Monte Carlo algorithm, such as pure and mixed estimator, will be discussed. Various zero temperature quantity such as pair correlation function, momentum distribution function, one-body, two-body density matrices and condensate fraction will also be defined.

3. In Chapter 3, we will give a brief introduction of the physics of the BCS regime and BEC regime as well as BCS-BEC crossover. After introducing the simple two-body interaction concept such as scattering lengths and phase shifts, we will cover the mean-field approximate equation of state and density profiles for these regimes. These quantities will be compared with our simulation results.

4. In Chapter 4, we will present results for the unpolarized Fermi gas in a box with periodic boundary conditions. By extrapolating the effective range of the interaction to zero, we are able to get energy lower than previous reported studies based on similar Monte Carlo techniques. We therefore emphasize the fact that in order for the system to be in the

unitary limit, the extrapolation of the effective range to zero is important. Furthermore, we present released-node diffussion Monte Carlo results for the four-atom and fourteen-atom systems. The four-atom released-node results further support the fact that the wave function and energy for our four-atom system is very accurate. For a larger system with 66 atoms, We calculated the pair correlation function and one-body and two-body density matrices, and we estimate momentum distribution function and condensate fraction from them. We also extract Tan's constant from one-body density matrix and pair correlation function.

5. In Chapter 5, we will show the results of simulations for the unpolarized Fermi gas in a box with both isotropic and anisotropic harmonic traps. We have solved the discrepancy of the ground state energy among previous studies for the unpolarized Fermi gas in isotropic harmonic traps by pointing out that the flexibility in one-body part of the wave function is crucial to fix the density near the edge of the trap, and the effective range extrapolation proved again important to get lower energy. We extend the simulation in anisotropic harmonic traps and calculate the ground state energies and density profiles for the non-interacting and unitary Fermi gas. We also illustrate the nodal surface for the system in both isotropic and anisotropic harmonic traps.

6. Finally, we conclude our work in the last chapter, ouline possible future work and discuss future advances.

## 1.1 Atomic Fermi gas experiments

The first cold atom gas experiments for Fermions were performed in 1999[36], following the realization of Bose-Einstein condensates (BEC) in 1995[34]. For the ultra-cold Fermi gas system, the most charming achievement is the realization of tuning s-wave scattering length by changing an external magnetic field through Feshbach resonance. By controlling the interaction strength and scattering length, the system can cross from the weakly interacting Bardeen-Cooper-Schrieffer(BCS) regime, where there are weakly bound Cooper pairs among atoms with opposite wave vector, to the strongly interacting BEC regime, where the atoms with different spins bound together and form a BEC condensate.

The basic idea of Feshbach resonance can be found in Ref. [32]. When the bound molecule state in the closed channel energetically approaches the scattering state in the open channel, as is shown in Figure 1.1, the Feshbach resonance is achieved. The energy difference can be controlled by tuning the magnetic field.

The Feshbach resonance can then be described by a relationship between the scattering

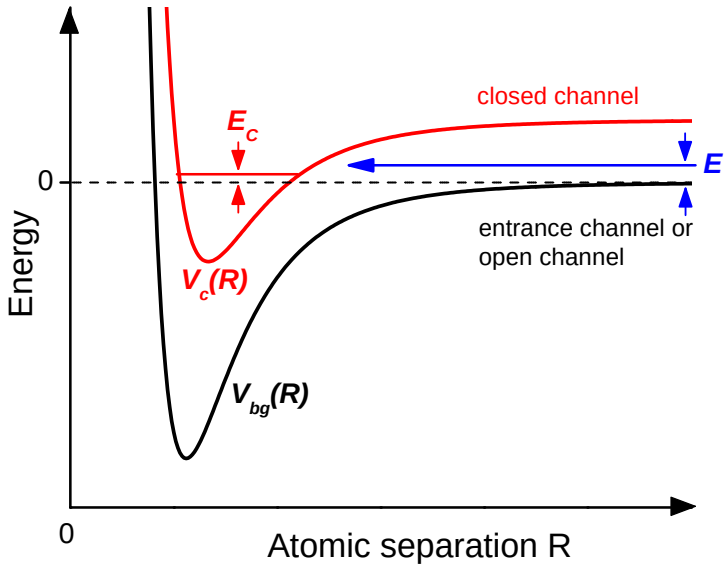


Figure 1.1: The two channel model for Feshbach resonance[32]. The resonance happens when two atoms collides in the open channel resonantly couple to the closed channel with bound state energy $E_c$, which can be magnetically tuned.

length and magnetic field[63],

$$a_s = a_{bg}(1 - \frac{\Delta_B}{B - B_0}), \tag{1.1}$$

where $B_0$ denotes the position of resonance and $\Delta_B$ is the width of the resonance. $a_{bg}$ is the background scattering length away from the resonance. In general, the interaction range is much smaller than the de Broglie wavelength or the interparticle distance $r_s$. In the vicinity of the resonance, the scattering length diverges as $a_s \to \pm\infty$. The system then loses its length scale, the so called *unitary limit*. The dependence of scattering length on the magnetic field for a broad Feshbach resonance of $^6$Li is shown in Figure 1.2.

## 1.2 BCS-BEC Crossover and Unitary limit

BCS theory is an established microscopic theory for superconductivity and superfluidity proposed by Bardeen, Cooper and Schrieffer[33, 9, 10]. When a weak attractive interaction is introduced in a fermionic system, the Fermi surface is unstable against forming weakly bound Cooper pairs. On the other hand, if the attractive interaction is strong and the Fermions with opposite spin start to form tightly bound dimers, a macroscopic number of these composite bosons will condense to the ground state, forming the so called Bose-Einstein condensate(BEC).

Thanks to the success of realizing the atomic Fermi gas with tunable s-wave interaction

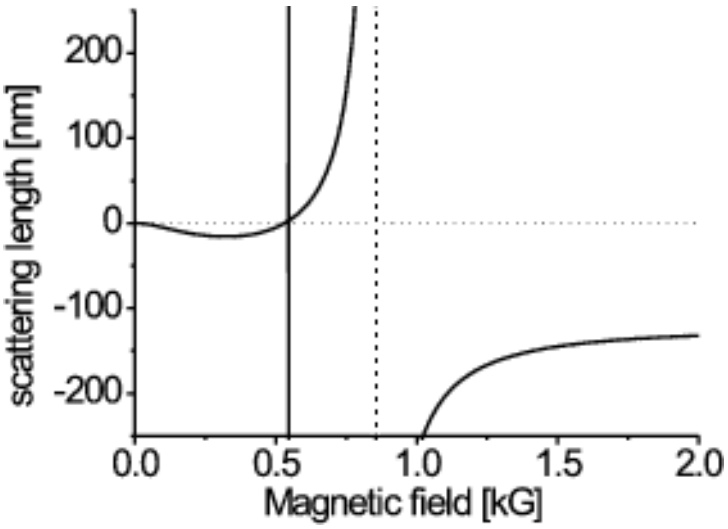


Figure 1.2: Scattering length dependence of the magnetic field for $^6$Li. The broad Feshbach resonance occurs at $B_0 \approx 834G$[18], and a narrow Feshbach(not shown in the graph) occurs at $B_0 \approx 543G$.

through the Feshbach resonance, the idea of a smooth crossover from the BCS regime to the BEC regime, the so called BCS-BEC crossover[47, 16], as illustrated in Figure 1.3, has been realized for two component Fermi gas system. By tuning the interaction strength, hence also the scattering length $a_s$, the system changes smoothly from weakly pairing Cooper pairs, where $a_s$ is negative to the condensation of composite bosons, where $a_s$ is positive.

### 1.2.1 Unitary limit and the Bertsch parameter

When the two body s-wave scattering length is tuned precisely to infinity and the effective interaction range is tuned to zero, i.e., two body interaction replaced by a contact interaction with infinite scattering length, the system enters into a strongly interacting regime, the so called unitary limit. In the unitary limit, the s-wave scattering phase shift

$$\delta_s = \frac{\pi}{2}, \tag{1.2}$$

and the s-wave scattering cross section achieved its maximum value

$$\sigma_s(k) = \frac{4\pi}{k^2}, \tag{1.3}$$

where $k$ is the momentum of the incident atom.

In the unitary limit, there's essentially no length scale except for the interparticle spacing

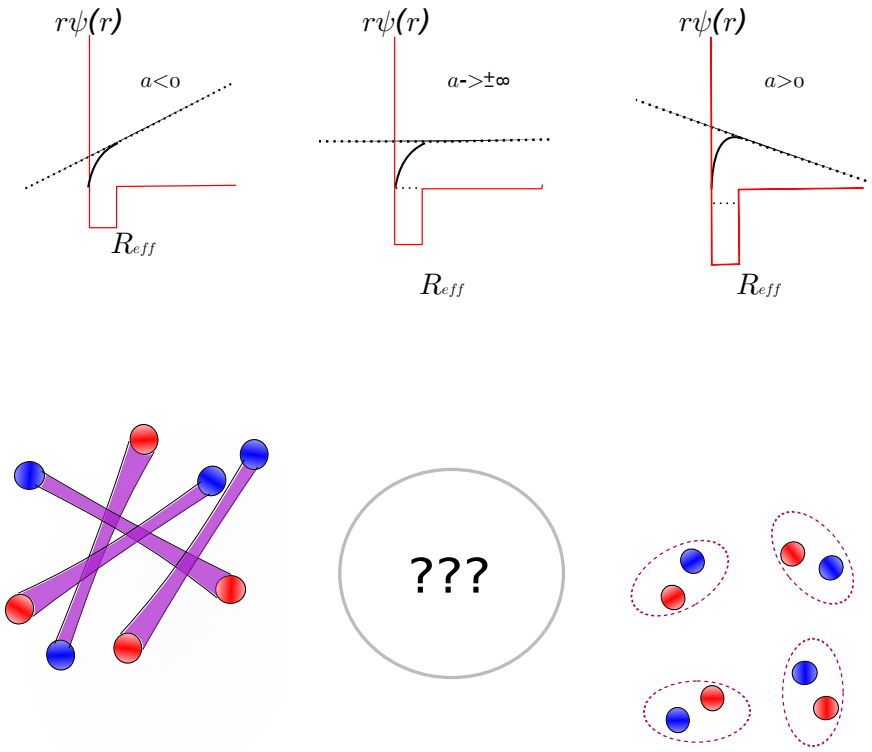


Figure 1.3: Graphic illustration of the BCS-BEC crossover. On the left side is the weakly interacting BCS regime, where the weak interaction doesn't admit a bound state for two atoms and the s-wave scattering length $a_s$ is negative. The size of weakly attracted atoms with opposite spin and momentum is much larger than the interparticle spacing $r_s$. In the middle is the unitary limit, where two atoms are just start to bound and $a_s \to \infty$, the system loses all the length scale except for $r_s$. The right side is the BEC rigem, where the atoms with different spins form tightly bounding molecules. The depth of the potential and therefore the strength of the interaction is controlled through the magnetic field in Feshbach resonance, as shown in Figure 1.2.

$r_s$, and the energy is expected to be proportional to the energy of a non-interacting gas, $E_{\text{free}}$ subject to the same boundary conditions,

$$E = \xi E_{\text{free}}. \tag{1.4}$$

The parameter $\xi$ is a universal constant called the Bertsch parameter. It is of great interest to determine what is the exact value of this parameter. A lot of studies have been conducted to evaluate $\xi$ experimentally using $^6$Li and $^{40}$K by investigating the expansion rate of atomic cloud and the sound propagating in it, and numerically by path integral Monte Carlo, diffusion Monte Carlo and lattice simulation. There are also analytical calculations such as the saddle point and variational approximations, mean-field theory with pairing, dimensional expansion and large N expansion. Table 1.1 provides a list of $\xi$ estimated by experiments, numerical simulations and theoretical calculations. In all of these studies, the Bertsch parameter have varied between $\approx$ 0.27–0.6. Due to the discrepancy among different methods, it is of great interest to find out the Bertsch parameter not only for describing the properties of the system, but also for benchmark and testing purposes for different methods[17].

### 1.2.2 A brief review of BCS theory

As a microscopic theory for superconductivity or superfluidity, BCS is in essence a variational approach. It constructs the wave function for the BCS Hamiltonian and determines the expansion coefficients for the condensate pairs. BCS theory is able to explain the origin of the gap and gives self-consistent equation for the order parameter and also determines critical temperature and quasiparticle density of the state[20].

The microscopic BCS theory Hamiltonian may be written as

$$H_{\text{BCS}} = \sum_{\mathbf{k}} \epsilon_{\mathbf{k}} (c^\dagger_{\mathbf{k}\uparrow} c_{\mathbf{k}\uparrow} + c^\dagger_{\mathbf{k}\downarrow} c_{\mathbf{k}\downarrow}) + \sum_{\mathbf{k}\mathbf{k}'} V_{\mathbf{k}\mathbf{k}'} c^\dagger_{\mathbf{k}\uparrow} c^\dagger_{-\mathbf{k}\downarrow} c_{-\mathbf{k}'\downarrow} c_{\mathbf{k}'\uparrow}, \tag{1.5}$$

in which $V_{\mathbf{k}\mathbf{k}'}$ is

$$V_{\mathbf{k}\mathbf{k}'} = \int d\mathbf{r} d\mathbf{r}' V(\mathbf{r}, \mathbf{r}') e^{i\mathbf{k}\cdot(\mathbf{r}-\mathbf{r}') - i\mathbf{k}'\cdot(\mathbf{r}-\mathbf{r}')}, \tag{1.6}$$

and $V(\mathbf{r}, \mathbf{r}')$ is the weak attractive interaction between spin up-and spin-down atoms with postion $\mathbf{r}$ and $\mathbf{r}'$ respectively.

In order to describe the physics of the BCS-BEC crossover, a BCS trial wave function, which intrinsicially builds two-component pairing, has been used,

$$|\Psi_{\text{BCS}}\rangle = \prod_{\mathbf{k}} (u_{\mathbf{k}} + v_{\mathbf{k}} c^\dagger_{\mathbf{k}\uparrow} c^\dagger_{-\mathbf{k}\downarrow}) |0\rangle, \tag{1.7}$$

Table 1.1: The Bertsch parameter $\xi$ from both experimental measurements and numerical calculations.

| Method | $\xi$ |
|---|---|
| Experiment[12] | 0.32(13) |
| Experiment[19] | 0.36(15) |
| Experiment[69] | 0.46(5) |
| Experiment[52] | 0.435(15) |
| Experiment[62] | 0.41(2) |
| Experiment[62] | 0.39(2) |
| Experiment[65] | 0.41(1) |
| Expreiment[81] | 0.36(1) |
| Lattice[58] (14-atom system) | 0.329(5) |
| Lattice[2, 1] | 0.292(24) |
| Lattice[21] | 0.37(5) |
| Lattice[23] | 0.375(5) |
| DMC[22] | 0.44(1) |
| DMC[4] | 0.42(1) |
| DMC[31] | 0.414(5) |
| DMC[64] | 0.4244(1) |
| DMC[43] | 0.383(1) |
| DMC(Our result) [61] | 0.398(3) |

where $|0\rangle$ is the vacuum state. $u_{\mathbf{k}}$ and $v_{\mathbf{k}}$ are complex variational coefficients that satisfy the normalization condition

$$|u_{\mathbf{k}}|^2 + |u_{\mathbf{k}}|^2 = 1 \tag{1.8}$$

In order to do calculation for the fixed number of atoms that can be used in quantum Monte Carlo, the BCS wavefunction can be projected to a fixed number of particles, by noticing that the BCS wave function can also be written as

$$\big|\Psi_{\mathrm{BCS}}\big\rangle_\theta = \prod_{\mathbf{k}} \big(|u_{\mathbf{k}}| + |v_{\mathbf{k}}| e^{i\theta} c^\dagger_{\mathbf{k}\uparrow} c^\dagger_{-\mathbf{k}\downarrow}\big)\big|0\big\rangle, \tag{1.9}$$

where $\theta$ is the phase of $u_{\mathbf{k}}$ and $v_{\mathbf{k}}$. By expanding the product we have

$$\big|\Psi_{\mathrm{BCS}}\big\rangle = C\big(\big|0\big\rangle + e^{i\theta} P^\dagger \big|0\big\rangle + e^{2i\theta} (P^\dagger)^2 \big|0\big\rangle + \cdots\big) \tag{1.10}$$

where C is some normalization constant , $P^\dagger$ is the pair projection operator,

$$P^\dagger = \sum_{\mathbf{k}} \left|\frac{v_{\mathbf{k}}}{u_{\mathbf{k}}}\right| c^\dagger_{\mathbf{k}\uparrow} c^\dagger_{-\mathbf{k}\downarrow}, \tag{1.11}$$

BCS wavefunction with a fixed number of N atoms can be projected out as

$$\big|\Psi_{\mathrm{BCS}}\big\rangle_N = \frac{1}{2\pi} \int_0^{2\pi} d\theta e^{-i\theta N/2} \big|\Psi_{BCS}\big\rangle_\theta \tag{1.12}$$

The projected BCS wave function for unpolarized two component atom with total number N then reads

$$\Psi_{\mathrm{BCS}}(\mathbf{R}) = \mathcal{A}\Big[\prod_{i,i'=1}^{N/2} \phi(\mathbf{r}_i, \mathbf{r}_{i'})\Big] = \det[\phi(\mathbf{r}_i - \mathbf{r}_{i'})]\,. \tag{1.13}$$

Here $\mathcal{A}$ represents the antisymmetrization operator. $i$ and $i'$ represent the labels of atoms with different spins, and $\phi(\mathbf{r}_i - \mathbf{r}_{i'})$ is the pair orbital between atoms in unlike spin channel.

$$\phi(|\mathbf{r}_i - \mathbf{r}_{i'}|) = \sum_{\mathbf{k}} \left|\frac{v_{\mathbf{k}}}{u_{\mathbf{k}}}\right| e^{i\mathbf{k}(\mathbf{r}_i - \mathbf{r}_{i'})}. \tag{1.14}$$

In order to determine the variational coefficient $u_{\mathbf{k}}$ and $v_{\mathbf{k}}$, we can consider solving for the mean field BCS Hamiltonian.

$$H^{\mathrm{MF}}_{\mathrm{BCS}} = \sum_{\mathbf{k}} \epsilon_{\mathbf{k}} (c^\dagger_{\mathbf{k}\uparrow} c_{\mathbf{k}\uparrow} + c^\dagger_{\mathbf{k}\downarrow} c_{\mathbf{k}\downarrow}) - \sum_{\mathbf{k}} \Delta (c^\dagger_{\mathbf{k}\uparrow} c^\dagger_{-\mathbf{k}\downarrow} + c_{-\mathbf{k}\downarrow} c_{\mathbf{k}\uparrow}) \tag{1.15}$$

in which

$$\epsilon_{\mathbf{k}} = \frac{\mathbf{k}^2}{2m}, \tag{1.16}$$

where $u_{\mathbf{k}}$ ,$v_{\mathbf{k}}$ and $\Delta$ are assumed to be real, and $\Delta$ is assumed to be $\mathbf{k}$ independent for simplicity.

The expectation value takes the form

$$\left\langle \Psi_{BCS} | H^{\mathrm{MF}}_{\mathrm{BCS}} | \Psi_{BCS} \right\rangle = \sum_{\mathbf{k}} 2\epsilon_{\mathbf{k}} v_{\mathbf{k}}^2 - 2\Delta u_{\mathbf{k}} v_{\mathbf{k}} = \sum_{\mathbf{k}} \left[ \epsilon_{\mathbf{k}} (\cos(2\theta_{\mathbf{k}} + 1) - \Delta \sin(2\theta_{\mathbf{k}}) \right], \tag{1.17}$$

where

$$u_{\mathbf{k}} = \sin\theta_{\mathbf{k}}, v_{\mathbf{k}} = \cos\theta_{\mathbf{k}}. \tag{1.18}$$

The relationship between $u_{\mathbf{k}}$ and $v_{\mathbf{k}}$

$$u_{\mathbf{k}}^2 + v_{\mathbf{k}}^2 = \sin^2\theta_{\mathbf{k}} + \cos^2\theta_{\mathbf{k}} = 1, \tag{1.19}$$

is also ensured.

In order to minimize the expectation value, we take derivative of $\theta_{\mathbf{k}}$ with respect of Eq. 1.17 and requiring it to vanish gives

$$\tan(2\theta_{\mathbf{k}}) = -\frac{\Delta}{\epsilon_{\mathbf{k}}}. \tag{1.20}$$

We solve for $u_{\mathbf{k}}$ and $v_{\mathbf{k}}$,

$$2u_{\mathbf{k}} v_{\mathbf{k}} = \frac{\Delta}{E_{\mathbf{k}}}, \tag{1.21}$$

$$v_{\mathbf{k}}^2 - u_{\mathbf{k}}^2 = -\frac{\epsilon_{\mathbf{k}}}{E_{\mathbf{k}}}, \tag{1.22}$$

where the $E_{\mathbf{k}}$ is defined as

$$E_{\mathbf{k}} = \sqrt{\epsilon_{\mathbf{k}}^2 + \Delta^2}. \tag{1.23}$$

The final results are

$$v_{\mathbf{k}}^2 = \frac{1}{2}(1 - \frac{\epsilon_{\mathbf{k}}}{E_{\mathbf{k}}}), \tag{1.24}$$

$$u_{\mathbf{k}}^2 = \frac{1}{2}(1 + \frac{\epsilon_{\mathbf{k}}}{E_{\mathbf{k}}}). \tag{1.25}$$

The full meanfield Hamiltonian can be written as

$$H^{\mathrm{MF}}_{\mathrm{BCS}} = \sum_{\mathbf{k}} \epsilon_{\mathbf{k}} (c^\dagger_{\mathbf{k}\uparrow} c_{\mathbf{k}\uparrow} + c^\dagger_{\mathbf{k}\downarrow} c_{\mathbf{k}\downarrow}) - \sum_{\mathbf{k}} \Delta_{\mathbf{k}} c^\dagger_{\mathbf{k}\uparrow} c^\dagger_{-\mathbf{k}\downarrow} - \sum_{\mathbf{k}} \Delta^*_{\mathbf{k}} c_{-\mathbf{k}\downarrow} c_{\mathbf{k}\uparrow}. \tag{1.26}$$

Here $\Delta_{\mathbf{k}}$ now has a $\mathbf{k}$ dependence and can be written as

$$\Delta_{\mathbf{k}} = -\sum_{\mathbf{k}'} V_{\mathbf{k}\mathbf{k}'} \langle c_{-\mathbf{k}'\downarrow} c_{\mathbf{k}'\uparrow} \rangle, \tag{1.27}$$

The so-called Bogoliubov transformation of $c^{\dagger}_{-\mathbf{k}\downarrow}$ and $c_{\mathbf{k}\uparrow}$ defines new operators $\gamma^{\dagger}_{-\mathbf{k}\downarrow}$ and $\gamma_{\mathbf{k}\uparrow}$,

$$\begin{pmatrix} \gamma_{\mathbf{k}\uparrow} \\ \gamma^{\dagger}_{-\mathbf{k}\downarrow} \end{pmatrix} = \begin{pmatrix} u^{*}_{\mathbf{k}} & v_{\mathbf{k}} \\ -v^{*}_{\mathbf{k}} & u_{\mathbf{k}} \end{pmatrix} \begin{pmatrix} c_{\mathbf{k}\uparrow} \\ c^{\dagger}_{-\mathbf{k}\downarrow} \end{pmatrix}. \tag{1.28}$$

The corresponding inverse transform is given by

$$\begin{pmatrix} c_{\mathbf{k}\uparrow} \\ c^{\dagger}_{-\mathbf{k}\downarrow} \end{pmatrix} = \begin{pmatrix} u_{\mathbf{k}} & -v_{\mathbf{k}} \\ v^{*}_{\mathbf{k}} & u^{*}_{\mathbf{k}} \end{pmatrix} \begin{pmatrix} \gamma_{\mathbf{k}\uparrow} \\ \gamma^{\dagger}_{-\mathbf{k}\downarrow} \end{pmatrix}. \tag{1.29}$$

If we assign $u_{\mathbf{k}}$, $v_{\mathbf{k}}$ and $E_{\mathbf{k}}$ the same values as above, the Hamiltonian $H^{\mathrm{MF}}_{\mathrm{BCS}}$ can be directly diagonalized as

$$H^{\mathrm{MF}}_{\mathrm{BCS}} = \sum_{\mathbf{k}} E_{\mathbf{k}} (\gamma^{\dagger}_{\mathbf{k}\uparrow}\gamma_{\mathbf{k}\uparrow} + \gamma^{\dagger}_{\mathbf{k}\downarrow}\gamma_{\mathbf{k}\downarrow}). \tag{1.30}$$

The most important prediction of the BCS theory is that the quasiparticles open up an excitation gap, i.e., a certain energy is required to break up condensed Cooper pairs. This can be directly seen from Eq. 1.30 and from the definition of $E_{\mathbf{k}}$, as is illustrated in Figure 1.4.

The order parameter $\Delta_{\mathbf{k}}$ can be found as

$$\begin{aligned} \Delta_{\mathbf{k}} &= -\sum_{\mathbf{k}'} V_{\mathbf{k}\mathbf{k}'} \langle c_{-\mathbf{k}'\downarrow} c_{\mathbf{k}'\uparrow} \rangle \\ &= -\sum_{\mathbf{k}'} V_{\mathbf{k}\mathbf{k}'} \left( u^{*}_{\mathbf{k}'} v_{\mathbf{k}'} \langle \gamma_{-\mathbf{k}'\downarrow} \gamma^{\dagger}_{-\mathbf{k}'\downarrow} \rangle - v_{\mathbf{k}'} u^{*}_{\mathbf{k}'} \langle \gamma^{\dagger}_{\mathbf{k}'\uparrow} \gamma_{-\mathbf{k}'\uparrow} \rangle \right) \\ &= -\sum_{\mathbf{k}'} V_{\mathbf{k}\mathbf{k}'} u^{*}_{\mathbf{k}'} v_{\mathbf{k}'} (1 - 2n(E_{\mathbf{k}'})). \end{aligned} \tag{1.31}$$

where $n(E_{\mathbf{k}'})$ is the Fermi-Dirac distribution function,

$$n(E_{\mathbf{k}'}) = \frac{1}{e^{\beta(E'_k - \mu)} + 1}. \tag{1.32}$$

The order parameter can be further calculated by making assumtions that $V_{\mathbf{k},\mathbf{k}'}$ is independent of $\mathbf{k}$ and $\mathbf{k}'$, the results is given as

$$\Delta_{\mathbf{k}} = V \sum_{k} \Delta_{\mathbf{k}} \frac{1 - 2n(E_{\mathbf{k}})}{2E_{\mathbf{k}}}. \tag{1.33}$$

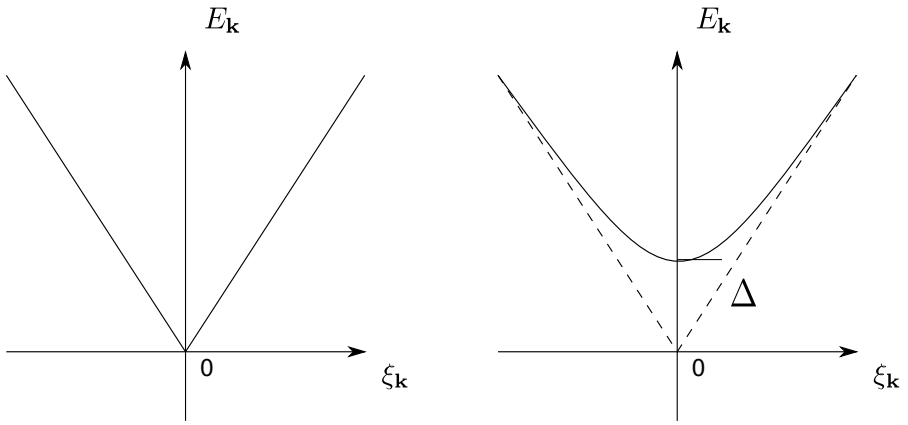


Figure 1.4: The quasi-particle excitation spectrum for a normal state and BCS superfluidity state. The left part is the normal state without the gap, and the right part is the superfluid state, with the quasi-particle pairing gap $\Delta$, formed by the attractive interaction.

After rearrangements of the equation leads to

$$1 = Vd(E_F) \int d\epsilon_{\mathbf{k}} \frac{\tanh(\beta(\sqrt{\epsilon_{\mathbf{k}}^2 + |\Delta_{\mathbf{k}}|^2}))}{2\sqrt{\epsilon_{\mathbf{k}}^2 + |\Delta_{\mathbf{k}}|^2}} \tag{1.34}$$

where $d(E_F)$ is the density of states near the Fermi surface.

Neglecting the quasiparticle interaction, the pairing gap can be approximately calculated from the energy difference of even and odd atom systems by the following formula.

$$\Delta_{\text{gap}} = E(N/2+1, N/2) - \frac{1}{2}\left[E(N/2, N/2) + E(N/2+1, N/2+1)\right]. \tag{1.35}$$

To conclude, the BCS theory provides explanation of the existence of pairing gap in the quasiparticle spectrum when there's attractive interactions between atoms with different spins. The success of BCS theory has been manifested in the various physical systems and phenomena such as superconductivity and superfluidity. The variational form of BCS wave function projected onto a given number of atoms will be used to construct the trial wave function in our DMC calculations.

# Chapter 2

# Quantum Monte Carlo methods

Quantum Monte Carlo methods provide powerful tools to tackle many-body physics problems which are generally not solvable by analytical calculations. The general idea of finding a stochastic solution for the Schrödinger equation has been utilized by a number of different quantum Monte Carlo methods. The list includes variational and diffusion Monte Carlo[44, 27], reptation Monte Carlo[11], path integral Monte Carlo[26] as well as auxiliary field Monte Carlo[15]. In this thesis, we will focus on the the first three methods, which are the major tools for extracting zero temperature ground state properties for the atomic Fermi systems that we are interested in.

This chapter gives an elementary introduction to the methods and techniques of quantum Monte Carlo. Various techniques such as projection and sampling algorithm, observable estimation and wave function optimization are discussed. These methods and techniques will serve as major tools for the study of atomic Fermi gas that is carried out in this thesis.

## 2.1 Metropolis algorithm

Many Markov Chain Monte Carlo methods use the Metropolis algorithm[66] update to get a set of sampling points $\mathbf{R}$ from a target function $P(\mathbf{R})$. The single point $\mathbf{R}$ samples the full configuration space, and the target function $P(\mathbf{R})$ is represented by a set of sampling point. In our case, $P(\mathbf{R})$ is the probability density at position $\mathbf{R}$,

$$P(\mathbf{R}) = \frac{\left|\Psi(\mathbf{R})\right|^2}{\int d\mathbf{R}\left|\Psi(\mathbf{R})\right|^2}, \tag{2.1}$$

where $\Psi(\mathbf{R})$ is the wave function.

$$\mathbf{R} = (\mathbf{r_1}, \mathbf{r_2}, \cdots, \mathbf{r_N}), \tag{2.2}$$

where $\mathbf{r}_i$ is the particle coordinate in d-dimentional space.

The Metropolis algorithm is a powerful tool to sample any given distribution without knowing its norm. This is a great advantage as sometimes the norm of a specific distribution might be too difficult to calculate. The standard Metropolis algorithm[66] consists of two steps:

- Propose a move from $\mathbf{R}_j \to \mathbf{R}_i$ according to some transfer matrix $T(\mathbf{R}_i|\mathbf{R}_j)$.
- Accept or reject the move, with the acceptance probability derived from an acceptance function $\mathcal{A}(\mathbf{R}_i, \mathbf{R}_j)$, which is in the range $[0, 1]$.

The idea of Metropolis algorithm is based on the fact that given a set of original sampling points $\mathbf{R}$, once stationary property and ergodicity property are satisfied, after equilibration, the asymptotic distribution of the sampling points should converge to the desired distribution. The stationary distribution is achieved when

$$\sum_j M(\mathbf{R}_i|\mathbf{R}_j)P(\mathbf{R}_j) = P(\mathbf{R}_i), \tag{2.3}$$

where $M(\mathbf{R}_i|\mathbf{R}_j)$ is the transition matrix that transfer the sampling points from original position $\mathbf{R}_j$ to the new position $\mathbf{R}_i$.

The condition of detailed balance, a stronger form of stationarity, can be written as

$$M(\mathbf{R}_i|\mathbf{R}_j)P(\mathbf{R}_j) = M(\mathbf{R}_j|\mathbf{R}_i)P(\mathbf{R}_i), \tag{2.4}$$

The stationarity can be recovered by summing over the $j$ index in Eq. 2.4 and by noting that

$$\sum_j M(\mathbf{R}_j|\mathbf{R}_i) = 1. \tag{2.5}$$

The Metropolis algorithm is aimed at enforcing detailed balance by breaking the transition matrix into two parts,

$$M(\mathbf{R}_i|\mathbf{R}_j) = T(\mathbf{R}_i|\mathbf{R}_j)\mathcal{A}(\mathbf{R}_i|\mathbf{R}_j), \tag{2.6}$$

The detailed balance condition can be rewritten as

$$\frac{\mathcal{A}(\mathbf{R}_j|\mathbf{R}_i)}{\mathcal{A}(\mathbf{R}_i|\mathbf{R}_j)} = \frac{T(\mathbf{R}_i|\mathbf{R}_j)P(\mathbf{R}_j)}{T(\mathbf{R}_j|\mathbf{R}_i)P(\mathbf{R}_i)}. \tag{2.7}$$

Therefore, the acceptance function of the form

$$\mathcal{A}(\mathbf{R}_j|\mathbf{R}_i) = \min\left(1, \frac{T(\mathbf{R}_i|\mathbf{R}_j)P(\mathbf{R}_j)}{T(\mathbf{R}_j|\mathbf{R}_i)P(\mathbf{R}_i)}\right), \tag{2.8}$$

can be shown to satisfy the detailed balance condition.

After the evolution reaches the equilibrium, observables can be collected. For a given operator $\hat{O}$ the expectation value is defined as

$$\langle \hat{O} \rangle = \frac{\int d\mathbf{R} O(\mathbf{R}) P(\mathbf{R})}{\int d\mathbf{R} P(\mathbf{R})}, \tag{2.9}$$

and the variance is defined as

$$\langle \sigma^2_{\hat{O}} \rangle = \frac{\int d\mathbf{R} (O(\mathbf{R}) - \langle \hat{O} \rangle)^2 P(\mathbf{R})}{\int d\mathbf{R} P(\mathbf{R})}, \tag{2.10}$$

The expectation estimator for the operator $\hat{O}$ can be written as

$$\langle \hat{O} \rangle_E = \frac{1}{N} \sum_{i=1}^{N} O(\mathbf{R}_i), \tag{2.11}$$

and the variance estimator can be written as

$$\langle \sigma^2_{\hat{O}} \rangle_E = \frac{1}{N-1} \sum_{i=1}^{N} \big( O(\mathbf{R_i}) - \langle \hat{O} \rangle_E \big)^2. \tag{2.12}$$

According to the central limit theorem, the distribution of $\langle \hat{O} \rangle_E$ approaches a normal distribution as the number of sampling points N goes to infinity,

$$\langle \hat{O} \rangle_E \xrightarrow{\mathrm{d}} \mathcal{N}(\langle \hat{O} \rangle, \langle \sigma^2_{\hat{O}} \rangle), \tag{2.13}$$

where $\mathcal{N}(\mu, \sigma^2)$ stands for the normal distribution with mean $\mu$ and variance $\sigma^2$, therefore, as the sampling point number $N \to \infty$, the variance of the estimator $\langle \hat{O} \rangle_E$ goes to 0.

## 2.2 Variational Monte Carlo

Variational Monte Carlo is used to draw samples from the distribution, which reads

$$P(\mathbf{R}) = \frac{\big|\Psi_T(\mathbf{R})\big|^2}{\int d\mathbf{R} \big|\Psi_T(\mathbf{R})\big|^2}. \tag{2.14}$$

The trial wave function is usually the best estimate for the system under study that accommodates the correct symmetries. Choosing a proper trial wave function is vital to get reasonable energy estimates from the VMC method.

The energy and its variance for the given trial wave function $\Psi_T(\mathbf{R})$ is written as

$$E_T = \frac{\int d\mathbf{R}\big|\Psi_T(\mathbf{R})\big|^2 E_L(\mathbf{R})}{\int d\mathbf{R}\big|\Psi_T(\mathbf{R})\big|^2}, \tag{2.15}$$

and

$$\sigma_{E_T^2} = \frac{\int d\mathbf{R}\big|\Psi_T(\mathbf{R})\big|^2 (E_L(\mathbf{R}) - E_T)^2}{\int d\mathbf{R}\big|\Psi_T(\mathbf{R})\big|^2}, \tag{2.16}$$

in which $E_L(\mathbf{R})$ is the so-called local energy and is defined as

$$E_L(\mathbf{R}) = \frac{\hat{H}\Psi_T(\mathbf{R})}{\Psi_T(\mathbf{R})}. \tag{2.17}$$

Using the Metropolis algorithm discussed in previous section, after the evolution becomes stationary, one obtains a set of sampling points $\mathbf{R_i}$. The energy and its variance estimators can be written as

$$E_T = \frac{1}{N}\sum_{i=1}^{N} E_L(\mathbf{R}_i), \tag{2.18}$$

and

$$\sigma_{E_T^2} = \frac{1}{N}\sum_{i=1}^{N} (E_L(\mathbf{R}_i) - E_T)^2. \tag{2.19}$$

The energy from trial wave function provides an upper bound for the ground state energy, as indicated by the following vaiational condition

$$\frac{\big\langle \Psi_T(\mathbf{R})\big|\hat{H}\big|\Psi_T(\mathbf{R})\big\rangle}{\big\langle \Psi_T(\mathbf{R})\big|\Psi_T(\mathbf{R})\big\rangle} \geq \frac{\big\langle \Psi_0(\mathbf{R})\big|\hat{H}\big|\Psi_0(\mathbf{R})\big\rangle}{\big\langle \Psi_0(\mathbf{R})\big|\Psi_0(\mathbf{R})\big\rangle}, \tag{2.20}$$

where $\Psi_0(\mathbf{R})$ is the true ground state for the given Hamiltonian $\hat{H}$.

If $\Psi_T(\mathbf{R})$ is exactly the same as the true ground state, the local energy is constant and it is equal to ground state energy everywhere while the variance of the ground state energy is zero. This zero variance property greatly helps to find of finding the trial wave function that is close to the true ground state wave function. Hence, it is used in the trial wave function optiimization, as is described later in the optimization method section.

In practice, the average acceptance ratio in Metropolis algorithm is tuned to approximately 0.5 in order to makes the sampling of the phase space approximately optimal .

## 2.3 Diffusion Monte Carlo

Diffusion Monte Carlo (DMC) is a stochastic implementation of the Euclidean time projection

$$\lim_{\tau\to\infty} e^{-\tau\hat{H}}\big|\Psi_T(\mathbf{R})\big\rangle = e^{-\tau E_0}\big|\Psi_0(\mathbf{R})\big\rangle, \tag{2.21}$$

since the excited eigenstates states decay out exponentially faster than the ground state. In the simple form, the evolution of the ground state reads

$$\Psi(\mathbf{R}, t+\tau) = \int d\mathbf{R}' G(\mathbf{R}, \mathbf{R}'; \tau)\Psi(\mathbf{R}', t), \tag{2.22}$$

where $\mathbf{R}$ includes $d \times N$ coordinates of total number of N atoms, $G(\mathbf{R}, \mathbf{R}'; \tau)$ is the diffusion kernal which maybe written as

$$G(\mathbf{R}, \mathbf{R}'; \tau) \approx e^{-(V(\mathbf{R})-2E_T)\tau/2} G_0(\mathbf{R}, \mathbf{R}'; \tau) e^{-(V(\mathbf{R}')-2E_T)\tau/2} + O(\tau^3). \tag{2.23}$$

Eq. 2.23 can be derived by utilizing Trotter-Suzuki formula

$$e^{-\tau(\hat{A}+\hat{B})} = e^{-\frac{\tau}{2}\hat{B}} e^{-\tau\hat{A}} e^{-\frac{\tau}{2}\hat{B}} + O(\tau^3), \tag{2.24}$$

and by considering that

$$\hat{H} = \hat{T} + \hat{V}. \tag{2.25}$$

In Eq. 2.23

$$G_0(\mathbf{R}, \mathbf{R}'; \tau) = \Big\langle \mathbf{R}|e^{-\tau\hat{H}}|\mathbf{R}'\Big\rangle = \left[\frac{1}{2\pi\tau}\right]^{3/2N} e^{\frac{-(\mathbf{R}-\mathbf{R}')^2}{2\tau}}. \tag{2.26}$$

Here $E_T$ is a reference energy chosen to be close to the ground state energy $E_0$ in order to make the normalization(prefactor) of the calculated ground state asymptotically constant. It can be verified that Eq. 2.26 gives a $\delta$-function as the time step $\tau$ is decreased to 0. Also, this function satisfy

$$\frac{\partial G_0(\mathbf{R}, \mathbf{R}'; \tau)}{\partial\tau} = \frac{1}{2}\sum_{i=1}^{N} \nabla_i^2 G_0(\mathbf{R}, \mathbf{R}'; \tau), \tag{2.27}$$

as can be verified by direct calculation.

In simple diffusion Monte Carlo we choose a discrete set of $\delta$ functions to represent the original wave function, with each $\delta$ function in the phase space called a *walker*.

$$\Psi(\mathbf{R}; t) \to \sum_i \delta(\mathbf{R} - \mathbf{R_i}(t)), \tag{2.28}$$

After evolving by a time $\tau$, this becomes

$$\Psi(\mathbf{R}; t+\tau) \rightarrow \sum_i G(\mathbf{R}, \mathbf{R_i}; \tau), \tag{2.29}$$

The new wave function $\Psi(\mathbf{R})$ after time $\tau$ can then be sampled by using Eq. 2.37, which is a Gaussian distribution multiplied by an additional weight factor $P = e^{-(V(\mathbf{R})+V(\mathbf{R}_i)-2E_T)\tau/2}$. This weight factor can be treated by simply assigning additional weight to each sampling point or more efficiently by introducing the branching process. The implementation of the branching process maybe defined as 1) If $0 < P < 1$, keep the $\delta$ function which is originally in place $\mathbf{R}_i$ with a probability P, and 2) If $P \geq 1$, keep the $\delta$ function which is originally in place $\mathbf{R}_i$, and in addition, introduce new walker at the same position, with probability $P-1$. Intuitively, the phase space location with larger potential energy will favour the elimination of existing walkers while the location with lower potential energy will favor generation of new walkers. Also, $E_T$ that appears in the weight factor will be occasionally adjusted to keep the total number of walkers approximately constant. The adjusted $E_T$ is also a measurement of the ground state energy, and it is denoted as a growth estimator(See the estimator section).

### 2.3.1 Fixed-node approximation

The simple diffusion Monte Carlo is working for the ground state that is positive everywhere, for example, for the bosonic ground state. For fermionic systems, however, the simple diffusion Monte Carlo runs into a problem. Due to the Pauli principle, the fermionic ground state will be divided into positive region and negative region by the ground state wave function sign in that region. A naive solution of assigning positive and negative sign to each walker and let them diffuse in the configuration space will run into the famous fermionic sign problem, i.e., the positive and negative walkers will tend to cancel each other and left a diminishing signal to noise ratio, simply because both populations will converge to the (lowest) bosonic ground state, with the fermionic difference vanishing exponentially quickly.

An alternative treatment of the fermionic sign problem is to introduce fixed-node approximation. The idea is to introduce a trial wave function and require all the walkers to be constrained in the regions within which trial wave function remains positive or negative. Given the constraint of the nodal surface, which is of $3N-1$ dimensions in the $3N$ coordinate space, the ground state energy, denoted as $E_0^\alpha$, will be a strict upper bound for the true ground state $E_0$. To prove this property, we introduce a wave function defined in only one nodal pocket[25] $\Psi_0^{snp}(\mathbf{R})$, where the upper index stands for single nodal pocket, and $\Psi_0^{snp}(\mathbf{R}) = 0$ for the region outside the given nodal pocket. Within this nodal pocket, we require

$$\hat{H}\Psi_0^{snp}(\mathbf{R}) = E_0^\alpha \Psi_0^{snp}(\mathbf{R}), \tag{2.30}$$

The full trial wave function can be constructed from $\Psi_0^{snp}(\mathbf{R})$, as

$$\Psi(\mathbf{R}) = \frac{1}{N_P}\sum_P (-1)^P \Psi_0^{snp}(P\mathbf{R}) = \mathcal{A}\Psi_0^{snp}(\mathbf{R}), \tag{2.31}$$

where P is the permutation and $N_P$ is the number of permutations. The ground state energy statisfies

$$\begin{aligned} E_0 &\leq \frac{\int d\mathbf{R}\Psi^*(\mathbf{R})\hat{H}\Psi(\mathbf{R})}{\int \Psi^*(\mathbf{R})\Psi(\mathbf{R})} \\ &= \frac{\int d\mathbf{R}\Psi^*(\mathbf{R})\hat{H}\mathcal{A}\Psi_0^{snp}(\mathbf{R})}{\int d\mathbf{R}\Psi^*(\mathbf{R})\mathcal{A}\Psi_0^{snp}(\mathbf{R})} \\ &= \frac{\int d\mathbf{R}\Psi^*(\mathbf{R})\mathcal{A}\hat{H}\Psi_0^{snp}(\mathbf{R})}{\int d\mathbf{R}\Psi^*(\mathbf{R})\mathcal{A}\Psi_0^{snp}(\mathbf{R})} \\ &= E_0^{\alpha}. \end{aligned} \tag{2.32}$$

Here we use the properties that $\mathcal{A}$ commute with Hamiltonian, is self-adjoint and idempotent(i.e., $\mathcal{A}\Psi(\mathbf{R}) = \Psi(\mathbf{R})$ for a full antisymmetric wave function). From Eq. 2.32, the upper-bound property for the fixed-node approximation is clear. In real calculation for solid state or for electronic systems, the fixed-node bias is approximately 3 to 5 percent of the corrrelation energy for carefully chosen trial wave functions with the accurate nodal surfaces.

### 2.3.2 Fixed-node diffusion Monte Carlo with importance sampling

The simple algorithm provided in Eq. 2.22 can run into a problem of inefficiency for larger systems. The fixed-node diffusion Monte Carlo(FN-DMC) with importance sampling has been proposed[29, 70] to improve the efficiency. By multiplying by a trial wave function $\Psi_T(\mathbf{R})$ and evolving both sides of the Schrödinger Equation

$$f(\mathbf{R};\tau) = \Psi(\mathbf{R};\tau)\Psi_T(\mathbf{R}). \tag{2.33}$$

The Schrödinger equation for imaginary time can be written in terms of $f(\mathbf{R};\tau)$ as follows

$$-\frac{\partial f(\mathbf{R};\tau)}{\partial \tau} = -\frac{1}{2}\nabla^2 f(\mathbf{R};\tau) + \nabla\cdot(\mathbf{v_D}(\mathbf{R})f(\mathbf{R};\tau)) + (E_{\rm loc}(\mathbf{R}) - E_T)f(\mathbf{R};\tau), \tag{2.34}$$

where $E_{loc}$ is the local energy, $\mathbf{v_D}(\mathbf{R})$ is the drift velocity defined as

$$\mathbf{v_D}(\mathbf{R}) = \frac{\nabla\Psi_T(\mathbf{R})}{\Psi_T(\mathbf{R})}, \tag{2.35}$$

Eq. 2.34 can be recognized as the Fokker-Plank equation, and one can similarly write an integral equation as

$$f(\mathbf{R}; t+\tau) = \int d\mathbf{R}' G(\mathbf{R}, \mathbf{R}'; \tau) f(\mathbf{R}'; t), \tag{2.36}$$

and the Green's function $G(\mathbf{R}, \mathbf{R}', \tau)$ can be broken into a diffusion drift part and a weight part,

$$G(\mathbf{R}, \mathbf{R}'; \tau) \approx G_D(\mathbf{R}, \mathbf{R}'; \tau) G_w(\mathbf{R}, \mathbf{R}'; \tau), \tag{2.37}$$

where

$$G_D(\mathbf{R}, \mathbf{R}'; \tau) = \frac{1}{(2\pi\tau)^{3N/2}} \exp\left[-\frac{(\mathbf{R} - \mathbf{R}' - \tau \mathbf{v}_D(\mathbf{R}')^2}{2\tau}\right], \tag{2.38}$$

and

$$G_w(\mathbf{R}, \mathbf{R}'; \tau) = \exp[-\tau(E_{\text{loc}}(\mathbf{R}) + E_{\text{loc}}(\mathbf{R}') - 2E_T)]. \tag{2.39}$$

The new algorithm has several advantages over the simple diffusion Monte Carlo algorithm. First, the walkers are driven from phase space where $\Psi_T(\mathbf{R})$ is small to the phase space where $\Psi_T(\mathbf{R})$ is large. This is a direct consequence of the introduction of the drift term $\mathbf{v_D}(\mathbf{R})$. Also, near the nodal surface of the guiding wave function $\Psi_T(\mathbf{R})$, the drift term is close to infinity, so the requirement of walkers not passing the nodal surface is satisfied automatically. Finally, the local energy term $E_{\text{loc}}(\mathbf{R})$ in the exponential part is well controlled and has much smaller variance compared with $V(\mathbf{R})$, therefore, the weight fluctuation is much smaller.

The role of trial wave function $\Psi_T(\mathbf{R})$ in the fixed-node diffusion Monte Carlo with importance sampling is threefold:

- Provide the guiding wave function which is required by the importance sampling.
- Provide the nodal surface for the fixed-node approximation.
- Provide an initial configuration for diffusion Monte Carlo with preceding variational Monte Carlo run.

Due to the approximate nature of the Green's function in Eq. 2.37, the algorithm sometimes is problematic, especially in places where local energy is large. A simple remedy for this problem is to use a smaller time step, however, this can sometimes cause significant inefficiency, especially when the system under consideration is large. An alternative approach is to introduce acceptance/rejection steps in fixed-node Diffusion Monte Carlo[28].

Similarly to the Metropolis algorithm, a move from $\mathbf{R}'$ to $\mathbf{R}$ is accepted with the probability

$$\begin{aligned} p(\mathbf{R}, \mathbf{R}') &= \min\left[1, \frac{G_d(\mathbf{R}', \mathbf{R}; \tau) G_w(\mathbf{R}', \mathbf{R}; \tau) |\Psi_T(\mathbf{R}')|^2}{G_d(\mathbf{R}, \mathbf{R}'; \tau) G_w(\mathbf{R}, \mathbf{R}'; \tau) |\Psi_T(\mathbf{R})|^2}\right] \\ &= \min\left[1, \frac{G_d(\mathbf{R}', \mathbf{R}; \tau) |\Psi_T(\mathbf{R}')|^2}{G_d(\mathbf{R}, \mathbf{R}'; \tau) |\Psi_T(\mathbf{R})|^2}\right]. \end{aligned} \tag{2.40}$$

The rejection or acceptance proccss is justified by two facts. First, for the exact Green's function we have

$$G(\mathbf{R}, \mathbf{R}'; \tau)|\Psi_T(\mathbf{R}')|^2 = G(\mathbf{R}', \mathbf{R}; \tau)|\Psi_T(\mathbf{R})|^2, \tag{2.41}$$

which can be deduced from the definition of $G(\mathbf{R}, \mathbf{R}'; \tau)$ as

$$G(\mathbf{R}, \mathbf{R}'; \tau) = \Psi_T(\mathbf{R}) G_0(\mathbf{R}, \mathbf{R}'; \tau)/\Psi_T(\mathbf{R}'). \tag{2.42}$$

Also, the detailed balance condition Eq. 2.40 is always satisfied if the trial wave function $\Psi_T(\mathbf{R})$ is the same as the true ground state wave function $\Psi_0(\mathbf{R})$.

In practice, the average acceptance ratio is tuned to approximately 0.99, which facilitates the search for the ground state sample configuration in the phase space efficiently and accurately.

A full diffusion Monte Carlo method consists of the following steps:

- Prepare a set of walkers $\{\mathbf{R}_i\}$ distributed according to the variational wave function $|\Psi_T(\mathbf{R})|^2$(by VMC).
- Propose a move for each walker from original place $\mathbf{R}$ to $\mathbf{R} + \xi + \tau \mathbf{v_D}(\mathbf{R})$, where $\xi$ is drawn from gaussian distribution and $\mathbf{v_D}(\mathbf{R})$ is the drift velocity.
- Multiply the walker by an additional weight, given by Eq. 2.39.
- Check if the walker has passed the node provided by $\Psi_T(\mathbf{R})$, if yes, reject the move.
- Accept or reject the move with probability given by Eq. 2.40.
- If the weight of the walker is bigger than some threshold value, start to use branching process that make copy of the original walker. If the weight is smaller than ia random number $\eta$ generated from uniform distribution on interval $(0, 1)$, eliminate the walker.
- Adjust the reference energy $E_T$ to control the total weight of the walkers.
- After each walker is updated, collect statistics of observables for given blocks of steps of walkers.

In order to make use of the data generated by the algorithm, a detailed analysis of error is necessary, The fixed-node diffusion Monte Carlo has several well-known errors or problems:

1) Time step error[75]. If the time step is too large, the difference between approximate Green's function (Eq. 2.37) and the exact Green's function will be large. The rejection acceptance/procedure is introduced in Eq. 2.40 to alleviate the problem. Also, the observable quantities for each time step size could be measured and in the end, one can extrapolate to the zero time step.

2) Duplicated walkers and persistent configuration. In the region of low local energy, in some cases walkers are 'stuck' and keep branching, which causes problem because the walkers are supposed to move in the configuration space. This problem is monitored by watching the rejection rate(age) of the walker, and by decreasing the time step so that the rejection rates for the walkers are small.

3) Orthogonality problem. The orthogonality problem lies in the fact that the ground state component in the trial wave function is sometimes too small, as a result, the process of projecting out the true ground state takes too much time. The orthogonality problem is relatively rare and a careful selection of the trial wave function according to the physical picture can avoid this problem in most of cases.

4) Fixed-node error. The fixed-node approximation, aimed at solving the sign problem by constraining the walker path in the nodal pocket provided by guiding wave function $\Psi_T(\mathbf{R})$, will cause projected ground state energy to be higher than the true ground state energy, as proved in Eq. 2.32. The energy difference between the DMC energy and the true ground state energy is the fixed-node error. In order to estimate the fixed-node error, released-node diffusion Monte Carlo which changes the guiding wave function to let walkers pass through the nodal surface is used, a detailed introduction will be given in the next section.

With all these problems carefully monitored and corrected, the error bars from Monte Carlo runs are then only statistical error bars due to stochastic nature of the method.

### 2.3.3 Released-node diffusion Monte Carlo

The nodal surface of the trial wave function is generally not the same as that of the true ground state node. As a result, the fixed-node approximation leads to the fixed-node error because the accessible phase space for a given walker is limited within the nodal pocket in which it is located. One way how to correct the fixed-node error is to use the released-node method[27], which is the main subject of this section.

Released-node diffusion Monte Carlo(RN-DMC) is a transient estimate method. The basic idea of RN-DMC is to choose a guiding wave function $\Psi_G(\mathbf{R})$ that closely mimics the original trial wave function $\Psi_T(\mathbf{R})$ used in the fixed-node DMC but is non-zero in the region close to nodal surface of the original trial wave function. In this case the walkers near the nodal surface can pass through the node and this in essence corrects the nodes of the original trial wave function. A convenient choice of the new guiding wave function can be written as[24]

$$\Psi_G(\mathbf{R}) = \sqrt{|\Psi_T(\mathbf{R})|^2 + \alpha}, \tag{2.43}$$

where the free chosen parameter $\alpha$ is used to control the rate of the walkers passing through the nodal surface.

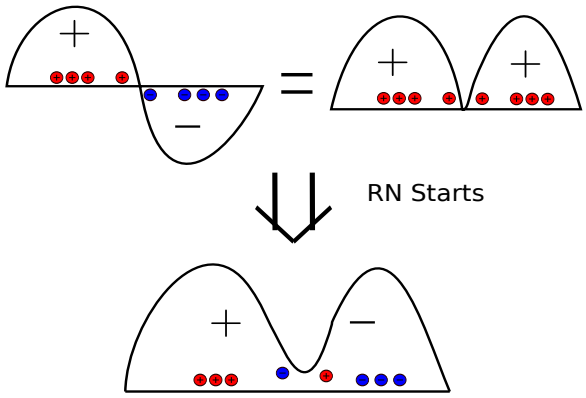


Figure 2.1: An illustration of released-node method. Originally all the walkers with positive sign and negative sign are restricted in their respective nodal pocket, and the energy is the same as bosonic system with the same node constrains, as shown on the upper panel of the graph. As the released-node process starts, the original nodal surface opens up gaps and walkers can now pass through different nodal pockets. During this process, which eventually projects to the bosonic ground state of the system, the fermionic signal can be picket up.

As illustrated in Figure 2.1, initially a fixed-node DMC run is conducted. At some time after equilibrating the DMC run, the guiding wave function of released-node method Eq. 2.43 is switched on, and walkers are able to pass cross the nodal surface under the new guiding wave function. This is mainly due to the fact that the drift $\mathbf{v_d}(\mathbf{R})$, defined in Eq. 2.35, is no longer approaching infinity near the nodal surface region. The drift term near the nodal surface is always pointing away from the nodal surface, as can be easily found from its definition, and the main mechanism of nodal passing behavior is due to diffusion, defined in Eq. 2.38.

The new guiding wave function will project out the *bosonic* ground state and during this process, the signal of the fermionic component may be projected out as

$$\begin{aligned} E_{\text{Fermi}} &= \frac{\int d\mathbf{R}\Psi_G(\mathbf{R})\Psi_{\text{DMC}}(\mathbf{R})\frac{\Psi_T(\mathbf{R}}{\Psi_G(\mathbf{R})}\frac{\hat{H}\Psi_T(\mathbf{R})}{\Psi_T(\mathbf{R})}}{\int d\mathbf{R}\Psi_G(\mathbf{R})\Psi_{\text{DMC}}(\mathbf{R})} \\ &= \frac{\sum_i w_i \frac{\Psi_T(\mathbf{R}_i)}{\Psi_G(\mathbf{R}_i)} E_{\text{loc}}(\mathbf{R}_i)}{\sum_i w_i \frac{\Psi_T(\mathbf{R}_i)}{\Psi_G(\mathbf{R}_i)}}, \end{aligned} \tag{2.44}$$

where the $w_i$ and $R_i$ are walker weight and walker position for $i$'s walker and $E_{\text{loc}}$ is the local energy.

The bosonic guiding wave function can also be used to get the bosonic energy, as

$$\begin{aligned} E_{\text{Boson}} &= \frac{\int d\mathbf{R}\Psi_G(\mathbf{R})\Psi_{\text{DMC}}(\mathbf{R})\frac{\hat{H}\Psi_G(\mathbf{R})}{\Psi_G(\mathbf{R})}}{\int d\mathbf{R}\Psi_G(\mathbf{R})\Psi_{\text{DMC}}(\mathbf{R})} \\ &= \frac{\sum_i w_i E_{\text{Gloc}}(\mathbf{R}_i)}{\sum_i w_i}, \end{aligned} \tag{2.45}$$

where $E_{\text{Gloc}}$ is the local energy for the bosonic guiding wave function, defined as

$$E_{\text{Gloc}} = \frac{\hat{H}\Psi_G(\mathbf{R})}{\Psi_G(\mathbf{R})}, \tag{2.46}$$

The Green's function which propagates $\Psi_G\Psi_{\text{DMC}}$ have the same form of that in Eq. 2.37, except in which the local energy $E_{\text{loc}}$ is replaced by $E_{\text{Gloc}}$, and drift velocity $v_D$ is now defined as

$$v_D(\mathbf{R}) = \frac{\nabla\Psi_G(\mathbf{R})}{\Psi_G(\mathbf{R})}. \tag{2.47}$$

Due to the transient nature of the released-node method, the error bars grow as

$$\sigma^2(t) \propto \frac{1}{N} e^{2\Delta_{BF}t}, \tag{2.48}$$

where $\Delta_{BF}$ is the energy difference between the ground state energy of bosonic and fermionic

states and $N$ is the number of walkers, so the variance is inverse proportional to $N$ and grows exponentially with the time.

To estimate the number and weight of walkers that have passed the nodal surface, an indicater quantity $\beta$ can be defined as

$$\beta = \frac{\sum_{i'} |w_{i'}|}{\sum_i |w_i|} \tag{2.49}$$

where the index $i'$ runs over the walkers that have passed the nodal surface odd number of times, and index $i$ runs over all walkers.

In practice, the $\beta = 1$ right after the RN-DMC procedure, when no walkers have passed the nodal surface. We also found that when $\beta$ is less than 0.8 the released-node signal has already been lost for most of the cases that's been studied in the unpolarized Fermi gas system.

In order to monitor the statistical signal, a record of the walkers that have never passed the nodal surface can also be kept, these walkers are in this sense still a fixed-node ensemble, with guiding wave function different from the trial wave function. In essence discarding the walkers that have passed through the nodal surface is an approximation which regards the walkers that have passed as a second order effect. The FN-DMC signal during the RN-DMC runs can be used as a measurement of the validity of the parameter $\alpha$ in Eq. 2.43 so that the parameter is within a reasonable range. This helps to obtain the maximum nodal release information while keeping the influence of the guiding wave function $\Psi_G(\mathbf{R})$ relatively small when compared to the original trial wave function $\Psi_T(\mathbf{R})$.

There are several variations to the simple version RN-DMC procedure, which involve

- Changing the guiding wave function form.
- Adding the branching procedure.
- Cancelling walkers with positive and negative weight when they are close (annihilation procedure).

And in these variations, the cancelling walker procedure most likely increase the sampling efficiency and signal to noise ratio after the released-node procedure starts.

## 2.4 Reptation Monte Carlo

The diffusion Monte Carlo method is a powerful method and works well to measure the observable quantities when the trial wave function and ground state is close enough. As will be elaborated in the next section, when the observables do not commute with the Hamiltonian,

the so called mixed-estimator will generate error terms that sometimes can not be neglected. The reptation Monte Carlo is then introduced to fix the problem.

Reptation Monte Carlo(RMC) uses similar idea with DMC to project out the ground state from a trial wave function $\Psi_T(\mathbf{R})$, but there are also important differences between these two methods:

- RMC directly samples the configurations and weights. The weight is already contained in the sampling process through the acceptance/rejection step and the branching process is absent. The sampling points don't carry any weight with them.
- RMC samples in both directions by introducing the sampling object path $[\mathbf{R^0}, \mathbf{R^1}, \cdots, \mathbf{R^L}]$. All the estimators in the RMC method are pure estimators, assuming the samples from the mid-point of the path are used.

The core algorithm of RMC is straightforward We want to evaluate the partition function for a given trial wave function, using the path integral formulation to split projection time into M slices, $\tau = M\epsilon$

$$Z_0 = \left\langle \Psi_T | e^{-\tau \hat{H}} | \Psi_T \right\rangle = \int e^{-S[\mathbf{R}]} P[\mathbf{R}] D[\mathbf{R}], \tag{2.50}$$

Where

$$D[\mathbf{R}] = d\mathbf{R^0} d\mathbf{R^1} \cdots d\mathbf{R^M}, \tag{2.51}$$

in which $\mathbf{R}$ is the $3N$ configuration space and the upper index is for the projection time slice. The weight factor $S[\mathbf{R}]$ is

$$S[\mathbf{R}] = (1/2)E_{\text{loc}}(\mathbf{R^0}) + E_{\text{loc}}(\mathbf{R^1}) + \cdots + E_{\text{loc}}(\mathbf{R^{M-1}}) + (1/2)E_{\text{loc}}(\mathbf{R^M}) \tag{2.52}$$

where the first and last term of the local energy have factor of 1/2. The probability distribution $P[\mathbf{R}]$ is denoted as

$$P[\mathbf{R}] = G(\mathbf{R^M}, \mathbf{R^{M-1}}; \tau) G(\mathbf{R^{M-1}}, \mathbf{R^{M-2}}; \tau) \cdots G(\mathbf{R^1}, \mathbf{R^0}; \tau) \Psi_T^2(\mathbf{R^0}) \tag{2.53}$$

where $G(\mathbf{R}, \mathbf{R}'; \tau)$ is the Greens function defined in Eq. 2.38.

To measure the ground state energy after equilibrium has been reached, use the relation

$$E_0 = -\lim_{\tau \to \infty} \frac{d}{d\tau} \log Z_0 = \lim_{\tau \to \infty} \frac{\left\langle E_{\text{loc}} e^{-S[\mathbf{R}]} \right\rangle}{\left\langle e^{-S[\mathbf{R}]} \right\rangle}, \tag{2.54}$$

In order to alleviate the problem of weight fluctuation, an additional acceptance rejection

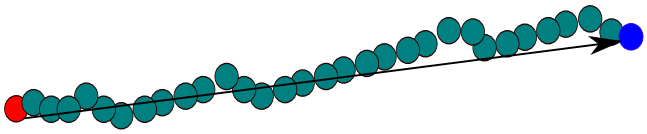

Figure 2.2: A graphic illustration of the RMC method. The dots represent sampling points in the RMC method. In the sampling process, randomly pick one direction(as illustrated on the graph), propose the move and if accepted, delete the sampling on the other end, and add the new sampling point in the selected direction in front of the old point.

step is introduced to directly sample $e^{-S[\mathbf{R}]}P[\mathbf{R}]$ as

$$A[\mathbf{R^i}, \mathbf{R^j}] = \min\left[1, \frac{W^0[\mathbf{R^j}, \mathbf{R^i}]P[\mathbf{R^j}]}{W^0[\mathbf{R^i}, \mathbf{R^j}]P[\mathbf{R^i}]}\right], \tag{2.55}$$

Where the basic sampling points in the configuration space is denoted as $[\mathbf{R^0}, \mathbf{R^1}, \cdots, \mathbf{R^L}]$, with each $R$ being a point in 3N dimensional space. This is the so-called reptile.

In this cases, the average over the weight factor $e^{-S[\mathbf{R}]}$ has already been taken into account and the ground state energy can be written as

$$E_0 = \lim_{\tau\to\infty} 1/2\left\langle E_{\rm loc}(\mathbf{R}^0) + E_{\rm loc}(\mathbf{R}^M)\right\rangle \tag{2.56}$$

and other observable quantity $\hat{O}$ (suppose $\hat{O}$ is a one-body operator) as

$$< \hat{O} >= \lim_{\tau\to\infty}\left\langle \int_\sigma^{\tau-\sigma} d\tau' \frac{\hat{O}(\tau')}{\tau - 2\sigma}\right\rangle, \tag{2.57}$$

where $O(\tau')$ is the quantity that may or may not commute with Hamiltonian.

The algorithm of RMC is illustrated in Figure 2.4

To summarize, the basic reptation Monte Carlo is implemented in the following steps,

- Select a direction of time for the reptile $[\mathbf{R^0}, \mathbf{R^1}, \cdots, \mathbf{R^L}]$, if the direction is backward,

reverse the reptile to be $[\mathbf{R^L}, \mathbf{R^{L-1}}, \cdots, \mathbf{R^0}]$.

- Generate a new sequent of the reptile $[\mathbf{R^K}, \mathbf{R^{K+1}}, \cdots, \mathbf{R^{K+L}}]$ according to the Green's function Eq. 2.38, with the time step chosen to minimize the correlation time.
- Accept or reject the new reptile according to the acceptance rate Eq. 2.55.
- Measure the observable quantities after the algorithm converges.

## 2.5 Wave functions, observables and estimators

Constructing many-body wave functions is a direct way of study many-body effects, in parallel to the reduction methods that are otherwise used to reduce the complexity of many-body problems to one-body problems, such as density functional theory or Green's function calculation.

In the DMC simulation, the quality of the trial wave function directly affects the nodal surface and the projected ground state energy, and a well-chosen wave function is sometimes the key of getting the ground state energy right. In this section, we introduce the wave function and its construction method that is generally used in quantum Monte Carlo calculation. Besides the wave function, we also introduce calculations of the observable quantities which can be deduced from the wave function.

### 2.5.1 Trial wave functions

A careful selection of the trial wave function is important in order to mimic the system ground state wave functioni as closely as possible. This facilitates fast projection of the ground state. The wave function selection should take into account several considerations: Pauli principle for fermions should be obeyed, which requires that

$$\Psi_T(\cdots \mathbf{r_i} \cdots \mathbf{r_j} \cdots) = -\Psi_T(\cdots \mathbf{r_j} \cdots \mathbf{r_i} \cdots), \tag{2.58}$$

where $\mathbf{r_i}$ and $\mathbf{r_j}$ are the coordinates for the same spicies of fermions. The wave function generally should conserve the symmetry of the system, for example, if the ground state is known to be rotationally invariant, the ground state wave function should obey the symmetry. For bound states, the wave function should be square integrable over the space so that it has finite norm.

In practice, several forms of the wave has been used, including Slater wave function, BCS wave function and Pfaffian wave function, which are chosen to obey the general considerations mentioned above.

The Slater wave function reads

$$\Psi_{\rm HF}(\mathbf{r_1},\cdots,\mathbf{r_N};\mathbf{r'_1},\cdots,\mathbf{r'_N}) = \det\begin{bmatrix} \phi_1(\mathbf{r_1}) & \dots & \phi_N(\mathbf{r_1}) \\ \vdots & \ddots & \vdots \\ \phi_1(\mathbf{r_N}) & \dots & \phi_N(\mathbf{r_N}) \end{bmatrix} \det\begin{bmatrix} \phi_1(\mathbf{r'_1}) & \dots & \phi_N(\mathbf{r'_1}) \\ \vdots & \ddots & \vdots \\ \phi_1(\mathbf{r'_N}) & \dots & \phi_N(\mathbf{r'_N}) \end{bmatrix}, \tag{2.59}$$

Where the $N$ and $N'$ are the numbers for spin-up and spin-down atoms, and $\phi_i(\mathbf{r})$ are single particle orbitals which may or may not be the same for different spins of atoms. For example, for electrons with Coulombic interactions, the true Hatree-Fock ground state is found to have broken the spin-up and spin-down symmetry[80], in general. The Slater wave function is the simplest wave function which obeys the antisymmetric criteria Eq. 2.58 with *assigned spins*,

Assuming the orbitals are Hartree-Fork orbitals the expectation of the energy is the Hartree-Fock energy,

$$E_{\rm HF} = \int d\mathbf{r_1}\cdots\mathbf{r_N}d\mathbf{r'_1}\cdots\mathbf{r'_N}\Psi^*_{HF}(\mathbf{r_1},\cdots,\mathbf{r_N};\mathbf{r'_1},\cdots,\mathbf{r'_N})\hat{H}\Psi_{HF}(\mathbf{r_1},\cdots,\mathbf{r_N};\mathbf{r'_1},\cdots,\mathbf{r'_N}), \tag{2.60}$$

The missing part of the total energy is often called the correlation energy so that

$$E_{\rm exact} = E_{\rm HF} + E_{\rm corr}. \tag{2.61}$$

The extension of the single Slater determinant is expansion of the ground state into linear combination of determinant(configuration interaction),

$$\Psi_{\rm CI} = \sum_i^{\rm exc} c_i \Psi^{(i)}_{\rm HF}, \tag{2.62}$$

where $i$ represents an excitation which can be constructed, for example, by replacing an occupied orbital by virtual orbital. The summation of $i$ is to include low energy excited orbital to replace up to some cut-off. Coefficients $c_i$ are found variationally. For example, the inclusion of one additional virtual orbital $\phi_{N+1}$ replacing an occupied orbital can be written as:

$$\Psi^{(i)}_{\rm HF} = \det\begin{bmatrix} \phi_1(\mathbf{r_1}) & \dots & \phi_{N-1}(\mathbf{r_1}) & \phi_{N+1}(\mathbf{r_1}) \\ \vdots & \ddots & \vdots & \vdots \\ \phi_1(\mathbf{r_N}) & \dots & \phi_{N-1}(\mathbf{r_N}) & \phi_{N+1}(\mathbf{r_N}) \end{bmatrix} \det\begin{bmatrix} \phi_1(\mathbf{r'_1}) & \dots & \phi_N(\mathbf{r'_1}) \\ \vdots & \ddots & \vdots \\ \phi_1(\mathbf{r'_N}) & \dots & \phi_N(\mathbf{r'_N}) \end{bmatrix} \tag{2.63}$$

The full configuration state function usually requires large number of determinants due to

the existence of large number of virtual obitals and possible number of excitations. Therefore a truncation is required to limit the expansion to several lowest excitations.

Meanwhile, the product of spin-up and spin-down determinants can be combined into one single Slater wave function, as

$$\begin{aligned}\Psi_{HF}(\mathbf{r_1},\cdots,\mathbf{r_N};\mathbf{r'_1},\cdots,\mathbf{r'_N}) &= \det\begin{bmatrix} \sum_{i=1}^{N}\phi_i(\mathbf{r_1})\phi_i(\mathbf{r'_1}) & \cdots & \sum_{i=1}^{N}\phi_i(\mathbf{r_N})\phi_i(\mathbf{r'_1}) \\ \vdots & \ddots & \vdots \\ \sum_{i=1}^{N}\phi_i(\mathbf{r_N})\phi_i(\mathbf{r'_1}) & \cdots & \sum_{i=1}^{N}\phi_i(\mathbf{r_N})\phi_i(\mathbf{r'_N}) \end{bmatrix} \\ &= \det\begin{bmatrix} \Phi(\mathbf{r_1},\mathbf{r'_1}) & \cdots & \Phi(\mathbf{r_1},\mathbf{r'_N}) \\ \vdots & \ddots & \vdots \\ \Phi(\mathbf{r_N},\mathbf{r'_1}) & \cdots & \Phi(\mathbf{r_N},\mathbf{r'_N}) \end{bmatrix}.\end{aligned} \tag{2.64}$$

where $\Phi(\mathbf{r_i},\mathbf{r'_i})$ is the two-body orbital. Eq. 2.64 can be straightforwardly proved from Eq. 2.59.

Projected BCS wave function has form similar to Eq. 2.64, with the pairing orbital $\Phi(\mathbf{r_1},\mathbf{r_2})$ to be restricted in the form $\Phi(\mathbf{r_1}-\mathbf{r_2})$, i.e., the center of mass motion of the paired atoms should be 0.

$$\Psi_{\mathrm{BCS}} = \mathcal{A}\left[\Phi(\mathbf{r_1},\mathbf{r'_1})\Phi(\mathbf{r_2},\mathbf{r'_2})\cdots\Phi(\mathbf{r_N},\mathbf{r'_N})\right] = \det\begin{bmatrix} \Phi(\mathbf{r_1}-\mathbf{r'_1}) & \cdots & \Phi(\mathbf{r_1}-\mathbf{r'_N}) \\ \vdots & \ddots & \vdots \\ \phi_1(\mathbf{r_N}-\mathbf{r'_1}) & \cdots & \Phi(\mathbf{r_N}-\mathbf{r'_N}) \end{bmatrix}. \tag{2.65}$$

Further difference is that in BCS case the singlet pair orbital includes also virtual states

$$\Phi(\mathbf{r_i},\mathbf{r_j}) = \sum_{\alpha,\beta=\mathrm{occ,virt}} c_{\alpha\beta}\phi_\alpha(\mathbf{r}_i)\phi_\beta(\mathbf{r}_j), \tag{2.66}$$

where $c_{\alpha\beta} = c_{\beta\alpha}$ and these coefficients are optimized variationally.

In order to calculate the pairing gap for the system, the BCS wave function is extended to include one additional atoms,

$$\begin{aligned}\Psi_{\mathrm{BCS}} = \mathcal{A}\left[\Phi(\mathbf{r_1},\mathbf{r'_1})\Phi(\mathbf{r_2},\mathbf{r'_2})\cdots\Phi(\mathbf{r_N},\mathbf{r'_N})\phi(\mathbf{r_{N+1}})\right] = \\ \det\begin{bmatrix} \Phi(\mathbf{r_1}-\mathbf{r'_1}) & \cdots & \Phi(\mathbf{r_1}-\mathbf{r'_N}) & \phi(\mathbf{r_1}) \\ \vdots & \ddots & \vdots & \vdots \\ \Phi(\mathbf{r_N}-\mathbf{r'_1}) & \cdots & \Phi(\mathbf{r_N}-\mathbf{r'_N}) & \phi(\mathbf{r_{N+1}}) \\ \phi(\mathbf{r'_1}) & \cdots & \phi(\mathbf{r'_N}) & 0 \end{bmatrix}.\end{aligned} \tag{2.67}$$

where $\phi(\mathbf{r})$ may be optimized so that the BCS wave function yield lowest variational energy.

The energy gap is then calculated by the energies difference,

$$\Delta = E_{2N+1} - \frac{1}{2}(E_{2N} + E_{2N+2}). \tag{2.68}$$

Pfaffian wave function[6] is a further generalization of BCS wave function, which can be used as a compact form that builds both triplet pairing and singlet pairing simultaneously. The Pfaffian wave function has the requirement of dimension to be even and elements to be skew-symmetric, i.e., the (i,j) element is of same absolute value and opposite sign with (j,i) element.

$$\mathrm{pf[A]} = \mathrm{pf}\begin{bmatrix} 0 & a_{12} & a_{13} & \dots & a_{1,2N} \\ -a_{12} & 0 & a_{23} & \dots & a_{2,2N} \\ -a_{13} & -a_{23} & 0 & \ddots & \vdots \\ \vdots & \ddots & \ddots & \ddots & \vdots \\ -a_{1,2N} & \dots & \dots & \dots & 0 \end{bmatrix} = \sum_{\mathrm{P}} (-1)^{\mathrm{P}} \mathrm{a_{P(1,2)} a_{P(3,4)} \cdots a_{P(2N-1,2N)}} \tag{2.69}$$

where P is the permutation that applies on the pair which includes $(2N-1)!!$ terms. A simple example of pfaffian is given by the smallest non-trivial pfaffian matrix with the size 4 by 4,

$$\mathrm{pf}\begin{bmatrix} 0 & a_{12} & a_{13} & a_{14} \\ -a_{12} & 0 & a_{23} & a_{24} \\ -a_{13} & -a_{23} & 0 & a_{34} \\ -a_{14} & -a_{24} & -a_{34} & 0 \end{bmatrix} = a_{12}a_{34} - a_{13}a_{24} + a_{14}a_{23} \tag{2.70}$$

Or it can be denoted using recursive notation as

$$\mathrm{pf}[A] = \sum_{j=2}^{2N} (-1)^j a_{1,j} \sum_{P} (-1)^P \prod_{\substack{k<l, \\ k,l\neq 1,j}} a_{P(k,l)} \tag{2.71}$$

This is similar to the usual recursive relation of determinant, with only modification of eliminating two elements instead of one in the determination of next recursive terms.

The pfaffian matrix can be used as a compact wave function building triplet and singlet pairing simultaneously,

$$\mathrm{pf[A]} = \mathrm{pf}\begin{bmatrix} \Xi^{\uparrow\uparrow} & \Phi^{\uparrow\downarrow} & \phi^{\uparrow} \\ -\Phi^{\uparrow\downarrow T} & \Xi^{\downarrow\downarrow} & \phi^{\downarrow} \\ -\phi^{\uparrow} & -\phi^{\downarrow} & 0 \end{bmatrix}, \tag{2.72}$$

where $\Xi^{\uparrow\uparrow}$ and $\Xi^{\downarrow\downarrow}$ are blocks of the triplet pairing orbitals with parallel spins, $\Phi^{\uparrow\downarrow}$ is block of the singlet pairing orbitals plus. $\phi^{\uparrow}$ and $\phi^{\downarrow}$ are the blocks of unpaired orbitals for spin up and

spin down channels.

The pfaffian wave function satisfy some general properties, the detailed proof can be found in [7]. Suppose matrix $A$ is skew symmetric of size 2n by 2n, $B$ and $M$ are arbitrary matrices of size 2n by 2n and n by n, respectively,

$$\mathrm{pf}[A^T] = (-1)^n \mathrm{pf}[A], \tag{2.73}$$

$$\mathrm{pf}^2[A] = \det[A], \tag{2.74}$$

$$\mathrm{pf}\begin{bmatrix} A_1 & 0 \\ 0 & A_2 \end{bmatrix} = \mathrm{pf}[A_1]\mathrm{pf}[A_2], \tag{2.75}$$

$$\mathrm{pf}[BAB^T] = \det[B]\mathrm{pf}[A], \tag{2.76}$$

$$\mathrm{pf}\begin{bmatrix} 0 & M \\ -M^T & 0 \end{bmatrix} = (-1)^{n(n-1)/2}\det[M]. \tag{2.77}$$

From the last identity in Eq. 2.73 it is clear that the pfaffian wave function is an extension of the BCS wave function, with extra degrees of freedom built in triplet pairing.

To better accommodate the correlation effect between different atoms, usually a correlation Jastrow factor multiplies the wave function:

$$\Psi_{\mathrm{Jast}}(\mathbf{R}) = \exp\left[\sum_k u_1(\mathbf{r_k}) + \sum_{l,m} u_2(\mathbf{r_l}, \mathbf{r_m}) + \sum_{n,p,q} u_3(\mathbf{r_n}, \mathbf{r_p}, \mathbf{r_q})\right], \tag{2.78}$$

where $u_1(\mathbf{r_k}), u_2(\mathbf{r_l}, \mathbf{r_m})$ and $u_3(\mathbf{r_n}, \mathbf{r_p}, \mathbf{r_q})$ correspond to one-body, two-body correlations and possibly, three-body correlation terms.

Given the Jastrow factor, full wave function may be written as

$$\Psi(\mathbf{R}) = \Psi_{\mathrm{id}}(\mathbf{R})\Psi_{\mathrm{Jast}}(\mathbf{R}) \tag{2.79}$$

Where $\Psi_{\mathrm{id}}$ can be chosen such that its nodal surface is correctly mimicking the nodal surface of the true ground state.

In order to capture the local distortion of nodal surface and better describe the many body effect, the so-called backflow wave function is used by transforming the original coordinates of a given atom $i$ to a new position,

$$\mathbf{x_i} = \mathbf{r_i} + \sum_{j \neq i} (\mathbf{r_i} - \mathbf{r_j})\gamma(r_{ij}), \tag{2.80}$$

where $r_{ij} = |\mathbf{r}_i - \mathbf{r}_j|$, $\gamma(r_{ij})$ is a function which tunes the imapact of neighbors on the given particle position. $\gamma(r_{ij})$ can further expand in some complete or overcomplete basis sets and

optimized to minimize variance or energy expectation.

The new wave function is then written as

$$\Psi(\mathbf{R}) = \Psi(\mathbf{x_1}, \cdots, \mathbf{x_N}; \mathbf{x'_1}, \cdots, \mathbf{x'_N}), \tag{2.81}$$

with transformed coordinates defined in Eq. 2.80

It should be noted that backflow wave function can improve the nodal surface only locally, while the global nodal surface distortion effect may still be hard to correct, this puts limitation on its usefulness.

The wave function introduced in this section, the Slater, BCS, and Pfaffian with the Jastrow factor correspond to the wave function that are used in this thesis and used frequently in the past for solid state and electron gas calculations. However, these wave functions do not exhaust the realm of possibilities. In future, new wave function forms will shed more light on new physics which is beyond the current knowledge.

### 2.5.2 Mixed, Pure and Growth Estimators

In VMC, a one-body operator expectation is determined as follows,

$$\left\langle \hat{O} \right\rangle_V = \frac{\left\langle \Psi_T(\mathbf{R}) | \hat{O} | \Psi_T(\mathbf{R}) \right\rangle}{\left\langle \Psi_T(\mathbf{R}) | \Psi_T(\mathbf{R}) \right\rangle}, \tag{2.82}$$

In FN-DMC or RMC, which generate the projection to the ground state $\Psi_0$, two expressions for $\left\langle \hat{O} \right\rangle$ can be defined, given mixed and pure estimators: Two estimators are then used as mixed and pure estimators:

$$\left\langle \hat{O} \right\rangle_{\text{mix}} = \frac{\left\langle \Psi_0(\mathbf{R}) | \hat{O} | \Psi_T(\mathbf{R}) \right\rangle}{\left\langle \Psi_0(\mathbf{R}) | \Psi_T(\mathbf{R}) \right\rangle}, \tag{2.83}$$

and

$$\left\langle \hat{O} \right\rangle_{\text{pure}} = \frac{\left\langle \Psi_0(\mathbf{R}) | \hat{O} | \Psi_0(\mathbf{R}) \right\rangle}{\left\langle \Psi_0(\mathbf{R}) | \Psi_0(\mathbf{R}) \right\rangle}. \tag{2.84}$$

If the operator $\hat{O}$ commutes with the Hamiltonian of the system, the relation of pure and mixed estimator is simply

$$\frac{\left\langle \Psi_0(\mathbf{R}) | \hat{O} | \Psi_T(\mathbf{R}) \right\rangle}{\left\langle \Psi_0(\mathbf{R}) | \Psi_T(\mathbf{R}) \right\rangle} = \bar{O} \frac{\left\langle \Psi_0(\mathbf{R}) | \Psi_T(\mathbf{R}) \right\rangle}{\left\langle \Psi_0(\mathbf{R}) | \Psi_T(\mathbf{R}) \right\rangle} = \bar{O}, \tag{2.85}$$

where $\bar{O}$ is the corresponding eigen value.

If the operator $\hat{O}$ does not commute with the Hamiltonian, we assume that the trial wave

function $\Psi_T(\mathbf{R})$ is sufficiently close to the $\Psi_0(\mathbf{R})$, and then we can write

$$\Psi_0 = \Psi_T + \delta\Psi, \tag{2.86}$$

and thus by neglecting second order terms in $\delta\Psi$

$$\begin{aligned}
\left\langle \hat{O} \right\rangle_{\text{pure}} &= \frac{\left\langle \Psi_T(\mathbf{R}) + \delta\Psi(\mathbf{R}) | \hat{O} | \Psi_T(\mathbf{R}) + \delta\Psi(\mathbf{R}) \right\rangle}{\left\langle \Psi_T(\mathbf{R}) + \delta\Psi(\mathbf{R} | \Psi_T(\mathbf{R}) + \delta\Psi(\mathbf{R}) \right\rangle} \\
&= \frac{\left\langle \Psi_T(\mathbf{R}) | \hat{O} | \Psi_T(\mathbf{R}) \right\rangle + 2\left\langle \delta\Psi(\mathbf{R}) | \hat{O} | \Psi_T(\mathbf{R}) \right\rangle}{\left\langle \Psi_T(\mathbf{R}) | \Psi_T(\mathbf{R}) \right\rangle + 2\left\langle \delta\Psi(\mathbf{R}) | \Psi_T(\mathbf{R}) \right\rangle} \\
&\approx \frac{2\left\langle \Psi_0(\mathbf{R}) | \hat{O} | \Psi_T(\mathbf{R}) \right\rangle - \left\langle \Psi_T(\mathbf{R}) | \hat{O} | \Psi_T(\mathbf{R}) \right\rangle}{\left\langle \Psi_T(\mathbf{R}) | \Psi_T(\mathbf{R}) \right\rangle + 2\left\langle \delta\Psi(\mathbf{R}) | \Psi_T(\mathbf{R}) \right\rangle} \\
&\approx 2\left\langle \hat{O} \right\rangle_{\text{mix}} - \left\langle \hat{O} \right\rangle_T + \mathcal{O}(\delta\Psi^2),
\end{aligned} \tag{2.87}$$

and also

$$\begin{aligned}
\left\langle \hat{O} \right\rangle_{\text{pure}} &= \frac{\left\langle \Psi_T(\mathbf{R}) + \delta\Psi(\mathbf{R}) | \hat{O} | \Psi_0(\mathbf{R}) \right\rangle}{\left\langle \Psi_T(\mathbf{R}) + \delta\Psi(\mathbf{R}) | \Psi_0(\mathbf{R}) \right\rangle} \\
&= \frac{\left\langle \Psi_T(\mathbf{R}) + \delta\Psi(\mathbf{R}) | \hat{O} | \Psi_0(\mathbf{R}) \right\rangle \frac{\left\langle \Psi_T(\mathbf{R}) | \hat{O} | \Psi_T(\mathbf{R}) \right\rangle}{\left\langle \Psi_T(\mathbf{R}) | \Psi_T(\mathbf{R}) \right\rangle}}{\left\langle \Psi_T(\mathbf{R}) + \delta\Psi(\mathbf{R}) | \Psi_0(\mathbf{R}) \right\rangle \frac{\left\langle \Psi_T(\mathbf{R}) | \hat{O} | \Psi_T(\mathbf{R}) \right\rangle}{\left\langle \Psi_T(\mathbf{R}) | \Psi_T(\mathbf{R}) \right\rangle}} \\
&= \frac{\left\langle \Psi_T(\mathbf{R}) + \delta\Psi(\mathbf{R}) | \hat{O} | \Psi_0(\mathbf{R}) \right\rangle \frac{\left\langle \Psi_0(\mathbf{R}) - \delta\Psi(\mathbf{R}) | \hat{O} | \Psi_0(\mathbf{R}) \right\rangle}{\left\langle \Psi_T(\mathbf{R}) - \delta\Psi(\mathbf{R} | \Psi_T(\mathbf{R}) \right\rangle}}{\left\langle \Psi_T(\mathbf{R}) + \delta\Psi(\mathbf{R}) | \Psi_0(\mathbf{R}) \right\rangle \frac{\left\langle \Psi_T(\mathbf{R}) | \hat{O} | \Psi_T(\mathbf{R}) \right\rangle}{\left\langle \Psi_T(\mathbf{R}) | \Psi_T(\mathbf{R}) \right\rangle}} \\
&\approx \frac{\left\langle \hat{O} \right\rangle_{\text{mix}}^2}{\left\langle \hat{O} \right\rangle_T} + \mathcal{O}(\delta\Psi),
\end{aligned} \tag{2.88}$$

which is, however, coverd only to the first order in $\delta\Psi$.

In most of DMC calculation, the pure estimator value is deduced from Eq. 2.87. In RMC, since the projection is on both sides, the pure estimator can be directly collected from the sampling points in the center of the reptile.

There is still another type of estimator used specifically for the ground state energy, the so called growth estimator[75],

$$E_0 = -\frac{1}{\tau} \log \frac{\left\langle \Psi_T(\mathbf{R}) | e^{-\tau \hat{H}} | \Psi_0(\mathbf{R}) \right\rangle}{\left\langle \Psi_T(\mathbf{R}) | \Psi_0(\mathbf{R}) \right\rangle}, \tag{2.89}$$

where $\tau$ is the time step for the Monte Carlo, and $e^{-\tau \hat{H}}$ is just the Euclidean projection operator for the system. However, it typically has somewhat larger fluctuations than the estimations based on spatial average. In practice, mixed estimator from Eq. 2.83 is most frequently used in DMC, and both mixed estimator and pure estimator is used in RMC.

### 2.5.3 Pair correlation function

Pair correlation function is used to characterize the probability of finding one atom, say, at $\mathbf{r}_2$ given the fact that another atom is at $\mathbf{r}_1$. It is convenient because its relation to various quantities such as potential energy and static structure factor, and also it can be directly measured from the experiment. The pair correlation function $g(\mathbf{r_1}, \mathbf{r_2})$ is defined as

$$n_{\sigma_1}(\mathbf{r_1}) n_{\sigma_2}(\mathbf{r_2}) g(\mathbf{r_1}, \mathbf{r_2}) = \left\langle \Phi^\dagger_{\sigma 1}(\mathbf{r_1}) \Phi^\dagger_{\sigma 2}(\mathbf{r_2}) \Phi_{\sigma 2}(\mathbf{r_2}) \Phi_{\sigma 1}(\mathbf{r_1}) \right\rangle, \tag{2.90}$$

where $n_{\sigma_1}(\mathbf{r_1})$ and $n_{\sigma_2}(\mathbf{r_2})$ denote the density of atoms in position $\mathbf{r}_1$ and $\mathbf{r}_2$ with spin $\sigma_1$ and $\sigma_2$. In this definition, the pair correlation function is equal to 1 if there is no correlation between different atoms within a given distance.

The pair correlation function can also be used to calculate the potential energy, as

$$\hat{V} = \frac{1}{2} \int d\mathbf{r_1} d\mathbf{r_2} \Phi^\dagger(\mathbf{r_1}) \Phi^\dagger(\mathbf{r_2}) V(\mathbf{r_1} - \mathbf{r_2}) \Phi(\mathbf{r_2}) \Phi(\mathbf{r_1}), \tag{2.91}$$

where $\Phi(\mathbf{r})^\dagger$, $\Phi(\mathbf{r})$ is creation and annihilation operator in the second quantization form, and therefore

$$\left\langle \hat{V} \right\rangle = \frac{1}{2} \int d\mathbf{r_1} d\mathbf{r_2} g(\mathbf{r_1}, \mathbf{r_2}) V(\mathbf{r_1} - \mathbf{r_2}) \tag{2.92}$$

If the system is homogeneous, the pair correlation function can be written as

$$g(\mathbf{r_1}, \mathbf{r_2}) = g(|\mathbf{r_1} - \mathbf{r_2}|) = g(r), \tag{2.93}$$

where $r$ is the relative distance between atoms 1 and 2.

The pair correlation can also be linked with the static structure factor[48],

$$S_{\uparrow\downarrow}(k) = \frac{2}{3\pi} \int_0^\infty dr r^2 k_F^3 [g_{\uparrow\downarrow}(k_F r) - 1] r^2 \frac{\sin(kr)}{kr}, \tag{2.94}$$

and

$$S_{\uparrow\uparrow}(k) = 1 + \frac{2}{3\pi} \int_0^\infty dr r^2 k_F^3 [g_{\uparrow\uparrow}(k_F r) - 1] r^2 \frac{\sin(kr)}{kr}, \tag{2.95}$$

where $r$ is radial coordinate, $k_F = (3\pi^2 n)^{1/3}$ is the Fermi wave vector.

For the DMC, the definition of pair correlation function is estimated using mixed estimator

$$g(r) = \frac{1}{4\pi r^2 V} \frac{N(N - \delta_{\sigma_1,\sigma_2})}{n_1 n_2} \frac{\sum_{j,|\mathbf{r}_{1j}-\mathbf{r}_{2j}=r|} W_j}{\sum_i W_i} \tag{2.96}$$

where $\delta_{\sigma_1,\sigma_2}$ is 1 for the same spin and 0 for different spins, $W_i$ is the weight for the walker $i$, while $W_j$ is the weight of walker $j$ in which particle 1 is located at the distance $r$ from the particle 2.

### 2.5.4 One-body and two-body density matrices

One-body density matrix for zero temperature is defined as

$$\rho_1(\mathbf{r}, \mathbf{r}') = \left\langle \Phi^\dagger(\mathbf{r})\Phi(\mathbf{r}') \right\rangle = \frac{N \int d\mathbf{r}_2 \cdots d\mathbf{r}_N \Psi_0^*(\mathbf{r}, \mathbf{r}_2 \cdots \mathbf{r}_N)\Psi_0(\mathbf{r}', \mathbf{r}_2 \cdots \mathbf{r}_N)}{\int d\mathbf{R}\Psi_0^*(\mathbf{R})\Psi_0(\mathbf{R})}, \tag{2.97}$$

It can also be written in the momentum space as

$$\rho_1(\mathbf{r}, \mathbf{r}') = \frac{1}{V} \sum_{\mathbf{k},\mathbf{l}} e^{i(\mathbf{k}\cdot\mathbf{x}-\mathbf{l}\cdot\mathbf{y})} \left\langle c_\mathbf{k}^\dagger c_\mathbf{l} \right\rangle, \tag{2.98}$$

where $c_\mathbf{k}^\dagger$ and $c_\mathbf{k}$ are the creation and annihilation operator for the plane wave with momentum $\mathbf{k}$.

In a translationally invariant system, the momentum operator $\hat{P}$ commutes with the Hamiltonian $\hat{H}$, therefore

$$\left\langle [c_\mathbf{k}^\dagger c_\mathbf{l}, \hat{P}] \right\rangle = 0. \tag{2.99}$$

On the other hand,

$$[c_\mathbf{k}^\dagger c_\mathbf{l}, \hat{P}] = \hbar(\mathbf{l} - \mathbf{k}) c_\mathbf{k}^\dagger c_\mathbf{l}, \tag{2.100}$$

Therefore for a translationally invariant system,

$$\left\langle c_\mathbf{k}^\dagger c_\mathbf{l} \right\rangle = \delta_{\mathbf{k},\mathbf{l}} \left\langle n_\mathbf{k} \right\rangle, \tag{2.101}$$

where $n_\mathbf{k}$ is the number operator for atoms with momentum $\mathbf{k}$.

The one-body density matrix (OBDM) of the translational invariant system can then be written as

$$\rho_1(\mathbf{r}, \mathbf{r}') = \frac{N_0}{V} + \int \frac{d^3k}{(2\pi)^3} e^{i\mathbf{k}(\mathbf{r}-\mathbf{r}')} \left\langle n_\mathbf{k} \right\rangle \tag{2.102}$$

Where $N_0$ is the number of atoms in the ground state of one particle orbital.

From the long-range 0ff-diagonal OBDM one can obtain indication on long-range order in

bosonic systems, in particular,

$$\rho_1(\mathbf{r},\mathbf{r}') \xrightarrow{|\mathbf{r}-\mathbf{r}'|\to\infty} \frac{N_0}{V} \tag{2.103}$$

Since $n_{\mathbf{k}}$ is bounded and the expotential $e^{i\mathbf{k}(\mathbf{r}-\mathbf{r}')}$ oscillates quickly as the distance between $\mathbf{r}$ and $\mathbf{r}'$ become large. For the bosonic system, it is possible that $N_0$ reads macroscorpic values, which is a sufficient criteria for the Boson-Einstein condensate(BEC). It should be noted that $N_0$ in this case is equal or smaller than the largest eigenvalue of the one-body density matrix, as will be shown below. The existence of the off diagonal long range order can be used as a sufficient condition for the existence of super-conductivity or super-fluidity, as proposed by Yang[79].

The direct Fourier transform of OBDM, as seen in Eq. 2.102, gives the momentum distribution of the system,

$$\left\langle n_{\mathbf{k}} \right\rangle = \int d\mathbf{k}\rho_1(\mathbf{r},\mathbf{r}')e^{-i\mathbf{k}(\mathbf{r}-\mathbf{r}')}. \tag{2.104}$$

In the DMC calculation, the OBDM for the homogeneous system is calculated using the mixed estimator

$$\begin{aligned}
\rho_1(\mathbf{r}+\mathbf{r}_0,\mathbf{r}) &= \frac{N\int d\mathbf{r}_2\cdots d\mathbf{r}_N \Psi_T^*(\mathbf{r}+\mathbf{r}_0,\mathbf{r}_2\cdots\mathbf{r}_N)\Psi_0(\mathbf{r},\mathbf{r}_2\cdots\mathbf{r}_N)}{\int d\mathbf{R}\Psi_0^*(\mathbf{R})\Psi_T(\mathbf{R})} \\
&= \frac{N\int d\mathbf{r}_1 d\mathbf{r}_2\cdots d\mathbf{r}_N \frac{\Psi_T^*(\mathbf{r}+\mathbf{r}_0,\mathbf{r}_2\cdots\mathbf{r}_N)}{\Psi_T^*(\mathbf{r},\mathbf{r}_2\cdots\mathbf{r}_N)}\Psi_T(\mathbf{r},\mathbf{r}_2\cdots\mathbf{r}_N)\Psi_0(\mathbf{r},\mathbf{r}_2\cdots\mathbf{r}_N)}{V\int d\mathbf{R}\Psi_0^*(\mathbf{R})\Psi_T(\mathbf{R})} \\
&= \frac{N\sum_i w_i \frac{\Psi_T^*(\mathbf{r}_i+\mathbf{r}_0,\mathbf{r}_{2i}\cdots\mathbf{r}_{Ni})}{\Psi_T^*(\mathbf{r}_i,\mathbf{r}_{2i}\cdots\mathbf{r}_{Ni})}}{V\sum_i w_i},
\end{aligned} \tag{2.105}$$

where index $i$ runs over all walkers and $i'$ runs over walkers that in the volume $d\mathbf{R}$.

For some more general system such as trapped systems, or systems with hard wall boundaries, one may define expansion of $\Phi(\mathbf{r})$ in natural orbitals, as[37],

$$\Phi(\mathbf{r}) = \sum_i \phi_i(\mathbf{r})\hat{a}_i, \tag{2.106}$$

In this way, assuming the the usual commutation and number relations we get

$$[\hat{a}_i^\dagger, \hat{a}_j] = \delta_{ij},\ <\hat{a}_i^\dagger\hat{a}_j>= N_i\delta_{ij}. \tag{2.107}$$

OBDM can be written as

$$\rho_1(\mathbf{r},\mathbf{r}') = \sum_{ij}\phi_j^*(\mathbf{r})\phi_i(\mathbf{r})N_i\delta_{ij}. \tag{2.108}$$

The momentum distribution can be extracted by noting that

$$\tilde{\phi}_i(\mathbf{k}) = \frac{1}{(2\pi)^{3/2}} \int d\mathbf{r} e^{-i\mathbf{k}\cdot\mathbf{r}} \phi_i(\mathbf{r}), \tag{2.109}$$

and

$$n(\mathbf{k}) = \sum_i n_i |\tilde{\phi}_i(k)|^2. \tag{2.110}$$

so that the momentum can be represented by

$$n(\mathbf{k}) = \frac{1}{(2\pi)^3} \int d\mathbf{r} d\mathbf{r}' \rho_1(\mathbf{r}, \mathbf{r}') e^{i\mathbf{k}(\mathbf{r}-\mathbf{r}')}, \tag{2.111}$$

For this derivation, no specific boundary conditions are required. For a system with spherical symmetry, this formula can be further reduced to

$$n(|\mathbf{k}|) = \frac{1}{(2\pi)^3} \int d\mathbf{r}_0 d\mathbf{r} \rho_1(\mathbf{r}_0 + \mathbf{r}, \mathbf{r}) \frac{\sin(kr_0)}{kr_0}, \tag{2.112}$$

and by expanding plane waves we get

$$e^{i\mathbf{k}\cdot\mathbf{r}} = \sum_l (2l+1) i^l j_l(kr) P_l(\hat{\mathbf{k}} \cdot \hat{\mathbf{r}}). \tag{2.113}$$

Note that in Eq. 2.113, only $l = 0$ survives as is required by the spherical symmetry. $P_l$ in Eq. 2.113 is the usual Legendre polynomial.

The momentum distribution can be readily implemented by both VMC and DMC algorithm, written as

$$n(|\mathbf{k}|) = \frac{N}{2\pi^2} \int d\mathbf{r}_1, \cdots \mathbf{r}_N |\Psi_T(\mathbf{r}_1, \cdots, \mathbf{r}_N)|^2 \int_0^\infty dr_0 r_0^2 \frac{\sin(kr_0)}{kr_0} \frac{\Psi_T(\mathbf{r}_1 + \mathbf{r}_0, \cdots, \mathbf{r}_N)}{\Psi_T(\mathbf{r}_1, \cdots, \mathbf{r}_N)}, \tag{2.114}$$

for VMC or

$$n(|\mathbf{k}|) = \frac{N}{2\pi^2} \int d\mathbf{r}_1 \cdots \mathbf{r}_N \Psi_0^*(\mathbf{r}_1, \cdots, \mathbf{r}_N) \Psi_T(\mathbf{r}_1, \cdots, \mathbf{r}_N) \times \int_0^\infty dr_0 r_0^2 \frac{\sin(kr_0)}{kr_0} \frac{\Psi_T(\mathbf{r}_1 + \mathbf{r}_0, \cdots, \mathbf{r}_N)}{\Psi_T(\mathbf{r}_1, \cdots, \mathbf{r}_N)}, \tag{2.115}$$

for DMC. The orientation of $\mathbf{r}_0$ can be choosen arbitrarily or integrated out.

The two-body density matrix (TBDM) is defined as

$$\rho_2(\mathbf{r}_1', \mathbf{r}_2', \mathbf{r}_1, \mathbf{r}_2) = \left\langle \Psi_\uparrow^\dagger(\mathbf{r}_1') \Psi_\downarrow^\dagger(\mathbf{r}_2') \Psi_\uparrow(\mathbf{r}_1) \Psi_\downarrow(\mathbf{r}_2) \right\rangle. \tag{2.116}$$

If the fermions form Cooper pairs or molecules and achieved Bose-Einstein condensate, the largest eigenvalue of the two-body density matrix should be of order $N/2$ for the spin unpolarized system. Furthermore, the projected two-body density matrix, defined as

$$\rho_2^P(r) = \frac{2}{N}\int d\mathbf{r}_1 d\mathbf{r}_2 \rho_2(\mathbf{r}_1+\mathbf{r}, \mathbf{r}_2+\mathbf{r}, \mathbf{r}_1, \mathbf{r}_2), \tag{2.117}$$

will converge to the condensate fraction $\alpha$ as the distance $\mathbf{r}$ goes to infinity,

$$\lim_{r\to\infty} \rho_2^P(r) = \alpha. \tag{2.118}$$

Similarly as in OBDM case, the projected TBDM can be directly implemented for VMC as

$$\begin{aligned}\rho_2^P(r) &= \frac{N(N-\delta_{1,2})}{4V^2}\frac{\int d\mathbf{r}_1\cdots d\mathbf{r}_N |\Psi_T(\mathbf{r}_1,\mathbf{r}_2,\mathbf{r}_3,\cdots,\mathbf{r}_N)|^2 \frac{\Psi_T^*(\mathbf{r}_1+\mathbf{r},\mathbf{r}_2+\mathbf{r},\mathbf{r}_3,\cdots,\mathbf{r}_N)}{\Psi_T^*(\mathbf{r}_1,\mathbf{r}_2,\mathbf{r}_3,\cdots,\mathbf{r}_N)}}{\int d\mathbf{r}_1\cdots d\mathbf{r}_N \Psi_T^*(\mathbf{r}_1,\mathbf{r}_2,\mathbf{r}_3,\cdots,\mathbf{r}_N)\Psi_T(\mathbf{r}_1,\mathbf{r}_2,\mathbf{r}_3,\cdots,\mathbf{r}_N)} \\ &= \frac{\sum_i w_i \frac{\Psi_T^*(\mathbf{r}_{1i}+\mathbf{r},\mathbf{r}_{2i}+\mathbf{r},\mathbf{r}_{3i},\cdots,\mathbf{r}_{Ni})}{\Psi_T^*(\mathbf{r}_{1i},\mathbf{r}_{2i},\mathbf{r}_{3i},\cdots,\mathbf{r}_{Ni})}}{\sum_i w_i}.\end{aligned} \tag{2.119}$$

and for DMC as

$$\begin{aligned}\rho_2^P(r) &= \frac{N(N-\delta_{1,2})}{4V^2}\frac{\int d\mathbf{r}_1\cdots d\mathbf{r}_N \Psi_0(\mathbf{r}_1,\mathbf{r}_2,\mathbf{r}_3,\cdots,\mathbf{r}_N)\Psi_T^*(\mathbf{r}_1,\mathbf{r}_2,\mathbf{r}_3,\cdots,\mathbf{r}_N)\frac{\Psi_T^*(\mathbf{r}_1+\mathbf{r},\mathbf{r}_2+\mathbf{r},\mathbf{r}_3,\cdots,\mathbf{r}_N)}{\Psi_T^*(\mathbf{r}_1,\mathbf{r}_2,\mathbf{r}_3,\cdots,\mathbf{r}_N)}}{\int d\mathbf{r}_1,\cdots,\mathbf{r}_N \Psi_0^*(\mathbf{r}_1,\mathbf{r}_2,\mathbf{r}_3,\cdots,\mathbf{r}_N)\Psi_T((\mathbf{r}_1,\mathbf{r}_2,\mathbf{r}_3,\cdots,\mathbf{r}_N)} \\ &= \frac{\sum_i w_i \frac{\Psi_T^*(\mathbf{r}_{1i}+\mathbf{r},\mathbf{r}_{2i}+\mathbf{r},\mathbf{r}_{3i},\cdots,\mathbf{r}_{Ni})}{\Psi_T^*(\mathbf{r}_{1i},\mathbf{r}_{2i},\mathbf{r}_{3i},\cdots,\mathbf{r}_{Ni})}}{\sum_i w_i}.\end{aligned} \tag{2.120}$$

where $w_i$ is the weight of the $i$th walker which is equal to one in VMC and belongs to a cutoff range around one for DMC, $r_1$ and $r_2$ can be the same spin or different spins and $\delta_{1,2}$ will be 1 if they are the same spin and zero otherwise. Eq. 2.120 uses mixed estimator and there will be some bias present in the results(besides the fixed-node error). However, if the variational wave function is very close to the true ground, this bias should be negligible.

Recently, there has been an proposed approach[5] of directly solving for the eigenvalues and eigenfunction of the one-body and two-body density matrices using statistical formulation of QMC. This approach has the advantage that it is not limited by the requirement of translational invariance, and hence is useful in finding the momentum distribution and condensate fraction for some more realistic systems such as the system confined to a hard wall sphere, or in a harmonic trap. The eigenvalue problem of the OBDM can be written as

$$\int d\mathbf{r}' \rho_1(\mathbf{r},\mathbf{r}')\phi_0(\mathbf{r}') = N_c\phi_0(\mathbf{r}) \tag{2.121}$$

where $\phi_0(\mathbf{r})$ is the eigenvector of the OBDM with the largest eigenvalue and $N_c$ is the corresponding eigenvalue. The algorithm take advantage of the fact that iterative multiplication of the matrix by a unit vector and renormalization, it will gradually rotate to the eigenstate with largest eigenvalue, i.e.,

$$\int d\mathbf{r}'\rho_1(\mathbf{r},\mathbf{r}')\phi_0^i(\mathbf{r}') = N_c^i\phi_0^{i+1}(\mathbf{r}') \tag{2.122}$$

and

$$\int d\mathbf{r}d\mathbf{r}'\rho_1(\mathbf{r},\mathbf{r}')\phi_0^{*i}(\mathbf{r})\phi_0^i(\mathbf{r}') = N_c^i \tag{2.123}$$

where $\phi_0^i$ is the the trial eigenvector after $i$ multiplications. It can be shown that

$$\phi_0^i(\mathbf{r}) \xrightarrow{i\to\infty} \phi_0(\mathbf{r}), \tag{2.124}$$

$$N_c^i \xrightarrow{i\to\infty} N_c \tag{2.125}$$

Also,

$$N_c^i \le N_c \tag{2.126}$$

To prove Eq. 2.126, note the fact that any $\phi_0^i(\mathbf{r})$ can be expanded in the eigenstates of OBDM,

$$\phi_0^i(\mathbf{r}) = \sum_j c_j\phi_j(\mathbf{r}), \tag{2.127}$$

$$\sum_j |c_j|^2 = 1. \tag{2.128}$$

where $c_j$ are the expansion coefficents, therefore

$$N_c^i = \sum_{i=0}^{\infty} N_i|c_j|^2 \le N_c\sum_{i=0}^{\infty}|c_j|^2 = N_c, \tag{2.129}$$

where $N_c$ is the largest eigenvalue of the OBDM.

This iterative algorithm can be implemented in DMC as

$$\begin{aligned}\frac{N_c^i}{N}\phi_0^{i+1} &= \int d\mathbf{r}_1\cdots\mathbf{r}_N\left[\phi_0^i(\mathbf{r}_1)\frac{\Psi_T^*(\mathbf{r},\mathbf{r}_2,\cdots,\mathbf{r}_N)}{\Psi_T^*(\mathbf{r}_1,\mathbf{r}_2,\cdots,\mathbf{r}_N)}\right]\Psi_T^*(\mathbf{r}_1,\mathbf{r}_2,\cdots,\mathbf{r}_N)\Psi_0(\mathbf{r}_1,\mathbf{r}_2,\cdots,\mathbf{r}_N)\\ &= \sum_j w_j\phi_0^i(\mathbf{r}_{1j})\frac{\Psi_T^*(\mathbf{r},\mathbf{r}_{2j},\cdots,\mathbf{r}_{Nj})}{\Psi_T^*(\mathbf{r}_{1j},\mathbf{r}_{2j},\cdots,\mathbf{r}_{Nj})},\end{aligned} \tag{2.130}$$

and

$$\frac{N_c^i}{N} = \int d\mathbf{r}\phi_0^{i+1*}(\mathbf{r})\phi_0^i(\mathbf{r}) \tag{2.131}$$

where index $j$ runs over all of the walkers, and $w_j$ is weight of jth walker,

For DMC calculation, since the mixed estimator is used, Eq. 2.126 will not necessarily hold. However, as the trial wave function $\Psi_T(\mathbf{R})$ is sufficiently close to the true ground state $\Psi_0(\mathbf{R})$ and large number of samples are taken, the error of estimated eigenvalue is relatively small.

The eigenvalue of the two-body density matrix can be written similarly

$$\int d\mathbf{r_1}'\mathbf{r_2}'\rho_2(\mathbf{r_1},\mathbf{r_2};\mathbf{r_1'},\mathbf{r_2'})\phi_0^i(\mathbf{r_1'},\mathbf{r_2'}) = N_{p0}^i\phi_0^{i+1}(\mathbf{r_1},\mathbf{r_2}), \tag{2.132}$$

where $\phi_0^i(\mathbf{r_1'},\mathbf{r_2'})$ is the trial two-body eigenvector and $N_{p0}^i$ is two-body eigenvalue.

Similarly as Eq. 2.130, the eigenvector with the largest eigenvalue of two-body density matrix can be calculated using similar strategy,

$$\frac{N_{p0}}{(N/2)^2}\phi_0^{i+1}(\mathbf{r_1},\mathbf{r_2}) = \int d\mathbf{r}_1\cdots d\mathbf{r}_N\phi_0^i(\mathbf{r_1'},\mathbf{r_2'})\frac{\Psi_T^*(\mathbf{r_1},\mathbf{r_2},\cdots,\mathbf{r}_N)}{\Psi_T^*(\mathbf{r_1'},\mathbf{r_2'},\cdots,\mathbf{r}_N)}\times \Psi_T^*(\mathbf{r}_1,\mathbf{r}_2,\cdots,\mathbf{r}_N)\Psi_0(\mathbf{r}_1,\mathbf{r}_2,\cdots,\mathbf{r}_N), \tag{2.133}$$

and

$$\frac{N_{p0}}{(N/2)^2} = \int d\mathbf{r_1}\mathbf{r_2}\phi_0^{i+1*}(\mathbf{r_1},\mathbf{r_2})\phi_0^i(\mathbf{r_1},\mathbf{r_2}). \tag{2.134}$$

Without taking the symmetry into account, the eigenvector for the two-body density matrix contains 6 independent coordinates, therefore it is a much larger parameter space, and in general, much harder to evaluate. However, for a system with explicit symmetry such as spherical symmetry, the independent coordinates can be reduced to 3 and easier to calculate. In practice, the 3 independent coordinates are discretized into mesh points and using einspline package[39] interpolated to continuous values.

## 2.6 Optimization method

The DMC mehod has a zero variance property, i.e. the local energy

$$E_{\rm loc}(\mathbf{R}) = \frac{\hat{H}\Psi(\mathbf{R})}{\Psi(\mathbf{R})}, \tag{2.135}$$

becomes a constant equal to ground state energy if the trial wave function is the exact ground state solution. Therefore the trial wave function with multiple parameters may be optimized by adjusting the parameters which minimize the energy or the variance, or a linear combination of the two. Algorithm like Newton's method, steepest descent method or Levenberg-Marquardt method require the energy or variance derivatives and Hessian with respect to the parameter set[8]. Suppose the trial wave function has a set of parameters {c}, the average energy maybe

written as

$$E^{\{c\}} = \frac{\int d\mathbf{R}|\Psi(\mathbf{R})|^2 E_{\rm loc}^{\{c\}}(\mathbf{R})}{\int d\mathbf{R}|\Psi(\mathbf{R})|^2} \tag{2.136}$$

and variance can be written as

$$(\sigma^{\{c\}})^2 = \frac{\int d\mathbf{R}|\Psi(\mathbf{R})|^2 (E_{\rm loc}^{\{c\}}(\mathbf{R}) - E^{\{c\}})^2}{\int d\mathbf{R}|\Psi(\mathbf{R})|^2} \tag{2.137}$$

where the dependence on parameter $\{c\}$ of the wave function has been omitted.

The variance minimization procedure requires the gradient of variance with respect to the optimization parameters, the derivative of given parameter $c_i$ for $E^{\{c\}}$ and $(\sigma^{\{c\}})^2$ can be straightforwardly calculated as

$$\frac{\partial E^{\{c\}}}{\partial c_i} = \big\langle \frac{\Psi_{,i}}{\Psi} E_{\rm loc} + \frac{H\Psi}{\Psi} - 2E^{\{c\}} \frac{\Psi_{,i}}{\Psi} \big\rangle = 2\big\langle \frac{\Psi_{,i}}{\Psi}(E_{\rm loc} - E^{\{c\}}) \big\rangle, \tag{2.138}$$

and

$$\frac{\partial (\sigma^{\{c\}})^2}{\partial c_i} = 2\left[ \big\langle E_{\rm loc,i}(E_{\rm loc} - E^{\{c\}} \big\rangle + \big\langle \frac{\Psi_{,i}}{\Psi} E_{\rm loc}^2 \big\rangle \big\langle \frac{\Psi_{,i}}{\Psi} \big\rangle \big\langle E_{\rm loc}^2 \big\rangle - 2E^{\{c\}} - \big\langle \frac{\Psi_{,i}}{\Psi}(E_{\rm loc} - E^{\{c\}}) \big\rangle \right], \tag{2.139}$$

where the the subscript $,i$ denotes derivative $\frac{\partial}{\partial c_i}$.

Similarly, the Hessian for $E^{\{c\}}$ and $(\sigma^{\{c\}})^2$ can be calculated from

$$\frac{\partial^2 E^{\{c\}}}{\partial^2 c_i c_j} = 2\left[ \big\langle \big( \frac{\Psi_{,i,j}}{\Psi} + \frac{\Psi_{,i}\Psi_{,j}}{\Psi^2}(E_{\rm loc} - E^{\{c\}}) \big\rangle - \big\langle \frac{\Psi_{,i}}{\Psi} \big\rangle E_{,j}^{\{c\}} - \big\langle \frac{\Psi_{,j}}{\Psi} \big\rangle E_{,i}^{\{c\}} + \big\langle \frac{\Psi_{,i}}{\Psi} E_{{\rm loc},j} \big\rangle \right], \tag{2.140}$$

and

$$\frac{\partial^2 (\sigma^{\{c\}})^2}{\partial^2 c_i c_j} = \big\langle (E_{{\rm loc},i} - E^{\{c\}})(E_{{\rm loc},j} - E^{\{c\}}) \big\rangle. \tag{2.141}$$

The minimization procedure can use cost function other than energy or variance, for example, the mixed cost function

$$f(E^{\{c\}}, (\sigma^{\{c\}})^2) = \alpha E^{\{c\}} + (1-\alpha)(\sigma^{\{c\}})^2, \tag{2.142}$$

or the absolute value cost function

$$f(E^{\{c\}}, \sigma^2) = < |E_{\rm loc} - E^{\{c\}}| > . \tag{2.143}$$

In practice, the mixed minimization procedure[76], which uses the mixed cost function, is

more stable over either variance minimization or energy minimization. The mixing parameter $\alpha$ is usually chosen between 0.85 and 0.95. Also, for some cases the provided trial wave function converges to an excited state which may cause the orthogonality problem, i.e., the trial wave function overlap with ground state wave function is too small to correctly project out the ground state. In these cases, multiple random guess of initial parameters can be used to explore the global minimum in the whole parameter space.

## 2.7 Summary

In this Chapter we discussed the basic Monte Carlo techniques that are relevant to the our study including the Metropolis algorithm, variational Monte Carlo, diffusion Monte Carlo and reptation Monte Carlo. The observables of interest such as pair correlation function, one-body and two-body density matrices have also been introduced. Quantum Monte Carlo methods provide techniques to evaluate ground state energies and related quantities for a given many-body Hamiltonian. The only approximation involved in the fixed-node diffusion Monte Carlo, the fixed-node approximation, usually cause a energy bias of $3 \sim 5$ percent of the correlation energy. Under this approximation, diffusion and reptation Monte Carlo still provide strict upper bounds for the energy estimations. The fixed-node approximation can be further relaxed through the released-node method. Although the convergence can be too slow for practical calculations, the released-node energy should converge to the true ground state energy after time inverse to the Fermi energy $E_F$.

# Chapter 3

# Theory of unpolarized Fermi gas

This Chapter gives a brief introduction for the theory of unpolarized Fermi gas. First the two-body problem is discussed. The two-body problem can be solved exactly either analytically or numerically and provides a starting point to treat the many-body problem. We then proceed to introduce the equation of state for the unpolarized Fermi gas for both BCS and BEC regimes. The free and interacting Fermi gas in harmonic trap are also discussed, and we focus on introducing to the density profile within the local density approximation(LDA) with the purpose of making comparisons to the DMC simulation results.

## 3.1 Two-body scattering

### 3.1.1 General theory

The scattering of two atoms enables us to gain some insight into the many-body problem and is the starting point to build the many-body wave function. The general Schrödinger equation of two atoms with mass $m_1$, $m_2$ and with interaction $V(\mathbf{r_1}-\mathbf{r_2})$ can be written as(set $\hbar = 1$)

$$\left(-\frac{1}{2m_1}\nabla_1^2 - \frac{1}{2m_2}\nabla_2^2 + V(\mathbf{r_1}-\mathbf{r_2})\right)\phi(\mathbf{r_1},\mathbf{r_2}) = E\phi(\mathbf{r_1},\mathbf{r_2}). \tag{3.1}$$

Without external forces, the center of mass of the two atoms can be separated from the relative motion,

$$\phi(\mathbf{r_1},\mathbf{r_2}) = \phi_{\mathrm{cm}}(\mathbf{R})\phi_{\mathrm{r}}(\mathbf{r}) \tag{3.2}$$

The center of mass coordinate $\mathbf{R}$ and relative coordinate $\mathbf{r}$ are given by

$$\begin{aligned} \mathbf{R} &= \frac{m_1\mathbf{r_1}+m_2\mathbf{r_2}}{m_1+m_2}, \\ \mathbf{r} &= \mathbf{r_1}-\mathbf{r_2}. \end{aligned} \tag{3.3}$$

The two-body interacting equation Eq. 3.1 can be rewritten as

$$\left(-\frac{1}{2M}\nabla^2_{\mathbf{R}} - \frac{1}{2\mu}\nabla^2_{\mathbf{r}} + V(r)\right)\phi_{\rm cm}(\mathbf{R})\phi_{\rm r}(\mathbf{r}) = E\phi_{\rm r}(\mathbf{r}) \tag{3.4}$$

where $M = m_1 + m_2$ and $\mu = \frac{m_1 m_2}{m_1+m_2}$. Eq. 3.4 can be directly separated as

$$\begin{aligned} -\frac{1}{2M}\nabla^2_{\mathbf{R}}\phi_{\rm cm}(\mathbf{R}) &= E_{\rm cm}\phi_{\rm cm}(\mathbf{R}), \\ \left(-\frac{1}{2\mu}\nabla^2_{\mathbf{r}} + V(\mathbf{r})\right)\phi_{\rm r}(\mathbf{r}) &= E_{\rm r}\phi_{\rm r}(\mathbf{r}), \\ E &= E_{\rm cm} + E_{\rm r}. \end{aligned} \tag{3.5}$$

The center of mass equation has the simple solution

$$\begin{aligned} \phi_{\rm cm}(\mathbf{R}) &= e^{i\mathbf{k}_{\rm cm}\cdot\mathbf{R}}, \\ E_{\rm cm} &= \frac{k^2_{\rm cm}}{2M}. \end{aligned} \tag{3.6}$$

And the two-body problem is reduced to solve the equation of relative motion. We make further assumption that the interaction term $V(\mathbf{r})$ depends only on the relative distance, so that the equation can be further decomposed as

$$\frac{d^2u_l(r)}{dr^2} + \left(2\mu E_{\rm r} - 2\mu V(r) - \frac{l(l+1)}{r^2}u_l(r)\right) = 0, \tag{3.7}$$

where $u_l(r) = r\phi_{\rm r}(r)$.

For the S-wave with $l = 0$, the Eq. 3.7 can be reduced to a simpler form,

$$-\frac{1}{2\mu}\frac{d^2u(r)}{dr^2} + V(r)u(r) = E_{\rm r}u(r). \tag{3.8}$$

The general solution of $u(r)$ can be written as,

$$u(r) = \sin(kr + \delta(k)), \tag{3.9}$$

where

$$k = \sqrt{2\mu E_{\rm r}}. \tag{3.10}$$

$k$ is the momentum of incoming and outgoing wave vector(elastic collision with the range of $V(r)$ finite), and $\delta(k)$ is the S-wave phase shift. When the scattering energy $E_{\rm r}$ is low and wave vector $k$ is small, the scattering can be described by a single parameter, the S-wave scattering

length, which is defined as

$$a_s = -\lim_{k\to 0} \frac{\delta(k)}{k}, \tag{3.11}$$

In the limit of zero momentum scattering, the solution may be written as

$$\phi_{\mathrm{r}}(r) \xrightarrow{k\to 0} C(1 - \frac{a_s}{r}), \tag{3.12}$$

where C is some constant. Therefore, $a_s$ can be equivalently defined as the first node of the scattering wave function in small wave vector limit.

### 3.1.2 Scattering of Pöschl-Teller potential

In this thesis, the interest is focused on the point like attractive interaction that has zero range. We use the Pöschl-Teller potential, which has can be solved analytically, to mimic the delta function when the effective range of the potential is extrapolated to 0. The Pöschl-Teller potential can also be used as explicit example of the general two-body scattering theory that is developed in the last section.

The Pöschl-Teller potential is written as

$$V(r) = -\frac{\lambda(\lambda-1)u_0^2}{\cosh^2(u_0 r)}, \tag{3.13}$$

Where $\lambda$ is the parameter which controls the scattering length, and $u_0$ is the inverse of effective range

$$u_0 = 2/R_{\mathrm{eff}}. \tag{3.14}$$

The scattering length of the potential may be written as [42]

$$\frac{a_s}{R_{\mathrm{eff}}} = \frac{\pi}{2}\cot(\frac{\pi\lambda}{2}) + \gamma + f(\lambda), \tag{3.15}$$

where $\gamma$ is the Euler constant and $f(\lambda)$ is the digamma function.

## 3.2 Equation of state for BCS and BEC regime

The S-wave scattering length of two atoms with different spin for the unpolarized Fermi gas is used to characterize many body phases,

$$\begin{aligned} &1/(k_F a_s) < -1 : \text{Weakly interacting Fermi gas} \\ &1/(k_F a_s) = 0 : \text{Unitary limit} \\ &1/(k_F a_s) > 1 \to 0+ : \text{Bose} - \text{Einstein condensate}, \end{aligned} \tag{3.16}$$

when $1/k_F a_s$ is tuned from $-1$ to 1, the system goes for a smooth transition from the Bardeen-Cooper-Schrieffer (BCS) to Bose-Einstein condensate(BEC) regime. Since there is no symmetry breaking in this process, this transition is a crossover instead of a phase transition, the so called BCS-BEC crossover.

The equation of state for the weakly attractive gas is given by [50, 59]

$$\frac{E}{E_{\text{free}}} = 1 + \frac{10}{9\pi} k_F a_s + \frac{4(11 - 2\log 2}{21\pi^2} (k_F a_s)^2 + \cdots, \tag{3.17}$$

where $E_{\text{free}}$ is the energy for the non-interacting Fermi gas.

On the BEC side, when $\frac{1}{k_F a_s} > 1$, the the energy is the same with a repulsive molecule gas,

$$\frac{E - N(\epsilon_b)/2}{E_{\text{free}}} = \frac{5}{18\pi} k_F a_m \left[1 + \frac{128}{15\sqrt{6\pi^3}} (k_F a_m)^{3/2} + \cdots\right], \tag{3.18}$$

where $\epsilon_b$ is the binding energy between the molecules, $a_m$ is the positive molecule molecule scattering length and [60]

$$a_m = 0.6 a_s. \tag{3.19}$$

At the crossover regime where $|\frac{1}{k_F a_s}| < 1$, there's no known analytical solution for the equation of state, and this is the subject that is studied by DMC previously[4].

## 3.3 Fermi gas in the harmonic trap

The Fermi gas is in a harmonic trap is worth to study for a number of reasons. First, all the real cold atom experiments are carried out in traps. Also, the trapped system has a number of interesting features in itself, such as the hidden SO(2,1) symmetry and it can be mapped to the gas in the free space[78].

### 3.3.1 Ideal Fermi gas in the harmonic trap

In order to consider the true interacting many-body problem, insights may be gained from studying the non-interacting system first. Since the ideal Fermi gas can be solved explicitly, it can also be used to test various assumptions and the results can be compared to the more complicated interacting Fermi gas cases.

For the ideal Fermi gas with no interaction, the Hamiltonian reads

$$\hat{H} = \sum_i -\frac{1}{2m}\nabla_i^2 + \sum_{i'} -\frac{1}{2m}\nabla_{i'}^2 + \sum_i V_{\text{ext}}(\mathbf{r}_i) + \sum_{i'} V_{\text{ext}}(\mathbf{r}_{i'}), \tag{3.20}$$

where $i$ and $i'$ are indices for spin up and spin down atoms, and $V_{\text{ext}}(r)$ is the isotropic trap

potential,

$$V_{\text{ext}}(r) = \frac{1}{2}m(\omega_x^2 x^2 + \omega_y^2 y^2 + \omega_z^2 z^2). \tag{3.21}$$

The solution for single particle in the harmonic trap reads

$$\begin{aligned}\phi_{i,j,k} = (2^{i+j+k} i!j!k!)^{-1/2}(\frac{m^3\omega_x\omega_y\omega_z}{\pi^3})^{1/4}\times \\ e^{-1/2m(\omega_x x^2+\omega_y y^2+\omega_z z^2)} H_i(\sqrt{m\omega_x}x)H_j(\sqrt{m\omega_y}y)H_k(\sqrt{m\omega_z}z),\end{aligned} \tag{3.22}$$

The energy eigenvalue can be written as

$$E_{i,j,k} = i\omega_x + j\omega_y + k\omega_z + \frac{1}{2}(\omega_x + \omega_y + \omega_z), \tag{3.23}$$

where $i, j, k$ denotes the excitation in $x, y, z$ directions.

The wave function can therefore be written as

$$\Phi(\mathbf{r_1}, \mathbf{r_2}, \cdots \mathbf{r_N}; \mathbf{r_{1'}}, \mathbf{r_{2'}}, \cdots \mathbf{r_{N'}}) = \det \begin{bmatrix} \phi_{0,0,0}(\mathbf{r_1}) & \dots & \phi_{0,0,0}(\mathbf{r_{1'}}) & \dots \\ \phi_{0,0,1}(\mathbf{r_1}) & \ddots & \ddots & \vdots \\ \vdots & \ddots & \ddots & \vdots \\ \dots & \ddots & \ddots & \dots \end{bmatrix} \tag{3.24}$$

Since all the orbitals are orthogonal to each other, the total density can be obtained by adding density of each orbital directly, and the density can be directly computed as

$$n(\mathbf{r}) = 2\sum_{i,j,k} |\phi_{i,j,k}(\mathbf{r})|^2, \tag{3.25}$$

where the summation of combination of index $i, j, k$ run over the lowest energy up to $N$.

The density of non-interacting Fermi gas may also be computed with the local density approximation(LDA), which assumes the occupation of the states as

$$f(\mathbf{r}, \mathbf{k}) = \frac{1}{e^{(\frac{\mathbf{k}^2}{2m} + V(\mathbf{r}) - \mu)/k_B T} + 1}, \tag{3.26}$$

and as $T \to 0$, this gives

$$\begin{aligned} f(\mathbf{r}, \mathbf{k}) &= 1, \frac{\mathbf{k}^2}{2m} + V(\mathbf{r}) \le \mu. \\ &= 0, \frac{\mathbf{k}^2}{2m} + V(\mathbf{r}) > \mu. \end{aligned} \tag{3.27}$$

The density profile is given by

$$n(\mathbf{r}) = 2\int_{|\mathbf{k}|<\sqrt{2m(\mu-V(\mathbf{r}))}} \frac{d^3\mathbf{k}}{(2\pi)^3} = \frac{1}{3\pi^2}\left[2m(\mu - V(\mathbf{r}))\right]^{3/2}. \tag{3.28}$$

where the factor 2 in front accounts for the spin up and spin down channels. At zero temperature, $\mu$ is equal to the Fermi energy $E_F$, which is fixed by

$$N = \int d^3\mathbf{r} n(\mathbf{r}) = \frac{1}{3}(\frac{E_F}{\bar{\omega}})^3, \tag{3.29}$$

where $\bar{\omega} = (\omega_x\omega_y\omega_z)^{1/3}$, and therefore

$$n_F(r) = \frac{1}{3\pi^2}\left(2m(\bar{\omega}(3N)^{1/3} - V(\mathbf{r}))\right)^{3/2}. \tag{3.30}$$

### 3.3.2 Interacting Fermi gas in the harmonic trap

The interacting Fermi gas in the harmonic trap system can be treated similarly as for the gas in free space, where the s-wave scattering length $a_s$ defines the regime of the system.

At the BCS limit, $1/k_F a_s \to -\infty$, the density is in essense similar to the non-interacting case, as the sharp Fermi surface in k-space is only modified very little in the region of the width $\approx k_F e^{-\frac{\pi}{2k_F|a_s|}}$, and as a result, the integration of Eq. 3.28, leading to the similar density profile as is for the non-interacting case.

On the BEC side of large and positive $1/k_F a_s \to \infty$, the Bose-Einstein condensate can be described by the famous Gross-Pitaevskii equation,

$$\left(-\frac{\nabla^2}{2M} + V_M(\mathbf{r}) + g|\Psi_M(\mathbf{r},t)|^2\right)\Psi_M(\mathbf{r},t) = i\frac{\partial}{\partial t}\Psi_M(\mathbf{r},t), \tag{3.31}$$

Where $M = 2m$ is the mass of composite boson and $V_M(r)$ is the external potential for the boson ( We assume spin-up and spin-down atoms that compose the boson are really close),

$$V_M(r) = M(\omega_x^2 + \omega_y^2 + \omega_z^2), \tag{3.32}$$

and $\Psi_M(\mathbf{r},t)$ is the time-dependent wave function for the composite Boson.

At equilibrium, the same dependence of $\Psi_M(\mathbf{r},t)$ can be separated out as

$$\Psi_M(\mathbf{r},t) = e^{-\mathbf{i}E_G t}\Psi_M(\mathbf{r}), \tag{3.33}$$

where $E_G$ is the energy for the ground state, the eigenstate function for the Gross-Pitaevskii

equation may be write as

$$\left(-\frac{\nabla^2}{2M} + V_M(\mathbf{r}) + g|\Psi_M(\mathbf{r})|^2\right)\Psi(\mathbf{r}) = E_G\Psi_M(\mathbf{r}). \tag{3.34}$$

Treating the bosons as ideal gas, the density will be $|\Psi(\mathbf{r})|^2$.

At the unitary limit, the scattering length diverges and the only length scale is the inter-particle spacing $r_s$ or the Fermi wave vector $k_F$. For the Fermi gas with no external potential constrain, the Fermi energy $\epsilon_F$ can be written as $\mu = \xi\epsilon_F$, where $\xi$ is the Bertsch's parameter as is already introduced in Chapter 1. For the trapped Fermi gas, under local density approximation, similar relation also holds locally. Define the local Fermi energy as

$$\epsilon_F(\mathbf{r}) = \epsilon_F - V_{\text{ext}}(\mathbf{r}). \tag{3.35}$$

Similar with the free Fermi gas, the local Fermi energy is related to the density through

$$\epsilon_F(\mathbf{r}) = \frac{1}{2m}(3\pi^2 n(\mathbf{r}))^{2/3}. \tag{3.36}$$

From Eq. 3.35 and Eq. 3.36,

$$n(\mathbf{r}) = \frac{1}{3\pi^2}\left(\frac{2m}{\xi}\right)^{3/2}(\mu - V_{ext}(\mathbf{r}))^{3/2}, \tag{3.37}$$

while $\mu$ is determined by

$$N = \int d\mathbf{r} n(\mathbf{r}) = \frac{1}{3}(\frac{\mu}{\sqrt{\xi}\bar{\omega}})^3, \tag{3.38}$$

which gives

$$\mu = \sqrt{\xi}E_F. \tag{3.39}$$

Therefore, the density profile maybe rewritten as

$$n(\mathbf{r}) = \frac{1}{3\pi^2}\left(\frac{2m}{\xi}\right)^{3/2}(\sqrt{\xi}E_F - V_{ext}(\mathbf{r}))^{3/2}. \tag{3.40}$$

## 3.4 Summary

This chapter gives a brief introduction of the Fermi gas theory, starting from two-body scattering, through concepts of scattering length and phase shift introduced to characterize BCS regime, unitary limit, BEC regime and BCS-BEC crossover. The equation of states in BCS and BEC regimes are introduced, and the non-interacting and unitary Fermi gas in harmonic trap system and their related properties, especially the density profiles, are also described. These can

be calculated and will be compared with exact calculations by DMC methods in the subsequent Chapter.

# Chapter 4

# QMC study of unpolarized Fermi gas at Unitary limit

In this Chapter, comprehensive quantum Monte Carlo results of various quantities of interest for the unpolarized Fermi gas in a periodic box are provided. The first Green's function and diffusion Monte Carlo calculations were carried out in 2003 and 2004[22, 4]. Since then, various QMC calculations have been performed. However, two fundamental questions regarding the ground state energies are still not clear. First, the unitary limit is defined using point-like interactions with the delta-function. However, in real simulations, the interaction with finite effective range are always used. It is therefore important to figure out whether the system really reaches the unitary limit. Second, the DMC provides only the upper-bound for the energy which is determined by the nodal surface of the wave function. Therefore, the question of whether the pair orbitals can be further improved to provide better nodal surface should be addressed. These questions motivate the further study of the unpolarized Fermi gas performed in this Chapter.

## 4.1 Simulation setup

The simulation is performed for unpolarized Fermi gas in a periodic box. The Hamiltonian of the system is written as,

$$H = -\frac{1}{2}\sum_{i=1}^{N/2}\nabla_i^2 - \frac{1}{2}\sum_{i'=1}^{N/2}\nabla_{i'}^2 + \sum_{i,i'}V(r_{ii'}), \tag{4.1}$$

where $N$ is the total number of atoms, $i$ and $i'$ correspond to the spin-up and spin-down atoms, and $r_{ii'}$ denotes the distance $|\mathbf{r}_i - \mathbf{r}_{i'}|$. For convenience, we set mass and Planck constant $m = 1$

and $\hbar = 1$. The interaction $V(r_{ii'})$ is the Pösch-Teller potential introduced in Chapter 3, Section 3.1.2,

$$V(r) = -\frac{\lambda(\lambda-1)u_0^2}{\cosh^2(u_0 r)} \tag{4.2}$$

with $\lambda = 2$, corresponding to effective range $R_{\text{eff}} = \frac{2}{u_0}$ and scattering length $a_s \to \infty$ for all values of $\mu \neq 0$.

The free Fermi gas energy $E_{\text{free}}$ are calculated using the same boundary conditions, and the conversion of free Fermi gas energy to the thermodynamic free gas energy for atom number up to 66 can be found in Appendix A.

The BCS wave function is used as a trial wave function and provides the nodal surface. In order to incorporate correlation between atoms, a Jastrow factor is included,

$$\Psi_T(\mathbf{R}) = \Psi_{\text{BCS}}(\mathbf{R}) e^{J(\mathbf{R})}, \tag{4.3}$$

where the BCS wave function and Jastrow factor is introduced in Chapter 2.

The pair orbital $\phi(\mathbf{r}_i, \mathbf{r}_{i'})$ in $\Psi_{\text{BCS}}$ is written as a linear combination of Gaussian functions

$$\phi(\mathbf{r}_i, \mathbf{r}_{i'}) = \sum_{l,m,n=-1}^{1} \sum_k d_k e^{-\alpha_k(x_i - x_i' + lL)^2} \times e^{-\alpha_k(y_i - y_i' + mL)^2} \times e^{-\alpha_k(z_i - z_i' + nL)^2}, \tag{4.4}$$

where $d_k$ are expansion coefficients, and $\mathbf{r}_i = (x_i, y_i, z_i)$ and $\mathbf{r}_{i'} = (x_{i'}, y_{i'}, z_{i'})$ are coordinates of $i$ and $i'$ atoms inside the simulation box. Sufficiently large exponents $\alpha_k$ are chosen so that only the first neighbour shell of periodic images contributes to the sum, that is, the Gaussian functions are negligible at distances larger than $3L/2$. The pair orbital is smooth with zero derivative at the boundary of the simulation cell. The Jastrow factor $J(\mathbf{R})$ is constructed in a similar way as the pair orbital $\phi(\mathbf{r}_i, \mathbf{r}_{i'})$ and contains contributions for both different spin pairs and same spin pairs.

## 4.2 QMC results

### 4.2.1 Ground state energy

In order to calculate the ground state energy of unpolarized many-body system, the starting point is to calculate first the non-trivial system of unpolarized 4 atoms for benchmark purposes. In order to test the validity of the method, the BCS wave function with two set of pair orbitals, denote as $\phi_a$ and $\phi_b$ are used, where $\phi_a$ is the same as in Eq. 4.4, and $\phi_b$ is written as

$$\phi_b(r) = c_1 f_1(r) + c_2 f_2(r), \tag{4.5}$$

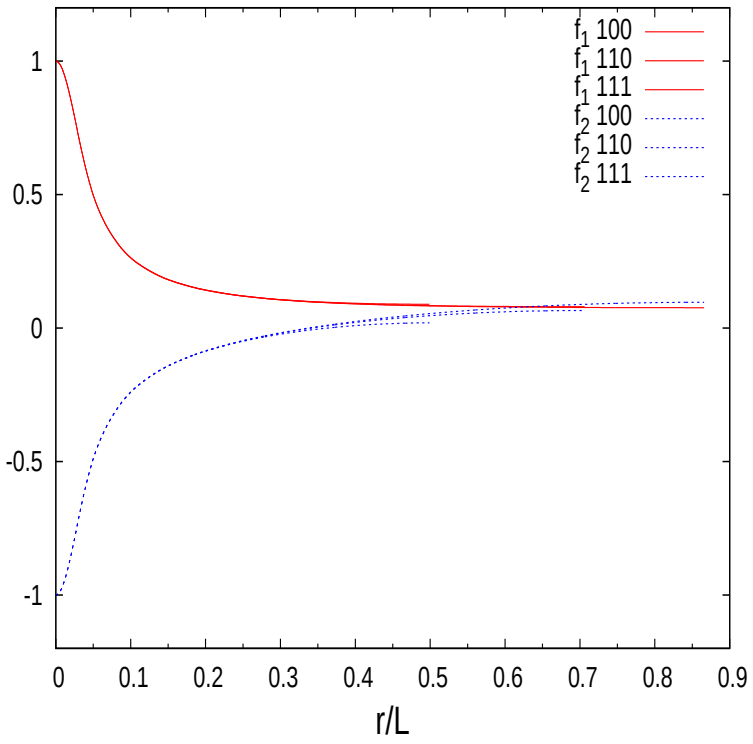


Figure 4.1: The ground state and first excited state in a periodic box using direct diagonalization method. $f_1(r)$ is the ground state and $f_2(r)$ is the first excited state. The three curves for each state represents (100), (110) and (111) direction in the box. The solution converges as the number of basis sets($\sin(r)$ and $\cos(r)$) increase up to 30000.

where $c_1$ and $c_2$ are variational coefficients. $f_1(r)$ and $f_2(r)$ are the ground state and the first excited state solutions of two-body problem in the relative coordinate of periodic box for the given Pöschl-Teller potential, as is shown in Fig. 4.1. The calculation of $f_1(r)$ and $f_2(r)$ are performed by direct diagonlization using $\cos(\mathbf{k}\cdot\mathbf{r})$ and $\sin(\mathbf{k}\cdot\mathbf{r})$ basis, where $\mathbf{k} = 2n\pi/L$, with $L$ being the simulation box size and $n$ integers. About thirty thousand plane wave basis sets are used to make the pair orbital to converge.

The pair orbitals of $\phi_a$ and $\phi_b$ are plotted in Fig. 4.2, it should be noted that although the two pair orbitals are optimized independently, the normalized pair orbital from the tail part almost overlap.

Calculation of ground state energy with VMC and DMC for the four-atom system with $R_{\text{eff}}/r_s = 0.1279$ is shown in Fig. 4.4. In the figure, the BCS-Jastrow wave function of two pair orbitals yields almost the same DMC energy. From the normalized pair orbital of the tail part in Fig. 4.2, it can be deduced that mainly the long tail decides the nodal surface and the head

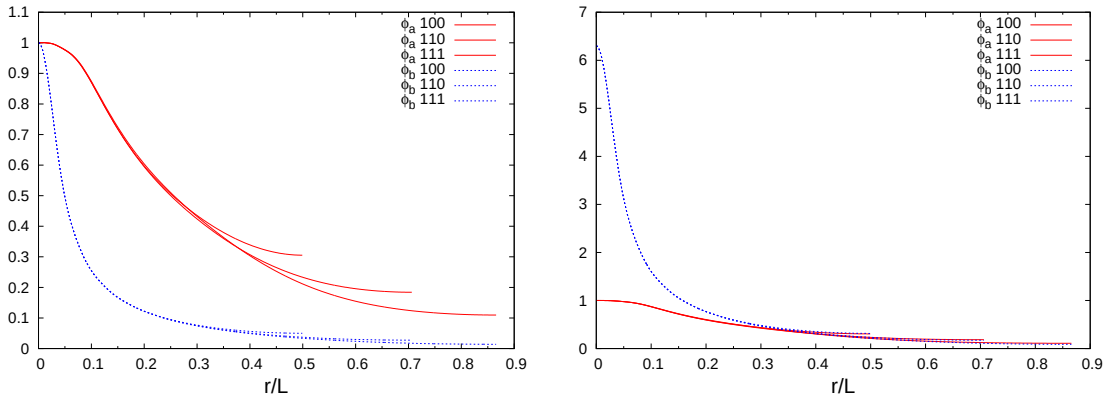


Figure 4.2: Optimized pair orbitals of $\phi_a$ and $\phi_b$ for construction of BCS wave function, the left panel shows the two pairing orbitals normalized in the head part, while the right panel shows the pair orbitals normalized from the tail part.

part of the pair orbital has relatively small influence. As the DMC results indicate the BCS wave function with two pair orbitals $\phi_a$ and $\phi_b$ yields almost the same ground state energy. To verify the validity of the calculation, BCS wave function with pair orbitals $\phi_a(r)$ but without Jastrow factor is also calculated. The results yield larger variance but again almost identical DMC energy. This is well anticipated as the Jastrow factor doesn't change the nodal surface, and as a result, the DMC energy is the same for wave function with same nodal surface.

The DMC results for the unpolarized four-atom system with effective range extrapolation are shown on the upper left panel of Fig. 4.4, as the effective range are extrapolated from $R_{\text{eff}}/r_s = 0.1279$ to $/R_{\text{eff}}/r_s = 0.003998$, the energy drops approximately 10 percent. The final results for the four atom system in the unitary limit with vanishing effective range is 0.212(2). This is comparable to other two indenpendent calculation[17], the direct diagonalization of Hamiltonian yields $\xi = 0.211(2)$ and $\xi = 0.210(2)$, and lattice Monte Carlo results give $\xi = 0.206(9)$. The agreement of three completely independent calculation strongly suggest that the energy for four-atom system is settled at present. This is further supported by the released-node calculation for the system, as will be shown in Fig. 4.6.

After the successful calculation of four-atom system, the DMC calculations are extended to larger systems of 14, 38 and 66 atoms. The numbers of atoms for the system are chosen so that the state corresponds to the closed shell. The calculated the ground state energies are listed in Tabel 4.1 and shown in Fig. 4.5. Energy drops are smaller per atom compare to four-atom system, the total energy drop is approximately 5 percent when compared to the results without extrapolation. This clearly indicates that in order to really reach the unitary limit, the effect of the effective range should be verified very carefully.

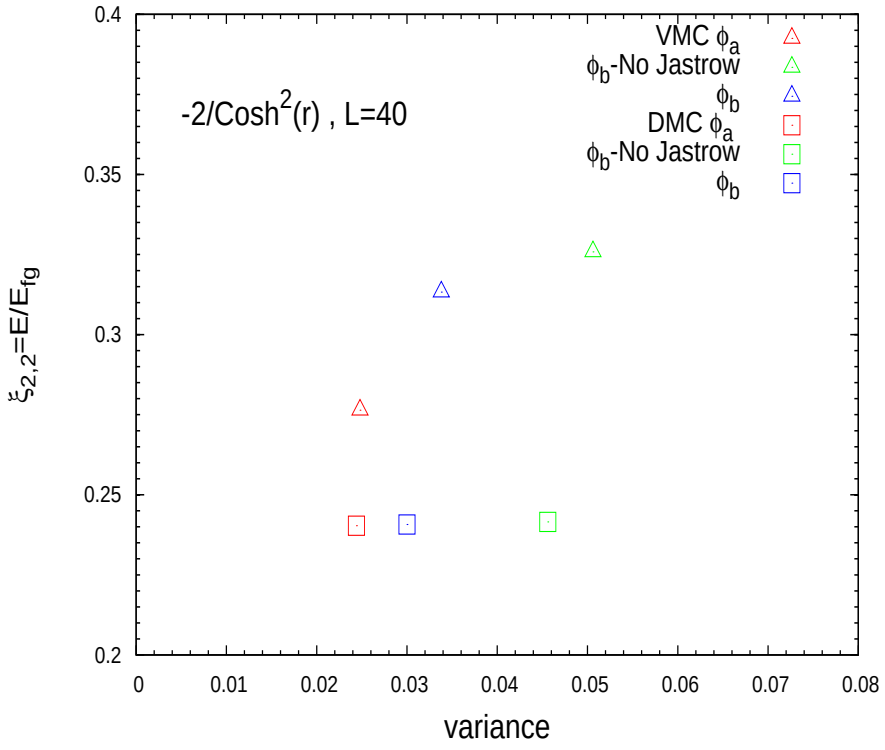


Figure 4.3: VMC and DMC calculation for the four-atom system using different pair orbitals and with or without Jastrow factor. The three wave functions yield almost identical DMC energy, indicating the accuracy of the calculation is very high. The statistical error bars are smaller than the symbol size.

Table 4.1: Effective range extrapolation of Bertsch parameter from DMC results for 4, 14, 38 and 66 atoms

| Atom number | 4 | | 14 | 38 | 66 |
|---|---|---|---|---|---|
| $\frac{R_{\text{eff}}}{r_s} = 0.12794$ | 0.238(1) | $\frac{R_{\text{eff}}}{r_s} = 0.1$ | 0.426(1) | 0.426(1) | 0.417(1) |
| 0.06397 | 0.224(1) | 0.05 | 0.416(1) | 0.417(1) | 0.411(1) |
| 0.03199 | 0.218(1) | 0.025 | 0.411(1) | 0.414(1) | 0.404(1) |
| 0.01599 | 0.215(1) | 0.0125 | 0.410(1) | 0.412(1) | 0.401(1) |
| 0.007996 | 0.213(1) | 0.00625 | 0.409(1) | 0.410(1) | 0.400(1) |
| 0.003998 | 0.212(1) | 0.003125 | 0.407(1) | 0.409(2) | 0.399(2) |
| 0(extropolated) | 0.212(2) | 0(extropolated) | 0.407(2) | 0.409(3) | 0.398(3) |

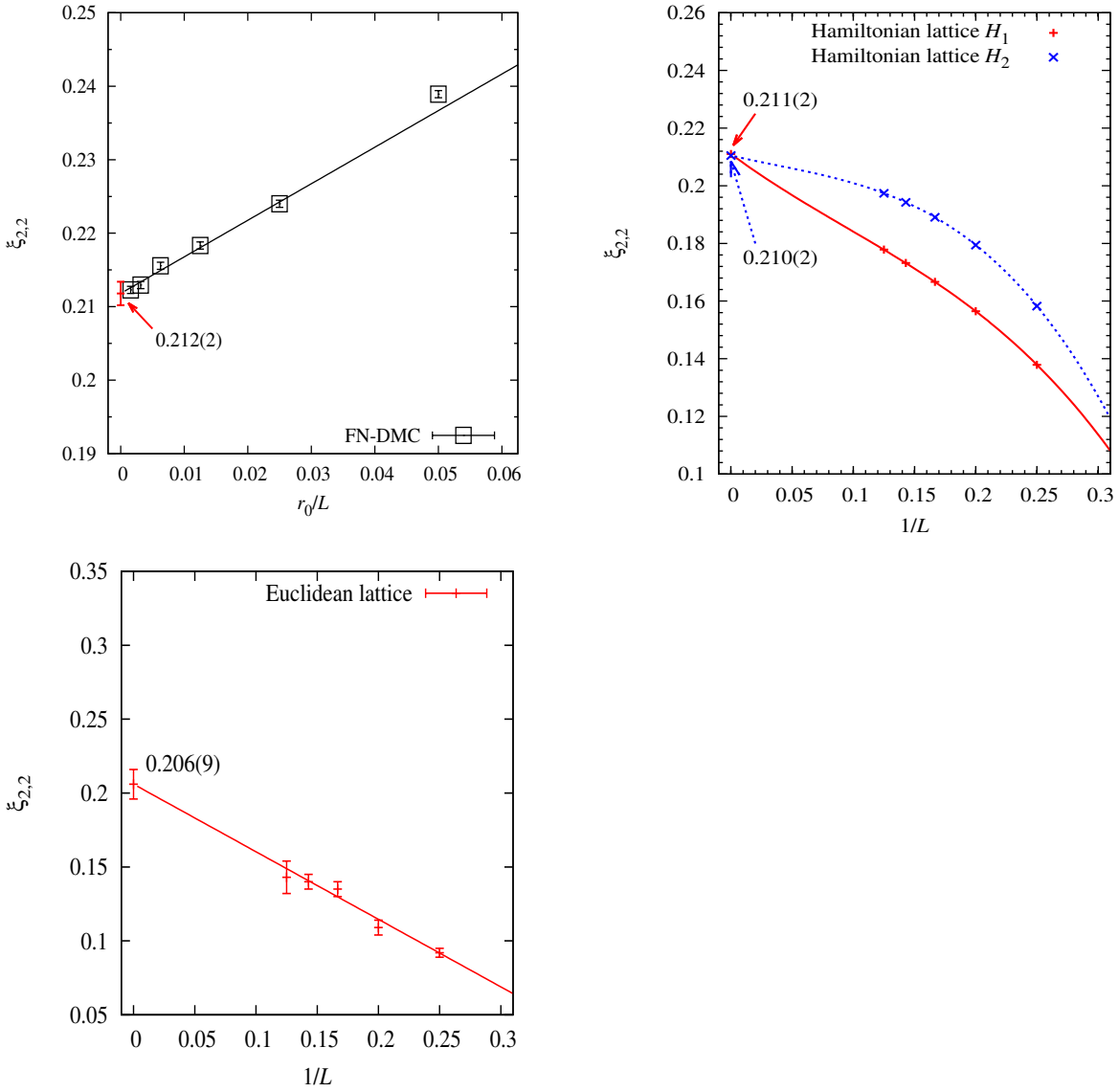


Figure 4.4: Three independent methods used for calculation $\xi_{2,2}$[17]. Upper left panel is the linear extrapolation of the effective range of the DMC results for the unpolarized four- atom system, by extrapolating the effective range of the potential to 0, the Bertsch parameter of four-atom system is found to be 0.212(2). Upper right panel is the results from direct diagonalization of Hamiltonian, which yields results of 0.211(2) and 0.210(2). Lower left panel is the results of the lattice Monte Carlo results, which gives result 0.206(9).

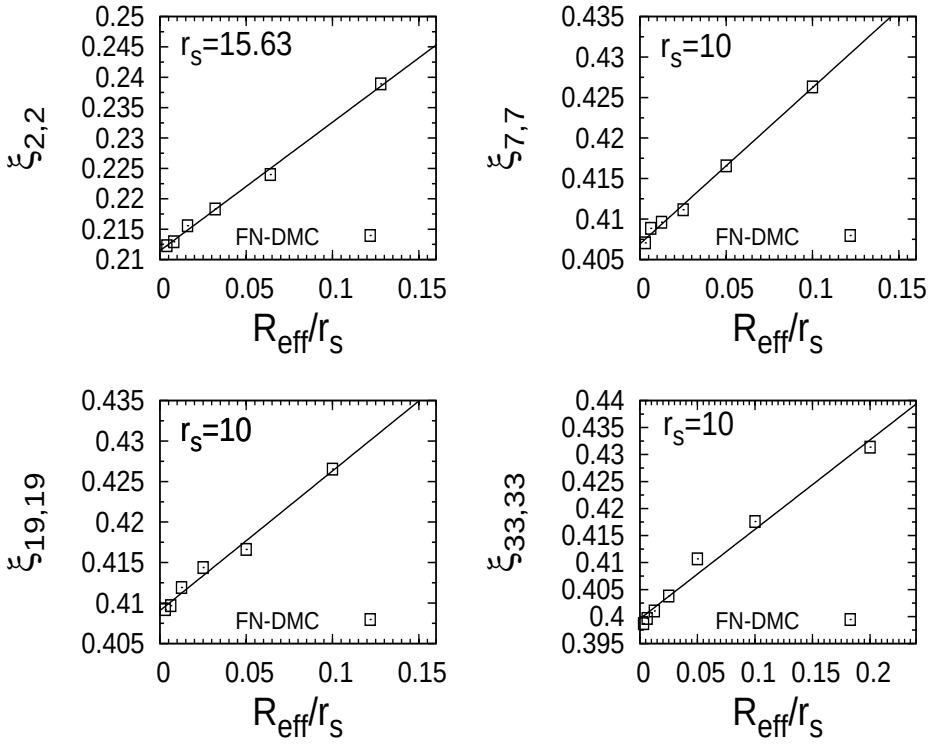


Figure 4.5: Linear extrapolation of the effective range of the DMC results for 4, 14, 38 and 66 atoms. By extrapolating the effective range of the potential to 0, $\xi_{2,2}, \xi_{7,7}, \xi_{19,19}, \xi_{33,33}$ are found to be 0.212(2), 0.407(2), 0.409(3), 0.398(3) respectively.

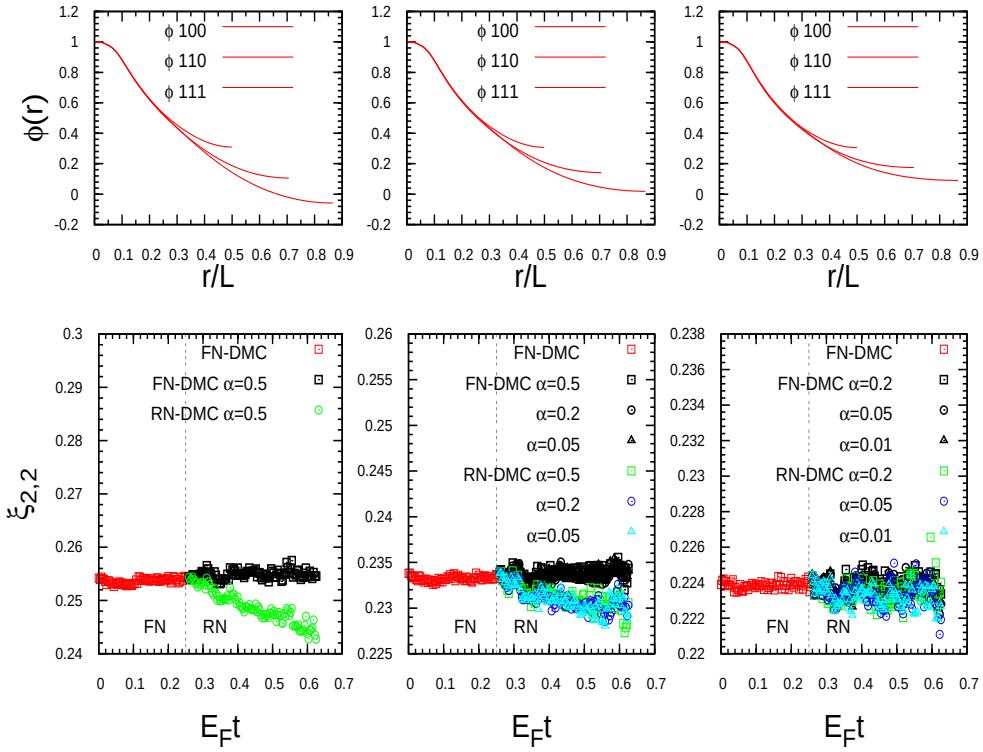


Figure 4.6: The pair orbitals and FN-DMC and RN-DMC energies of the 4-atom unitary system with $R_{\text{eff}}/r_s = 0.06397$. The upper row shows the pair orbitals with the lowest (left), intermediate (middle) and optimal (right) accuracy with regard to the variational optimization. The lower row shows the corresponding DMC energies as functions of the projection time starting from the variational estimate. Note that the resolution of the left and right panels differs by an order of magnitude. The vertical grey lines indicate the instant of the nodal release.

### 4.2.2 Released-node DMC results for 4 and 14 unpolarized atoms

In order to further corroborate the previous fixed-node DMC results of four-atom system and test the quality of the nodal surface, the released-node calculations are performed for 4 and 14 atoms. In a typical released-node run the number of walkers was about two million so that the error bars were initially very small. Time step $\Delta\tau$ was set to $4 \times 10^{-5} r_s^2$ in all cases and the time-step bias of the results were verified to be negligible.

The RN-DMC calculations for 4 atoms were done with $R_{\text{eff}}/r_s = 0.06397$. In Fig. 4.6, the upper row shows the pair orbital along three distinct directions (100, 110 and 111) of the interparticle distance vector $\mathbf{r}_i - \mathbf{r}_j$. The lower row shows the FN-DMC and RN-DMC energies

as they evolve with the projection time. The plots show convergence of the FN-DMC energy followed by the nodal release. This is accomplished by switching the guiding wave function from $\Psi_T(\mathbf{R})$ to the bosonic function $\Psi_G(\mathbf{R})$, as is introduced in Chapter 2.

The released-node signal reflects the quality of the nodal surface of the trial wave function employed in the FN-DMC simulation. In order to test for the effectiveness of the RN-DMC method we introduce the wave functions with intentionally varied accuracy by employing sub-optimal pair orbitals. The plot of the energy evolution in the left panel of Fig. 4.6 shows a clear and pronounced drop after the nodal release. As the quality of the pair orbital improves, this drop shrinks. For the fully optimized BCS-Jastrow wave function (the right panel in Fig. 4.6) the energy is reduced by less than 0.002 within the longest projection time that has been tried. Despite the fact that energies do not converge within the simulation time, it is apparent that the released-node method successfully detects the nodal inaccuracies that were intentionally introduced into the wave functions. In addition, as expected, the amplitude of the released-node signal qualitatively corresponds to the size of the introduced nodal deficiencies: the larger the nodal distortion the stronger the nodal release response. For the best wave function there is essentially no released-node signal visible within the obtained error bars and projection times. This fact further supports the fixed-node DMC results and indicates that the fully optimized BCS wave functions are very accurate in this small system and that the fixed-node error is marginal.

An unexpectedly high sensitivity of the nodal quality to the details of the pair orbital at large distances are also observed. Although the suboptimal orbitals used in the 4-atom RN-DMC simulations are modified only in their long-range tails (see the upper row of Fig. 4.6), the fixed-node energies raise by sizeable amounts. This suggests an explanation for the relatively slow convergence of the released-node energy: the long-range tails of the pair orbital affect the nodal hypersurfaces, although the energy cost of nodal hypersurfaces displacement is surprisingly low. One can further deduce that this makes the released-node method quite challenging to apply since it requires correcting the nodal surface change by sampling low-density regions with walkers travelling large distances. This is, however, difficult to achieve since the diffusive motion of walkers is slow, proportional to $t^{1/2}$, while the growth of the noise is fast, proportional to $\exp(\Delta_{BF}t)$, where $\Delta_{BF}$ is the difference between the bosonic and fermionic ground-state energies.

The RN-DMC energy for 14 atoms with $R_{\text{eff}}/r_s = 0.2$ is shown in Fig. 4.7. The error bars are estimated from eight independent runs with two million walkers each. In the interval of $E_F t \leq 0.2$ after the nodal release the RN-DMC energy gain appears to be very small and the error bars preclude to make any statistically sound estimation for longer projection times. The rapid loss of resolution is expected since the difference between the bosonic and fermionic ground states grows with the number of atoms. The RN-DMC signal exhibits little dependence

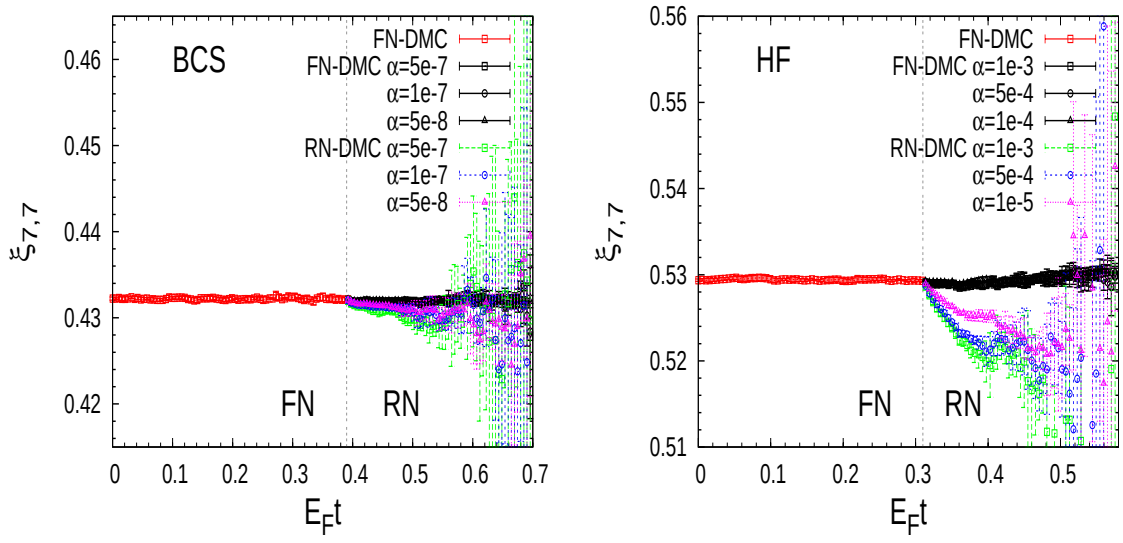


Figure 4.7: Evolution of the DMC energies for the 14-atom system with the best optimized BCS-Jastrow wave function(left) and Slater-Jastrow wave function(right). The runs are for $R_{\text{eff}}/r_s = 0.2$. For the BCS-Jastorw wave function, no statistically significant energy drop is observed after the nodal release that is indicated with the vertical dotted line. For the Slater-Jastrow function, the RN-DMC drops are significant, the parameter $\xi_{7,7}$ drops by $\approx 0.015$ within $E_F t \approx 0.2$ after the nodal release.

on the parameter $\alpha$ that appears in the guiding wave function.

In order to make a comparison with a case displaying a clear fixed-node bias, we have carried out RN-DMC runs using the Slater-Jastrow trial wave function, see right panel of Fig. 4.7. Since this wave function has the nodal surface of the non-interacting Fermi gas, the nodal surface is strongly distorted. As a result, we see a pronounced released-node signal. However, within the projection time interval of $E_F t \leq 0.2$, the energy drops by only $\approx 0.015$ for the largest $\alpha$ we tested. This is very small considering that the true ground-state energy is at least an order of magnitude lower, which illustrates the challenges of efficient application of the released-node method, at least for the present cases. Nevertheless, the released-node method clearly detects the existence of the nodal errors associated with the Slater wave function. Although a definite assessment can not be made of the fixed-node errors of the BCS wave functions, the comparison of Figs. 4.7 indicates that they are considerably smaller than the fixed-node errors of the Slater determinant.

To summarize, the released-node DMC calculations have been performed for 4 and 14 atoms with different types of wave functions with intentionally varied nodes. The release-node results for 4 atoms indicate that fully optimized BCS wave function is very accurate and the fixed-node error is marginal for this small system. For larger system of 14 atoms, the convergence to the correct and asymptotically exact ground-state energies are found to be unfavorably slow compared to the growth of the statistical noise. Only small energy gains within the simulation times that allowed for acceptable signal to noise ratio can be identified. Despite that, the RN-DMC calculations have shed new light on the remaining nodal errors which are related to the less accurate description of the low-probability regions of the configuration space.

### 4.2.3 Pair correlation function

Pair correlation functions may be regarded as the probability of finding one atom given the position of another atom with same or different spins.

As is shown is in Fig. 4.8, the same spin pair correlation function $g^{\uparrow\uparrow}(r)$ is 0 when the distance between two up spin atoms are 0, which is anticipated by the Pauli exclusion principle that no two atoms with same spin can occupy the same state. As the distance increases, the same spin pair correlation function increase gradually and when $k_F r > 5$, its value approaches 1, indicating there's essentially no correlation for the distance bigger than $k_F r > 5$. The different spin pair correlation function $g^{\uparrow\downarrow}(r)$ at $k_F r < 2$ shows a enhanced probability of finding one spin up atom near the spin down atom. At unitary limit, although two-body problem has no bound state, the spin up and spin down atom has already formed molecule due to the many-body effect. The value approaches 1 for $k_F r > 2$ suggesting the correlation distance between different spins are smaller than that of the same spin.

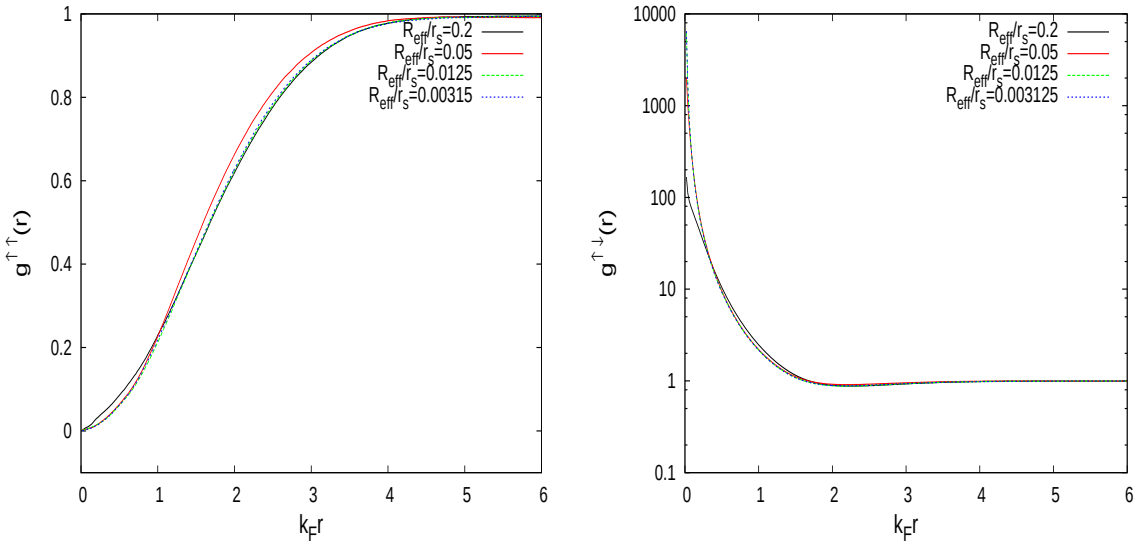


Figure 4.8: Pair correlation function for unpolarized 66 atom system with $R_{\text{eff}}/r_s = 10$, the left panel is the same spin pair correlation function $g^{\uparrow\uparrow}(r)$ and the right panel is the opposite spin pair correlation function $g^{\uparrow\downarrow}(r)$. The results indicate effective range extropolation has little effect on $g^{\uparrow\uparrow}(r)$, and there's enhancement at short distance $r \approx 0$ for $g^{\uparrow\downarrow}(r)$ with smaller effective interaction range.

The effective range extropolation has different effect for spin pair correlation function $g^{\uparrow\uparrow}(r)$ and $g^{\uparrow\downarrow}(r)$. The $g^{\uparrow\uparrow}(r)$ is almost not affected by the effective range extrapolation. As is shown in Fig. 4.8, with different effective interaction range of the interaction potential, the pair correlation function between up up atoms almost overlaps. This can be explained by the fact that when extrapolate the effective range of the interaction, the short range behavior does not change too much as the probability of the same spin atom being very close is small. For $g^{\uparrow\downarrow}(r)$, the peak near $r = 0$ is increased for smaller effective potential, indicating the probability of finding atoms with different spins near short distance enhances when the effective range of interaction potential becomes smaller.

The pair correlation function provides useful information regarding the probability of finding one atom given the position of another atom, which is useful for direct experimental observation. Also, the pair correlation function bares useful many-body information of the system, the pair correlation functions are used to extract Tan's constant, as will be introduced in the later section.

### 4.2.4 One-body, two-body density matrices and condensate fraction

The calculation of off-diagonal OBDM is shown in Fig. 4.9, as can be seen from the graph, the effective range extrapolation has relatively little effect on the OBDM except some minor shift in the region $k_F r < 2$, this correspond in the momentum space a smaller fraction of interacting atoms below Fermi energy.

In order to quantify the pairing effects the two-body density matrix are calculated as in Fig. 4.10 and this enables the evaluation of the condensate fraction. The projected TBDM for spin-up and spin-down atoms is defined as

$$\rho^{(2)}(\mathbf{r}) = \frac{N^2}{4V^2} \frac{\int d\mathbf{R}\Phi(\mathbf{R})\Psi_T(\mathbf{R})\frac{\Psi_T(\mathbf{r}_1+\mathbf{r},\mathbf{r}_2+\mathbf{r})}{\Psi_T(\mathbf{r}_1,\mathbf{r}_2)}}{\int d\mathbf{R}\Phi(\mathbf{R})\Psi_T(\mathbf{R})}\,, \tag{4.6}$$

where $N$ is the total number of atoms and $V$ is the volume of the simulation cell. The density matrices have been calculated for the fixed-node wave functions and hence they correspond to the mixed estimators [44]. Nevertheless, the mixed-estimator bias is negligible since the variational Monte Carlo and DMC estimates of $\rho^{(2)}$ coincide within error bars. This is a further evidence of the high accuracy of our trial wave functions.

The condensate fraction can be extracted from the two-body density matrix as

$$c = \frac{2V^2}{N} \lim_{r\to\infty} \rho^{(2)}(r)\,. \tag{4.7}$$

The calculated density matrices are shown in Fig. 4.10 with the condensate fraction estimated

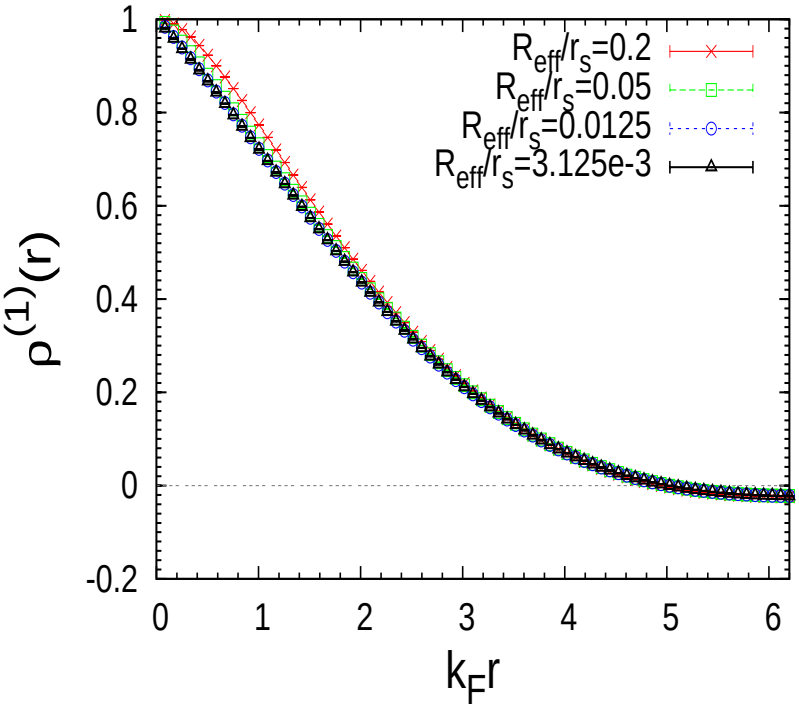


Figure 4.9: The one-body density matrix for 66 atoms calculated from the FN-DMC mixed estimator, the one-body density matrix change relatively small with respect to the effective range extrapolation.

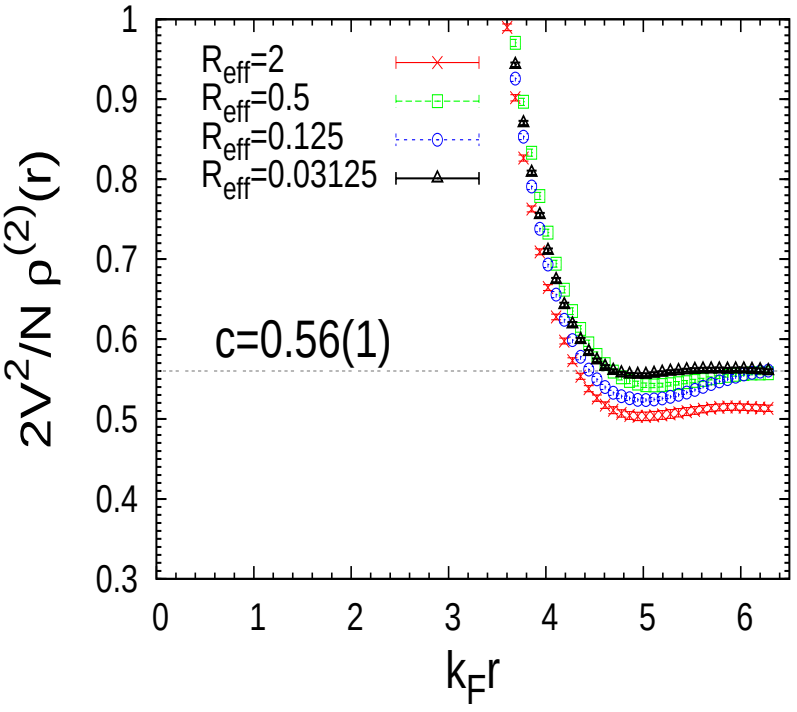


Figure 4.10: The two-body density matrix for 66 atoms calculated from the FN-DMC mixed estimator. The condensate fraction converges to 0.56(1) for $R_{\rm eff}/r_s \leq 0.05$ for the effective range extrapolation.

from the long-range limit. The condensate fraction saturates for $R_{\text{eff}} \leq 0.5$ at $c = 0.56(1)$. This value is not too far from the results obtained previously [4, 64].

### 4.2.5 Nodal surface of BCS, unitary limit and BEC results

To illustrate the character of the nodal surfaces in the BCS-BEC systems, the three-dimensional scans of the nodes are presented for three wave functions corresponding to the following scattering regimes: the free atomic gas with no pairing, the best unitary-limit wave function, and the wave function with enhanced pairing from the BEC side of the BEC-BCS phase diagram ($a_s k_F = 0.6592$). The left column of Fig. 4.11 displays the nodal surface of the free atomic Fermi gas. The de-localized nature of the system is apparent. At the unitary limit, shown in the middle column of Fig. 4.11, the shape of the nodal surface is significantly different as the pairing effects clearly dominate and lead to a localized character of the nodes from the perspective of a pair of up and down spin atoms. The nodes on the BEC side (the right column) do not differ much from the unitary limit, except for a slightly more pronounced localization.

## 4.3 Extraction of Tan's constant

Tan derived a simple formula relating the energy of s-wave scattering length to the energy [72, 74, 73], with the form

$$E = \frac{VC}{4\pi a_s m} + \sum_{\mathbf{k}\sigma} \frac{k^2}{2m}(n_{\mathbf{k}\sigma} - \frac{C}{k^4}). \tag{4.8}$$

Eq. 4.8 is the so called Tan's formula, in which $V$ is the volume, $a_s$ is the s-wave scattering length between up and down atoms, with the the parameter $C$ defined as

$$C \equiv \lim_{\mathbf{k}\to\infty} k^4 n_{\mathbf{k}\uparrow}. \tag{4.9}$$

C is called contact parameter, which links the equation of state, pair correlation function, momentum distribution and one-body density matrix together. C gives an measurement for the formation of pairs. The contact parameter C is to some finite value in the unitary limit, and it can be extracted from the one-body density matrix and same spin pair correlation function. Following Gandolfi et.[43], the contact parameter can be parametrized through $\zeta$ and $\mu$ as

$$\frac{C}{k_F^4} = \frac{2}{5\pi}\left[\zeta + \frac{10\nu}{3(k_F a_s)} + \cdots\right], \tag{4.10}$$

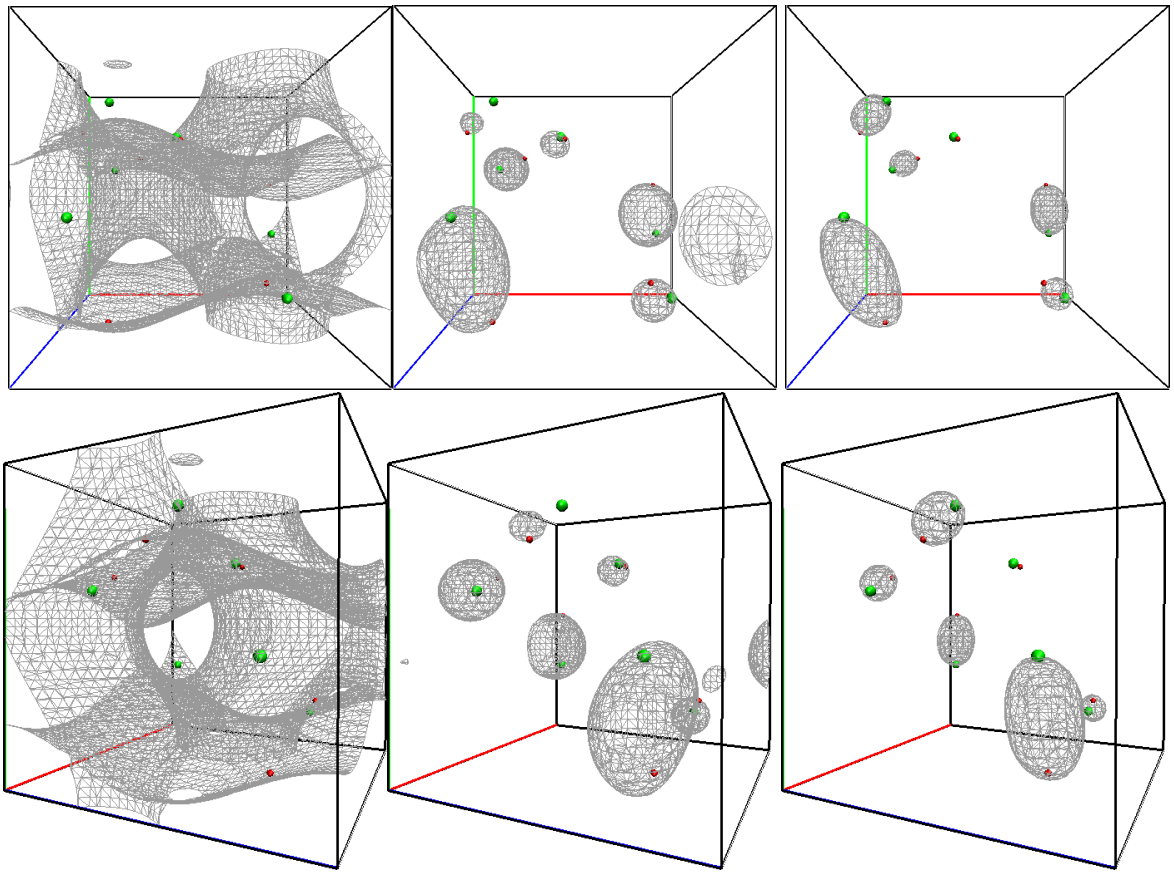

Figure 4.11: Three-dimensional subsets of the nodal hypersurfaces for three types of wave functions and corresponding phases in the 14-atom system. The node is obtained by scanning the simulation cell with a pair of spin-up and spin-down atoms sitting on the top of each other while keeping the rest of the atoms at fixed positions (tiny spheres). From the left to the right, the columns show the nodal surfaces of the wave functions corresponding to the free Fermi gas, the unitary limit and the BEC side of the crossover. The lower row displays the same surfaces rotated by 45 degrees around the $z$-axis.

where $\zeta$ and $\nu$ may be linked with equation of state, one-body density matrix pair$\rho_1(r)$, pair correlation function $g_{\uparrow\downarrow}(r)$ and momentum distribution function $n(\mathbf{k})$ at the unitary limit as

$$\frac{E}{E_{\text{Free}}} = \xi - \frac{\zeta}{k_F a_s} - \frac{5\nu}{3(k_F a_s)^2} + \cdots , \tag{4.11}$$

$$\rho_1(r) = 1 - \frac{3}{10}\nu k_F r + \cdots , \tag{4.12}$$

$$g_{\uparrow\downarrow}(r) = \frac{9\pi}{20}\nu\frac{1}{(k_F r)^2} + \cdots , \tag{4.13}$$

$$n(k) = \frac{8}{10\pi}\nu\frac{k_F^4}{k^4}. \tag{4.14}$$

Where $\xi$ is the Bertsch's parameter, $k_F$ is the Fermi vector.

Fitting the above equation from results of pair correlation function gives

$$\nu_1 = 0.860(1) \tag{4.15}$$

and fitting the above equation from for the one-body density matrix gives

$$\nu_2 = 0.903(1) \tag{4.16}$$

These two values, which should be equal by definition, agrees reasonably well from the data fitting by DMC calculations, the resulting contact parameter is thus(calculated from the average of the two $\nu$ above, errorbars is estimated to include the value of C calculated from each single $\nu$)

$$\frac{C}{k_F^4} = \frac{2\nu}{5\pi} = 0.112(4) \tag{4.17}$$

Recent experimental results[53] from static structure factor determine the value of $\nu = 0.93(5)$, while the slope $S(k)$ versus $k_F/k$ at $T = 0.10(2)T_F$ yields a value of 0.80(3), which is comparable with our results.

## 4.4 Conclusion

In this Chapter, we have provided a comprehensive study of various quantities of interest for the unpolarized Fermi gas. The main questions that have been raised as the motivation of this study has been answered. First, the effective range of the potential for the interacting atoms does affect the ground state energy. If the effective range is extrapolated to 0, as the true unitary limit is defined, the energies will drop around 5 to 10 percent, depending on the interparticle spacing or the number of particles in the periodic box. Second, the released-node method provides a method to determine the fixed-node error and the accuracy of the nodal

surface. The RN-DMC in the study provides clear signal at unitary limit if inappropriate wave function has been used, and for a small number of of four atoms, the released-node result suggest that the pair orbital and nodal surface of the BCS wave function is very accurate. For larger number of 14 atoms, RN-DMC already encounters efficiency problem. Nevertheless, the RN-DMC calculation in this work shed lights on the origin of the fixed-node error and we are able to identify the wrong node immediately when inaccurate wave function or pair orbital are used. Besides ground state energy, the pair correlation function, one-body density matrix, condensate fraction and Tan's constant are also calculated.

The room for further improvement of the nodal surface on the other hand is not completely exhausted(As can be also seen in [43], and some recent auxillary field Monte Carlo [23]), due to the particular nature of the problem for the homogeneous Fermi gas in a periodic box, the long tail of the pair orbital needs to be tuned very accurately in order to get accurate nodal surface and ground state energy, which is alleviated if the Fermi gas is in a trapped configuration, as will be shown in the next Chapter.

# Chapter 5

# Unpolarized Fermi gas in isotropic and anisotropic harmonic traps

The unpolarized Fermi gas in harmonic traps have been studied extensively experimentally in the past ten years due to the well established cooling techniques and Feshbach resonance. The trapped system is more closely connected to the cold atom experiment unlike the periodic gas system. It will be interesting to perform computational simulation for the trapped system to obtain various properties and make direct comparisons with the experimental results.

The unpolarized Fermi gas in isotropic harmonic trap has been studied previously by various numerical methods such as correlated Gaussian method[77], diffusion Monte Carlo method[30, 77] and lattice auxiliary field Monte Carlo method [38], the calculated results however show discrepancies between different methods. Since the system of few atom is of fundamental interest, it will be interesting to find out the exact ground state energy and understand the discrepancies in the literature. Also, the local density approximation(LDA) provides a density profile for the trapped Fermi gas system, and it is well-known that the LDA will fail for the area with large density variation(for example, on the edge for the trapped Fermi gas system). It will be illuminating to see the exact density profile and find out the correction for LDA at edge of the potential.

Furthermore, by increasing the harmonic trapping frequency $\omega_z$ while keeping the trapping frequency in x and y direction unchanged, the motion of Fermi atoms in z direction is gradually frozen. The simulation setup then can be regarded as an explicite transition from isotropic three dimensional harmonic trap to two dimensional harmonic trap. The Fermi gas with reduced dimensions has different properties than that of the three dimensional counterpart. Most importantly, in totally freezed motion of z direction of two dimensional system, the fermions form bound state with arbitrary weak attractive interaction, and the binding energy is predicted to be identical to the two-body binding energy by the mean field theory. It is also interesting

to test the existing theory with the accurate DMC method.

All of these provide the motivations for the calculations in this Chapter for unpolarized Fermi gas in isotropic and anisotropic harmonic traps with gradually increased frequency in z direction.

## 5.1 Simulation setup

The simulation for the unpolarized Fermi gas is carried out in harmonic traps, the Hamiltonian is written as

$$\hat{H} = -\frac{1}{2}\sum_{i=1}^{N/2}\nabla_i^2 - \frac{1}{2}\sum_{i'=1}^{N/2}\nabla_{i'}^2 + \sum_{i,i'}V(r_{ii'}) + \sum_{i,i'}V_{\text{ext}}(\mathbf{r}_i) + V_{\text{ext}}(\mathbf{r}_{i'}), \tag{5.1}$$

in which

$$V(r_{ii'}) = -\frac{2\mu^2}{\cosh^2(\mu r_{ii'})}, \tag{5.2}$$

is the Pöschl-Teller potential for the interaction between spin-up and spin-down atoms with indices $i$ and $i'$, $r_{ii'}$ denotes $|\mathbf{r}_i - \mathbf{r}_{i'}|$, and

$$V_{\text{ext}}(\mathbf{r}) = \frac{1}{2}\left[\omega_\perp(x_i^2 + y_i^2) + \omega_z z_i^2\right], \tag{5.3}$$

is the external harmonic potential for the atoms, where $\omega_\perp = \omega_x = \omega_y$.

The trial wave function of the system is chosen to be

$$\Psi_{T1}(\mathbf{R}) = \Psi_{\text{BCS}}(\mathbf{R})e^{J(\mathbf{R})}\prod_i g(\mathbf{r}_i)\prod_{i'} g(\mathbf{r}_{\mathbf{i}'}), \tag{5.4}$$

where $\Psi_{\text{BCS}}$ is the BCS wave function and $e^{J(\mathbf{R})}$ is the Jastrow factor and the forms of these two terms are similar to the ones in the homogeneous Fermi gas system. An additional one-body term $g(\mathbf{r})$ multiplier is used to fix the boundary of the Fermi gas system at the edge of the trap. $g(\mathbf{r})$ is assumed to be the same for the spin-up and spin-down atoms due to symmetry, and takes the form

$$g(\mathbf{r}) = \sum_k d_k e^{-\alpha_k(x^2+y^2)-\beta_k(z^2)}, \tag{5.5}$$

where $d_k$ are the variational coefficients, which are found by optimization of the wave function. $\alpha_k$ and $\beta_k$ are the Gaussian coefficients which ensure the wave function vanishes outside the length scales of characteristic lengths $\sqrt{\frac{1}{\omega_\perp}}$ and $\sqrt{\frac{1}{\omega_z}}$. The accurate optimization of $d_k$ is crucial to fix the boundary of the Fermi gas in the trap, and reduce the fixed-node error.

## 5.2 QMC results

### 5.2.1 Four-atom system results

In order to test the validity of the simulation, the simplest case of simulation of four-atom system in isotropic harmonic trap is calculated. Besides the trial wave function Eq. 5.4, another form of trial wave function is used, which has the form

$$\Psi_{T2}(\mathbf{R}) = \Psi_{\text{Slat}}(\mathbf{R}) e^{J(\mathbf{R})}, \tag{5.6}$$

where

$$\Psi_{\text{Slat}} = \sum_{k=2}^{4} \det \begin{bmatrix} \varphi_1(\mathbf{r}_1)\varphi_1(\mathbf{r}_3) + \varphi_k(\mathbf{r}_1)\varphi_k(\mathbf{r}_3) & \varphi_1(\mathbf{r}_1)\varphi_1(\mathbf{r}_4) + \varphi_k(\mathbf{r}_1)\varphi_k(\mathbf{r}_4) \\ \varphi_1(\mathbf{r}_2)\varphi_1(\mathbf{r}_3) + \varphi_k(\mathbf{r}_2)\varphi_k(\mathbf{r}_3) & \varphi_1(\mathbf{r}_2)\varphi_1(\mathbf{r}_4) + \varphi_k(\mathbf{r}_2)\varphi_k(\mathbf{r}_4) \end{bmatrix}. \tag{5.7}$$

Here $\varphi_1$ is the one-body ground state for the harmonic trap and $\varphi_2, \varphi_3, \varphi_4$ are the first excited states in x, y and z direction with degenerate energy. Since in the harmonic trap, the most important levels for small number of four atom are the ground state and the first excited states, the wave function Eq. 5.6 captures the most important physics and the remaining correlation is further included in the Jastrow factor $e^{J(\mathbf{R})}$.

The results for the four atoms in the harmonic trap are shown in Fig. 5.1. The effective range of the interaction is extropolated to 0, and the energy drops around 3 percent. The trial wave function in Eq. 5.4 is found to provide slightly better results. The final extrapolated result is $5.032(3)\omega_z$, which is comparable to correlated Gaussian method $5.028\omega_z$ and slightly better than the previous DMC result 5.051(9)[77]. Also, the auxiliary field lattice calculation gives 5.071(75)[38]. As can be seen, the results for various methods agree within 1 percent, validating the current DMC calculation.

### 5.2.2 Energy

The energy for the unpolarized Fermi gas in both isotropic and anisotropic harmonic traps is calculated similarly as for the four-atom system, since wave function in Eq. 5.4 provides better results it is used exclusively for system with larger number of atoms.

The calculated DMC results for the isotropic trap are listed in Table 5.1. The linear extrapolated DMC results and previous DMC results, correlated gaussian method results[77] and lattice[38] calculation results are shown in Table 5.2. The calculated DMC results for anisotropic traps are listed in Table 5.3, 5.4 and 5.5.

The energy in the unit of $\omega_z$ for the isotropic harmonic trap is shown in Fig. 5.2

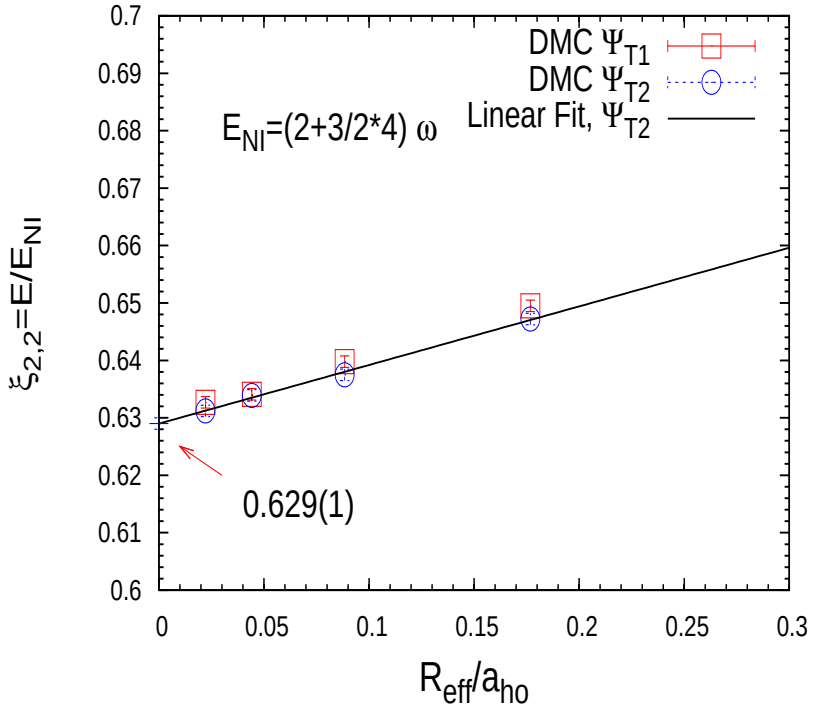


Figure 5.1: DMC energy of unpolarized four-atom system in harmonic trap with two different trial wave function with effective range of the interaction extrapolated to zero. The extrapolated Bertsch's parameter reads 0.629(1).

Table 5.1: DMC energies of unpolarized Fermi gas in isotropic harmonic traps with atom number N and varing effective range. Energies are in unit of $\omega_z$.

| N | $\frac{R_{\rm eff}}{a_{ho}} = 0.1768$ | =0.08839 | =0.04419 | =0.02209 |
|---|---|---|---|---|
| 2 | 2.0368(1) | 2.0184(1) | 2.0056(1) | 2.0040(1) |
| 4 | 5.178(1) | 5.100(1) | 5.071(1) | 5.050(1) |
| 6 | 8.632(2) | 8.507(2) | 8.442(3) | 8.427(5) |
| 8 | 12.568(3) | 12.410(5) | 12.316(6) | 12.306(6) |
| 10 | 16.924(3) | 16.666(3) | 16.462(3) | 16.419(6) |
| 12 | 21.281(2) | 20.956(3) | 20.792(3) | 20.720(8) |
| 16 | 30.944(8) | 30.556(8) | 30.133(8) | 29.916(10) |
| 20 | 41.365(3) | 40.712(4) | 40.130(5) | 40.096(8) |
| 24 | 52.388(4) | 51.414(3) | 50.767(4) | 50.446(5) |
| 36 | 88.936(5) | 87.329(5) | 86.270(8) | 85.714(16) |
| 40 | 101.718(8) | 99.099(22) | 98.256(24) | 98.240(20) |

Table 5.2: Energies of unpolarized Fermi gas in isotropic harmonic traps with atom number N and effectivive range extrapolated energy results $E_{\rm ext}$, previous DMC and Lattice results(quoting the absolute value of the errorbars) and correlated Gaussian(CG) results. Energies are in unit of $\omega_z$.

| N | $E_{\rm ext}$ | DMC[77] | Lattice[38] | CG[77] |
|---|---|---|---|---|
| 2 | 2.000(2) | | | |
| 4 | 5.032(3) | 5.051(9) | 5.071(75) | 5.028 |
| 6 | 8.389(7) | 8.64(3) | 8.347(80) | 8.48 |
| 8 | 12.251(13) | 12.58(3) | 11.640(124) | |
| 10 | 16.34(3) | 17.8(1) | 16.050(69) | |
| 12 | 20.64(2) | 23.1(1) | 20.765(97) | |
| 16 | 29.85(8) | 33.2(1) | 29.932(93) | |
| 20 | 39.86(9) | 43.2(1) | 39.31(9) | |
| 24 | 50.446(5) | 50.22(8) | 51.44(20) | |
| 36 | 85.714(16) | 85.54(12) | 88.05(46) | |
| 40 | 97.37(33) | 109.7(1) | 100.50(30) | |

Table 5.3: Energies of unpolarized Fermi gas in anisotropic harmonic trap with atom number N and effective range extropolated energy $E_{\rm ext}$ with frequency ratio $\omega_\perp/\omega_z = 1/\sqrt{30}$. Energies are in the unit of $\omega_z$.

| N | $\frac{R_{\rm eff}}{a_{ho}} = 0.5$ | =0.25 | =0.125 | = 0.0625 | $E_{\rm ext}$ |
|---|---|---|---|---|---|
| 2 | 0.9965(3) | 0.9764(3) | 0.9656(3) | 0.9624(2) | 0.956(2) |
| 4 | 2.198(1) | 2.143(1) | 2.121(2) | 2.121(3) | 2.102(6) |
| 6 | 3.471(3) | 3.408(1) | 3.380(1) | 3.364(2) | 3.348(2) |
| 8 | 4.872(1) | 4.785(1) | 4.736(1) | 4.694(1) | 4.680(9) |
| 10 | 6.349(1) | 6.228(1) | 6.232(1) | 6.192(1) | 6.171(20) |

Table 5.4: Energies of unpolarized Fermi gas in anisotropic harmonic trap with atom number N and effective range extropolated energy $E_{\rm ext}$ with frequency ratio $\omega_\perp/\omega_z = 1/30$. Energies are in the unit of $\omega_z$.

| N | $\frac{R_{\rm eff}}{a_{ho}} = 0.5$ | =0.25 | =0.125 | = 0.0625 | $E_{\rm ext}$ |
|---|---|---|---|---|---|
| 2 | 0.8333(2) | 0.8102(2) | 0.8081(5) | 0.7978(7) | 0.794(3) |
| 4 | 1.725(7) | 1.673(1) | 1.628(1) | 1.620(1) | 1.629(2) |
| 6 | 2.543(1) | 2.487(1) | 2.459(1) | 2.447(1) | 2.431(2) |
| 8 | 3.427(1) | 3.350(1) | 3.314(1) | 3.299(1) | 3.278(2) |
| 10 | 4.324(1) | 4.227(1) | 4.181(1) | 4.162(1) | 4.136(3) |

Table 5.5: Energies of unpolarized Fermi gas in anisotropic harmonic trap with atom number N and effective range extropolated energy $E_{\rm ext}$ with frequency ratio $\omega_\perp/\omega_z = 1/25$. Energy are in the unit of $\omega_z$.

| N | $\frac{R_{\rm eff}}{a_{ho}} = 0.5$ | =0.25 | =0.125 | = 0.0625 | $E_{\rm ext}$ |
|---|---|---|---|---|---|
| 2 | 0.8334(1) | 0.8144(1) | 0.8057(3) | 0.8010(1) | 0.796(1) |
| 4 | 1.696(1) | 1.662(1) | 1.645(1) | 1.638(1) | 1.629(2) |
| 6 | 2.580(1) | 2.525(1) | 2.500(1) | 2.498(1) | 2.480(5) |
| 8 | 3.485(1) | 3.407(1) | 3.371(1) | 3.354(1) | 3.333(2) |
| 10 | 4.406(1) | 4.307(1) | 4.260(1) | 4.241(1) | 4.214(3) |
| 12 | 5.342(1) | 5.221(1) | 5.164(1) | 5.162(1) | 5.121(12) |
| 16 | 7.255(1) | 7.093(1) | 7.013(1) | 6.999(1) | 6.948(11) |
| 20 | 9.217(1) | 9.012(1) | 8.916(1) | 8.862(1) | 8.812(3) |
| 24 | 11.230(1) | 10.982(1) | 10.846(1) | 10.800(1) | 10.731(6) |
| 36 | 17.476(2) | 17.110(1) | 16.890(1) | 16.873(1) | 16.749(31) |
| 40 | 19.670(1) | 19.202(1) | 18.983(2) | 18.879(2) | 18.758(8) |

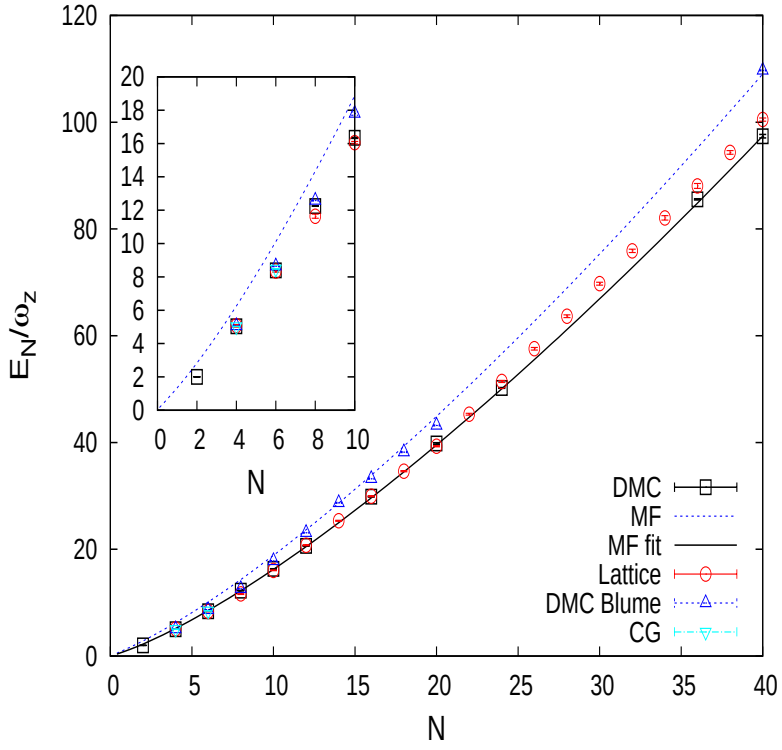


Figure 5.2: Energy v.s. number of atoms for the unpolarized Fermi gas in isotropic harmonic trap. The data is listed in Table 5.2. The DMC calculation results shows clear improvement over previous ones due to better choice of wave function.

For the isotropic harmonic case, the density functional using $\epsilon$ expansion[71] gives

$$E_N = E_{\mathrm{LDA}}(1 + c_s(3N)^{-2/3}), \tag{5.8}$$

where the $E_{\mathrm{LDA}}$ is the energy under local density approximation, which reads

$$E_{\mathrm{LDA}} = \frac{\sqrt{\xi}}{4}\omega(3N)^{4/3}, \tag{5.9}$$

with $c_s$ and $\xi$ parameters. For the non-interacting case, $\xi = 1$ and $c_s = 0.5$, and for the gas at unitary limit, previous calculation yields $\xi = 0.475$ and $c_s = 1.68$, shown as the dashed $MF$ curve in Fig. 5.2. Using the results in this work and a non-linear fit with the similar functional, the parameters are found to be: $\xi_{\mathrm{tr}} = 0.403(1)$, $c_s = 0.986(1)$, shown as the solid 'MF fit' curve in Fig. 5.2. The fitted $\xi$ is closer to the ones obtained for the Fermi gas system in the box with period boundary conditions. As DMC provides an upperbound for the ground state energy, the new parameters are considerably improved over previous calculation.

The extrapolated energy plot for both isotropic and anisotropic Fermi gas system, divided by the non-interacting system energy $E_{\mathrm{NI}}$ is shown in Fig. 5.3. With small number of atoms and isotropic harmonic potential, the system exhibits large shell effect. As the number of atoms is increased, the Bertsch parameter $E/E_{\mathrm{NI}}$ in isotropic harmonic trap seems to converge to 0.65(1). For the squeezed potential with $\omega_z/\omega_\perp = 1/25$, this parameter converges to 0.70(1). From the Fig. 5.3, it is also clear that as the frequency in z direction increases, the shell effect is more quenched.

The calculated energies provide a benchmark for the cold atom experiments, where the trap depth and frequency is tunable. In real experiments, anharmonic effects could also appear. In order to correct these effects, further investigation of the calculation is required.

### 5.2.3 Density profile

The density profile provides information of spatial distribution of the Fermi gas in the trap, as it is directly accessible by the cold atom experiments. It is interesting to make comparisons with theoretical prediction, numerical simulation and experimental data. The density profile for Fermi gas in isotropic harmonic trap for 40 atoms is shown in Fig. 5.4. where $r$ is the radial distance from the center of the trap, and $n(r)$ is the density profile. The bump at 0 radius is artificial due to the large sampling error. As shown in the Fig. 5.4, the Fermi gas shrinks in size as the attractive interaction is turned on. Also, the density curve is smoother for the gas at unitary limit, as the attractive interaction smoothes out one-particle orbitals. Furthermore, the density profile provided by the local density approximation predicts much larger atom density near the edge of the trap, as is discussed above. The correct treatment of the wave function

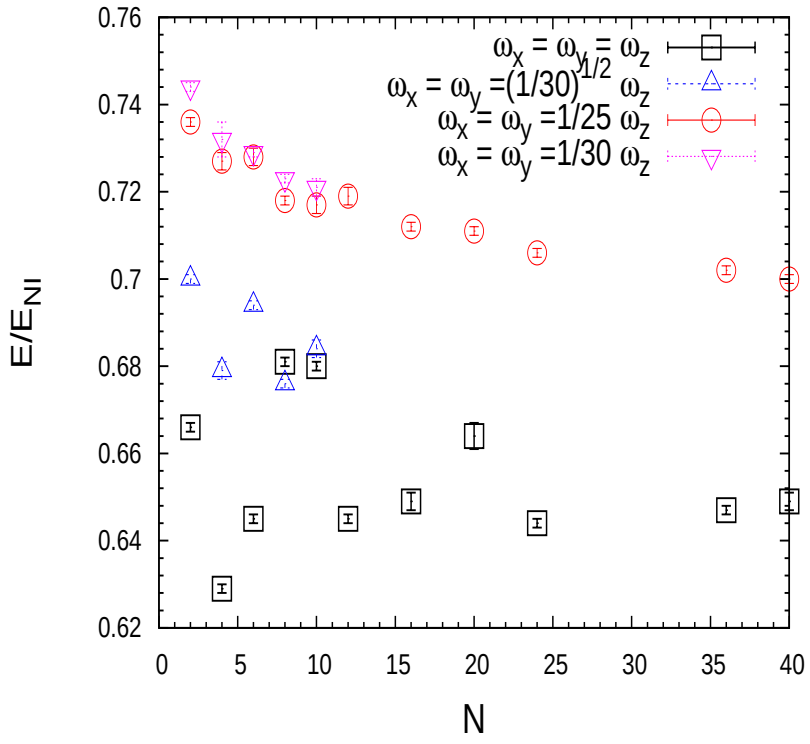


Figure 5.3: Bertsch parameter $E/E_{\rm NI}$ for unpolarized Fermi gas at unitary limit in isotropic and anisotropic harmonic trap.

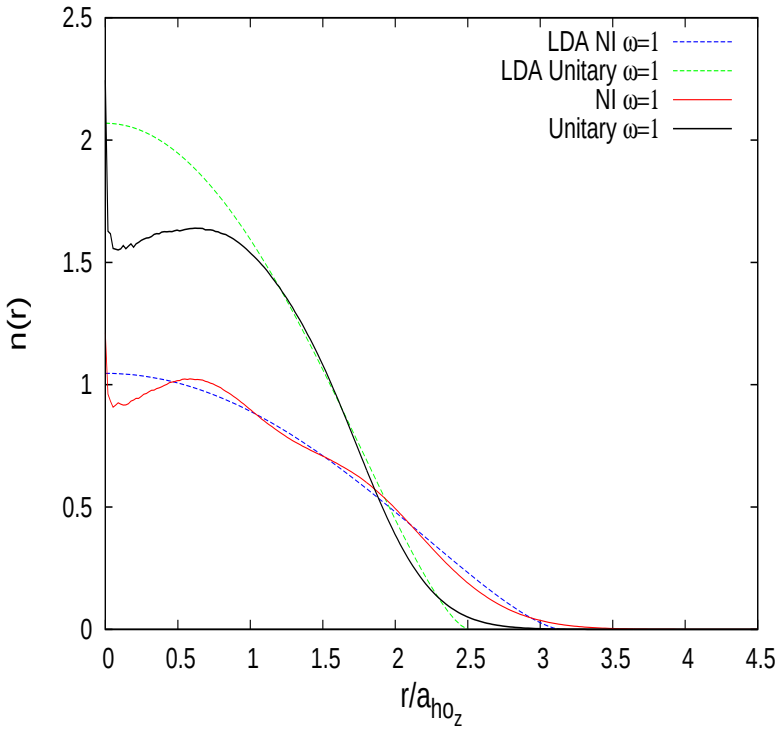


Figure 5.4: Density profile for unpolarized Fermi gas in isotropic harmonic trap. 'NI' stands for the non-interacting density profile, 'Unitary' for the density profile at unitary limit. The solid line is from QMC simulation and the dashed line is from the LDA.

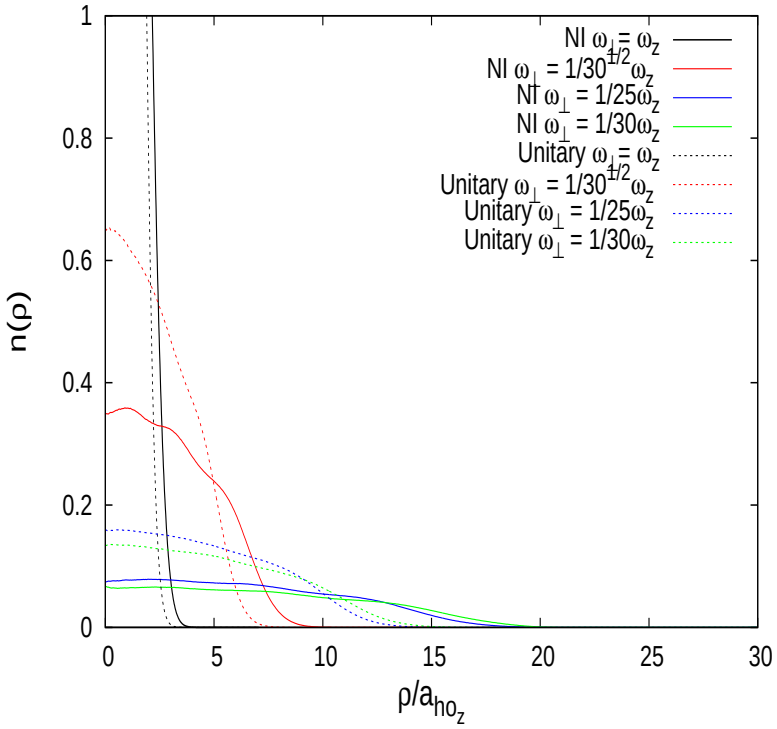


Figure 5.5: Projected density profile for unpolarized Fermi gas in isotropic and anisotropic harmonic traps. 'NI' stands for non-interacting density profile, shown as the solid line. 'Unitary' stands for the unitary limit density profile, shown as the dashed line. The densities are projected onto the x-y plane.

and hence density at the edge of the trap is essential to extract correct ground state energy and the local density approximation does not provide a good description for the interacting system, at least for the small sizes of fourty atoms or so.

The projected density profiles on the x-y plane for isotropic and anisotropic harmonic traps are shown in Fig. 5.5, where $\rho = \sqrt{x^2 + y^2}$ is the distance to the center of the trap on the x-y plane, Four different frequency ratios $\nu = \omega_z/\omega_\perp$ are used, as $\nu$ decreases from 1 to 1/30, the density profile extends further in the x-y plane, due to weaker constrains on the x-y plane with smaller trapping frequency. Again at the boundary of the trap, the densities for all the trap configurations are found to be modified significantly from the non-interacting cases and also, the local kinks for the non-interacting gas are smoothed out due to the attractive interaction.

### 5.2.4 Nodal surface

The accurate description of the nodal surface of the Fermi gas is the key for the DMC calculation. The nodal surface of non-interacting and interacting Fermi gas in both isotropic and anisotropic harmonic traps are illustrated in this section. Fig. 5.6 gives the nodal surface of the Fermi gas system of ten atoms in isotropic harmonic traps. The nodal surfaces are obtained by scanning the simulation with a pair of spin-up and spin-down atoms sitting on top of each other while keeping the rest atoms at fixed positions. From the figure, as the interaction is turned on, the nodal surface shrinks to pocket s around two closest atoms with different spins. Similarly Fig. 5.7 and Fig. 5.8 gives the nodal surface of the system in anisotropic harmonic traps with frequency ratio $\omega_\perp/\omega_z = 1/\sqrt{30}$ and $\omega_\perp/\omega_z = 1/25$, and the behaviour of nodal surface from non-interacting to interacting transition is similar to that of the isotropic cases.

## 5.3 Conclusion

In this Chapter, we have calculated ground state energies and density profiles of unpolarized Fermi gas in isotropic and anisotropic harmonic traps. For isotropic harmonic traps, we elucidated the discrepancy between previous calculated ground state energy using various methods. The differences between our extropolated DMC results and the latest lattice results are less than 3 percent. We calculated the ground state energies for the unpolarized Fermi gas in squeezed harmonic traps, which can be used by the experimentalist as a benchmark for the reduced dimension. We calculated the density profile and showed the failure of the local density approximation for the description of unitary Fermi gas in isotropic harmonic trap. We illustrate the nodal surface of the non-interacting and unitary Fermi gas for a given configuration and find that the attractive interaction reduces the node to smaller nodal pockets within nearest spin up and spin down atoms.

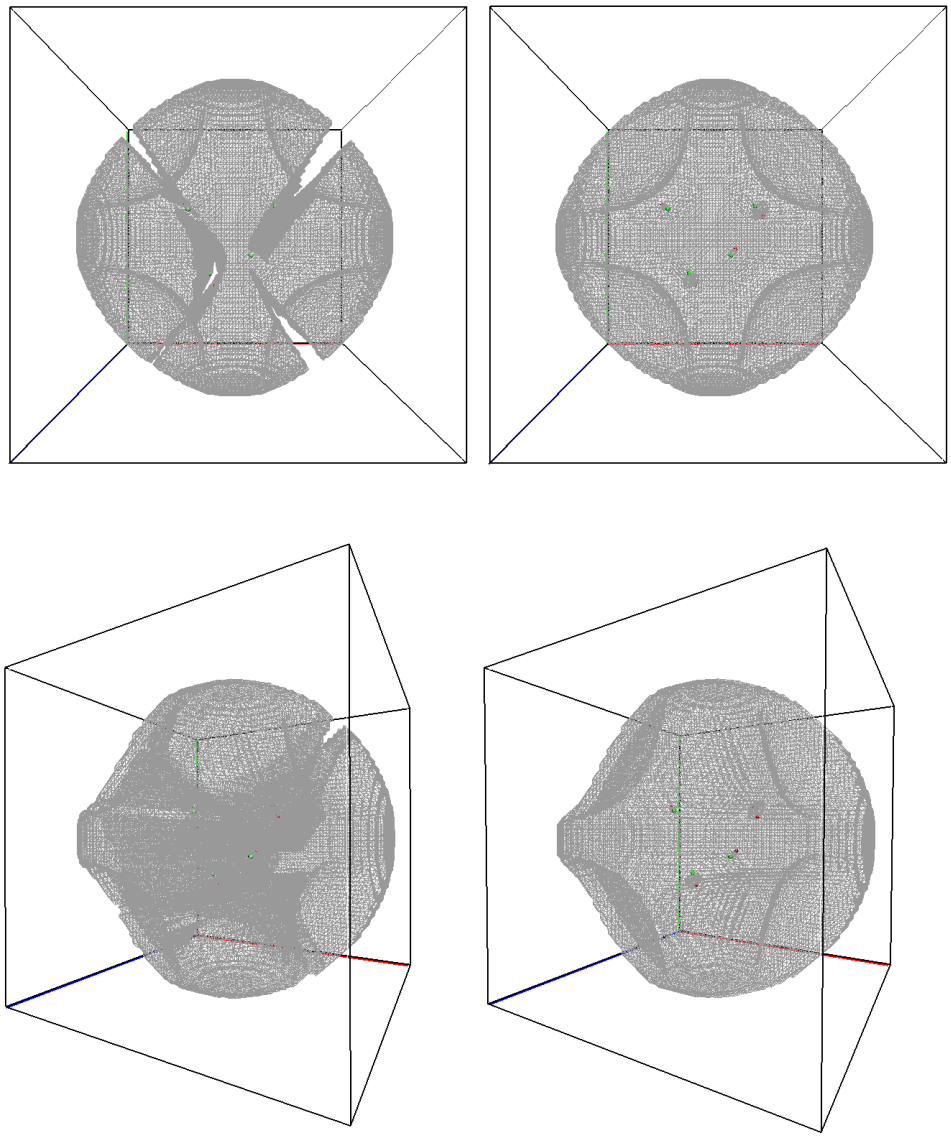

Figure 5.6: The nodal surface for non-interacting and unitary Fermi gas in isotropic harmonic trap. The figures on the left are for the non-interacting Fermi gas, and the figures on the right are for the unitary Fermi gas. The lower panel are the same graphs rotated by 45 degrees along z-axis.

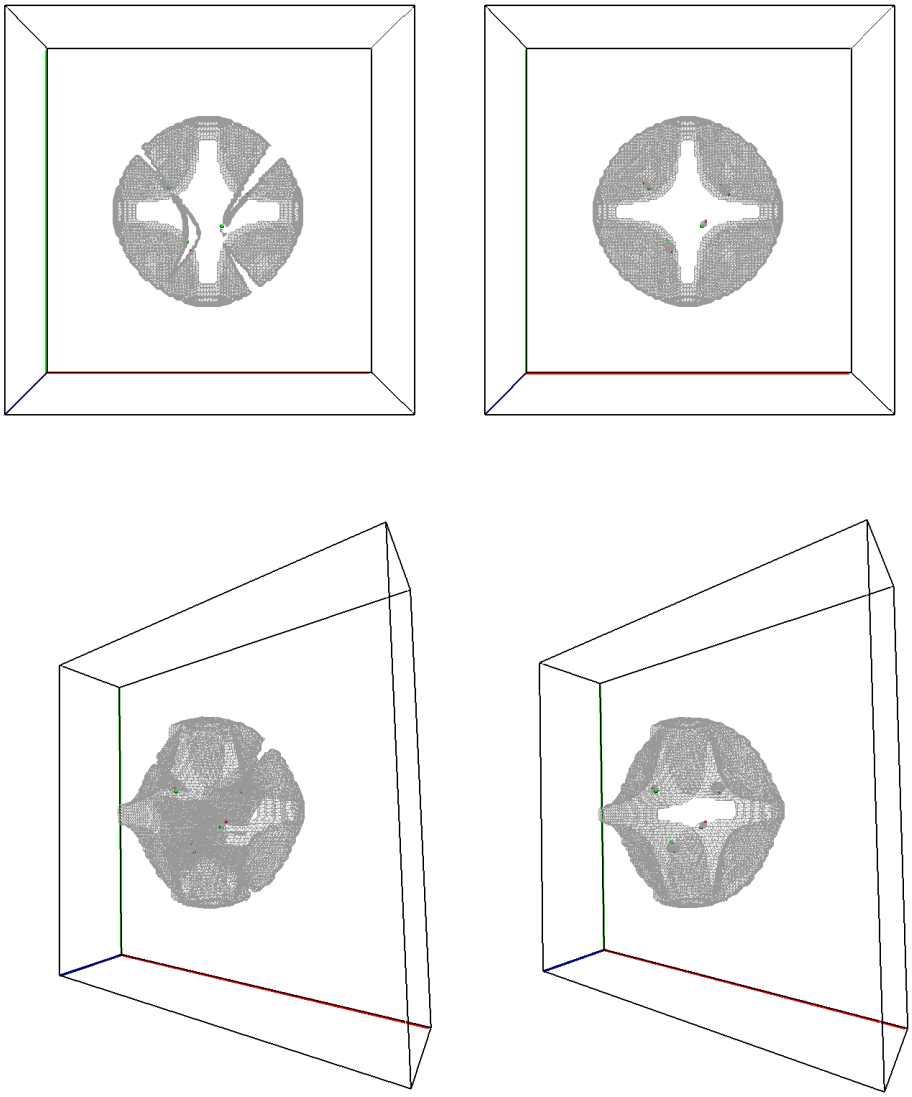

Figure 5.7: The nodal surface for non-interacting and unitary Fermi gas in anisotropic harmonic trap with $\omega_\perp/\omega_z = 1/\sqrt{30}$. The figures on the left are for the non-interacting Fermi gas, and the figures on the right are for the unitary Fermi gas. The lower panel are the same graphs rotated by 45 degrees along z-axis.

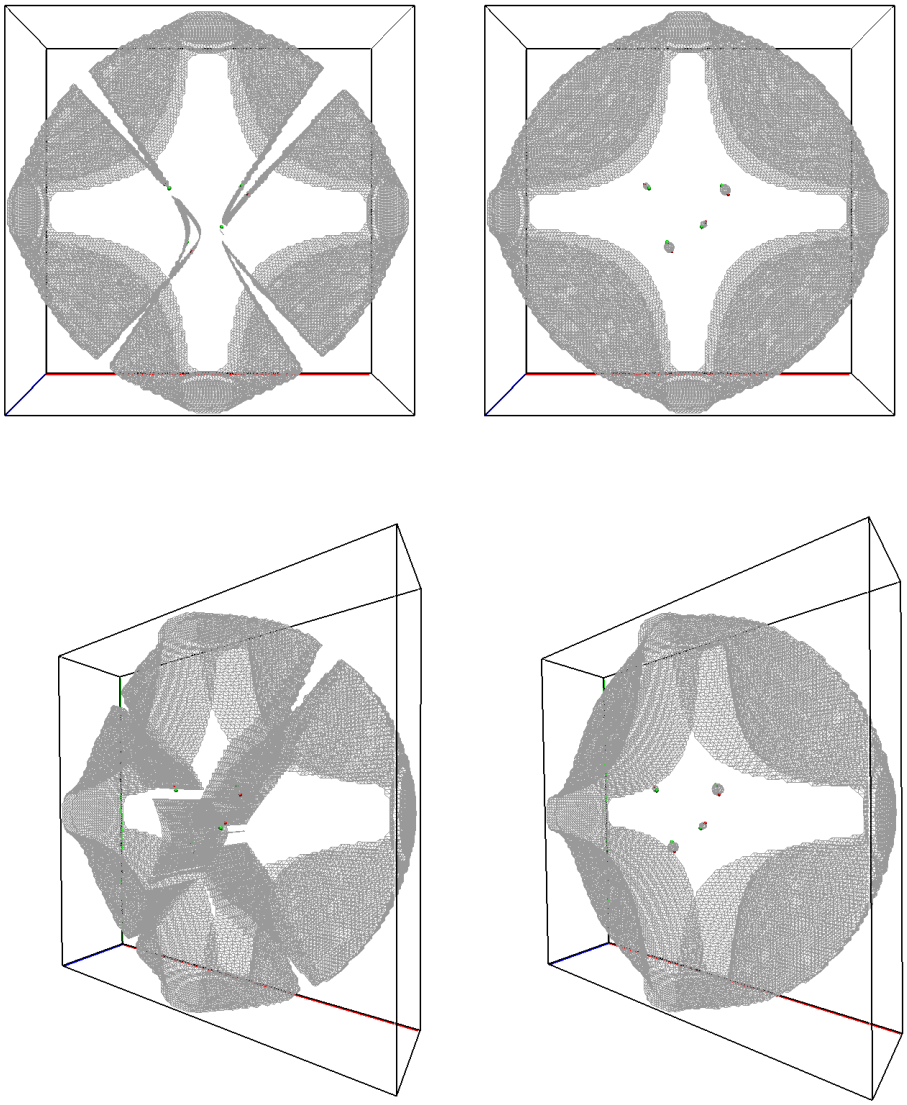

Figure 5.8: The nodal surface for non-interacting and unitary Fermi gas in anisotropic harmonic trap $\omega_\perp/\omega_z = 1/25$. The figures on the left are for the non-interacting Fermi gas, and the figures on the right are for the unitary Fermi gas, The lower panel are the same graphs rotated by 45 degrees along z-axis. Due to a weaker constrain on the x-y plane, the gas extended further on x-y plane compared with Fig. 5.7, as can be identified by the larger range of the nodal surface in the box.

# Chapter 6

# Summary and future work

## 6.1 Summary

The diffusion Monte Carlo method provides accurate strategy to calculate the ground state properties for the Fermi gas systems. With the only limitation of the fixed-node approximation, DMC provides an strict upper bound for the ground state energy and it also enables the calculation of various quantities related to the ground state for the dilute unpolarized Fermi gas system, which are the main research topic for this thesis.

After the introduction of the quantum Monte Carlo methods and related technique that has been used in this work in Chapter 2 and a brief theoretical introduction of the Fermi gas theory in Chapter 3, we use the quantum Monte Carlo methods to study unpolarized Fermi gas in the free space in a periodic box in Chapter 4. We have shown that in order to reach the unitary limit, the extrapolation of the effective range of the interaction to the zero range is necessary and due to this extrapolation, energy drops around 10 percent for four-atom system and around 5 percent for larger number atom system than previous DMC calculations without the extrapolation. We have carried out released-node DMC simulations for four-atom and fourteen-atom system and the signal of RN-DMC indicate the four-atom results are very accurate. For the fourteen-atom system, the released-node signals are able to detect the energy signal for the deliberately distorted nodal surface. Besides energy, a variety of quantities that relates to the ground state of unpolarized Fermi gas are calculated, including pair correlation function, one-body and two-body density matrices, condensate fraction and Tan's contact constant. We also illustrate the effect of effective range extrapolation on these quantities.

In Chapter 5, we have calculated the various ground state properties of unpolarized Fermi gas in isotropic and anisotropic harmonic traps. For isotropic harmonic traps, we solved the discrepancy between previous calculated results using various numerical methods. The differences

between our extropolated DMC results and the latest lattice results are less than 3 percent. We estimated the parameter for energy functional provided by an epsilon expansion and get more accurate parameter set than the previous results. We calculated the ground state energy for the unpolarized Fermi gas in squeezed harmonic traps, which can be used by the experimentalist as a benchmark for the reduced dimension. In addition to energy, we calculated the density profile and showed the failure of the local density approximation to describe the unitary Fermi gas in isotropic harmonic trap. We illustrate the nodal surface of the non-interacting and unitary Fermi gas for some configurations and find that the attractive interactions reduce the node to small nodal pocket within nearest spin-up and spin-down atoms.

## 6.2 Future work

The Fermi gas system provides a perfect test ground for the quantum many-body theory while quantum Monte Carlo simulations provide the opportunities to bridge the gap between the theory and experiment. Beyond current work, some new directions may be pursued as the future work using the quantum Monte Carlo methods.

- The spin imbalanced Fermi gas system. At the crossover regime, the spin imbalanced Fermi gas system is still not very well understood. The difference in the Fermi surface may lead to the pairing of spin-up and spin-down atoms with different amplitude of the wave vector, the so called Fulde-Ferrell-Larkin-Ovchinnikov (FFLO) state[45, 57]. It will be interesting to use diffusion Monte Carlo to decide the energy difference between different wave function to decide whether FFLO state signal can be captured.

- The p-wave superfluidity. For certain atomic species like $^{40}$K[46], p-wave Feshbach resonance may induce the formation of p-wave molecules. It will be very interesting to to study the phase diagram with different interaction strengths[49].

- Low-dimensional Fermi gas system. The BCS-BEC crossover in low-dimensional system such as 2D[14] and 1D may be studied systematically by diffusion Monte Carlo methods, including the physics of Luttinger liquid which may be studied further.

- Multi-component Fermi gas system. Three- and four-component Fermi gas systems will present unique feature of the Efimov state physics, the simple three-body and four-body binding of the Efimov state will provide the building block for the true many-body physics for the three- and four-component Fermi gas system, and quantum Monte Carlo is ready to explore the phase structure for these systems.

In conclusion, we have employed quantum Monte Carlo to study the unpolarized two component Fermi gas at unitary limit in free space and isotropic and anisotropic harmonic traps. The

quantum Monte Carlo methods will continue to play an active and sometimes essential role in the search, explanation, verification and prediction for both experimental and theoretical results for the Fermi gas system.

# REFERENCES


[1] T. Abe and R. Seki. From low-density neutron matter to the unitary limit. *Phys. Rev. C*, 79:054003, May 2009.

[2] T. Abe and R. Seki. Lattice calculation of thermal properties of low-density neutron matter with pionless *NN* effective field theory. *Phys. Rev. C*, 79:054002, May 2009.

[3] Mark G. Alford, Andreas Schmitt, Krishna Rajagopal, and Thomas Schäfer. Color superconductivity in dense quark matter. *Rev. Mod. Phys.*, 80:1455–1515, Nov 2008.

[4] G. E. Astrakharchik, J. Boronat, J. Casulleras, Giorgini, and S. Equation of state of a fermi gas in the bec-bcs crossover: A quantum monte carlo study. *Phys. Rev. Lett.*, 93:200404, Nov 2004.

[5] G. E. Astrakharchik and K. V. Krutitsky. Condensate fraction of cold gases in a nonuniform external potential. *Phys. Rev. A*, 84:031604, Sep 2011.

[6] M. Bajdich, L. Mitas, G. Drobný, L. K. Wagner, and K. E. Schmidt. Pfaffian pairing wave functions in electronic-structure quantum monte carlo simulations. *Phys. Rev. Lett.*, 96:130201, Apr 2006.

[7] M. Bajdich, L. Mitas, L. K. Wagner, and K. E. Schmidt. Pfaffian pairing and backflow wavefunctions for electronic structure quantum monte carlo methods. *Phys. Rev. B*, 77:115112, Mar 2008.

[8] Michal Bajdich. *Generalized Pairing Wave Functions and Nodal Properties for Electronic Structure Quantum Monte Carlo*. 2007.

[9] J. Bardeen, L. N. Cooper, and J. R. Schrieffer. Microscopic theory of superconductivity. *Phys. Rev.*, 106:162–164, Apr 1957.

[10] J. Bardeen, L. N. Cooper, and J. R. Schrieffer. Theory of superconductivity. *Phys. Rev.*, 108:1175–1204, Dec 1957.

[11] Stefano Baroni and Saverio Moroni. Reptation quantum monte carlo: A method for unbiased ground-state averages and imaginary-time correlations. *Phys. Rev. Lett.*, 82:4745–4748, Jun 1999.

[12] M. Bartenstein, A. Altmeyer, S. Riedl, S. Jochim, C. Chin, J. Hecker Denschlag, and R. Grimm. Crossover from a molecular bose-einstein condensate to a degenerate fermi gas. *Phys. Rev. Lett.*, 92:120401, Mar 2004.

[13] J. G. Bednorz and K. A. Mller. Possible high tc superconductivity in the balacuo system. *Zeitschrift fr Physik B Condensed Matter*, 64:189–193, 1986. 10.1007/BF01303701.

[14] G. Bertaina and S. Giorgini. Bcs-bec crossover in a two-dimensional fermi gas. *Phys. Rev. Lett.*, 106:110403, Mar 2011.

[15] R. Blankenbecler, D. J. Scalapino, and R. L. Sugar. Monte carlo calculations of coupled boson-fermion systems. i. *Phys. Rev. D*, 24:2278–2286, Oct 1981.

[16] Immanuel Bloch, Jean Dalibard, and Wilhelm Zwerger. Many-body physics with ultracold gases. *Rev. Mod. Phys.*, 80:885–964, Jul 2008.

[17] Shahin Bour, Xin Li, Dean Lee, Ulf-G. Meißner, and Lubos Mitas. Precision benchmark calculations for four particles at unitarity. *Phys. Rev. A*, 83:063619, Jun 2011.

[18] T. Bourdel, J. Cubizolles, L. Khaykovich, K. M. F. Magalhães, S. J. J. M. F. Kokkelmans, G. V. Shlyapnikov, and C. Salomon. Measurement of the interaction energy near a feshbach resonance in a $^6$Li fermi gas. *Phys. Rev. Lett.*, 91:020402, Jul 2003.

[19] T. Bourdel, L. Khaykovich, J. Cubizolles, J. Zhang, F. Chevy, M. Teichmann, L. Tarruell, S. J. J. M. F. Kokkelmans, and C. Salomon. Experimental study of the bec-bcs crossover region in lithium 6. *Phys. Rev. Lett.*, 93:050401, Jul 2004.

[20] Henrik Bruus and Karsten Flensberg. *Many-Body Quantum Thoery in Condensed Matter Physics*. Oxford University Press, 2004.

[21] Aurel Bulgac, Joaquin E. Drut, and Piotr Magierski. Quantum monte carlo simulations of the bcs-bec crossover at finite temperature. *Phys. Rev. A*, 78:023625, Aug 2008.

[22] J. Carlson, S.-Y. Chang, V. R. Pandharipande, and K. E. Schmidt. Superfluid fermi gases with large scattering length. *Phys. Rev. Lett.*, 91:050401, Jul 2003.

[23] J. Carlson, Stefano Gandolfi, Kevin E. Schmidt, and Shiwei Zhang. Auxiliary-field quantum monte carlo method for strongly paired fermions. *Phys. Rev. A*, 84:061602, Dec 2011.

[24] J. Casulleras and J. Boronat. Progress in monte carlo calculations of fermi systems: Normal liquid $^3$*he*. *Phys. Rev. Lett.*, 84:3121–3124, Apr 2000.

[25] D. M. Ceperley. Fermion nodes. *Journal of Statistical Physics*, 63:1237–1267, 1991. 10.1007/BF01030009.

[26] D. M. Ceperley. Path integrals in the theory of condensed helium. *Rev. Mod. Phys.*, 67:279–355, Apr 1995.

[27] D. M. Ceperley and B. J. Alder. Ground state of the electron gas by a stochastic method. *Phys. Rev. Lett.*, 45:566–569, Aug 1980.

[28] David Ceperley, M. H. Kalos, and Joel L. Lebowitz. Computer simulation of the static and dynamic properties of a polymer chain. *Macromolecules*, 14(5):1472–1479, 1981.

[29] Kalos M.H. Ceperley, D.M. *Monte Carlo Methods in Statistical Physics, 2nd ed.* Springer(Berlin), edited by K. Binder, 1979.

[30] S. Y. Chang and G. F. Bertsch. Unitary fermi gas in a harmonic trap. *Phys. Rev. A*, 76:021603, Aug 2007.

[31] S. Y. Chang and V. R. Pandharipande. Ground-state properties of fermi gases in the strongly interacting regime. *Phys. Rev. Lett.*, 95:080402, Aug 2005.

[32] Cheng Chin, Rudolf Grimm, Paul Julienne, and Eite Tiesinga. Feshbach resonances in ultracold gases. *Rev. Mod. Phys.*, 82:1225–1286, Apr 2010.

[33] Leon N. Cooper. Bound electron pairs in a degenerate fermi gas. *Phys. Rev.*, 104:1189–1190, Nov 1956.

[34] K. B. Davis, M. O. Mewes, M. R. Andrews, N. J. van Druten, D. S. Durfee, D. M. Kurn, and W. Ketterle. Bose-einstein condensation in a gas of sodium atoms. *Phys. Rev. Lett.*, 75:3969–3973, Nov 1995.

[35] D. J. Dean and M. Hjorth-Jensen. Pairing in nuclear systems: from neutron stars to finite nuclei. *Rev. Mod. Phys.*, 75:607–656, Apr 2003.

[36] B. DeMarco and D. S. Jin. Onset of fermi degeneracy in a trapped atomic gas. *Science*, 285(5434):1703–1706, 1999.

[37] J. L. DuBois and H. R. Glyde. Bose-einstein condensation in trapped bosons: A variational monte carlo analysis. *Phys. Rev. A*, 63:023602, Jan 2001.

[38] Michael G. Endres, David B. Kaplan, Jong-Wan Lee, and Amy N. Nicholson. Lattice monte carlo calculations for unitary fermions in a harmonic trap. *Phys. Rev. A*, 84:043644, Oct 2011.

[39] Kenneth P. Esler. http://einspline.sourceforge.net/.

[40] U. Fano. Effects of configuration interaction on intensities and phase shifts. *Phys. Rev.*, 124:1866–1878, Dec 1961.

[41] Herman Feshbach. A unified theory of nuclear reactions. ii. *Annals of Physics*, 19(2):287 – 313, 1962.

[42] S. Flu̇gge. *Practical Quantum Mechanics I*. Springer-Verlag, Berlin-Heidelberg(New York), 1971.

[43] Michael McNeil Forbes, Stefano Gandolfi, and Alexandros Gezerlis. Resonantly interacting fermions in a box. *Phys. Rev. Lett.*, 106:235303, Jun 2011.

[44] W. M. C. Foulkes, L. Mitas, R. J. Needs, and G. Rajagopal. Quantum monte carlo simulations of solids. *Rev. Mod. Phys.*, 73:33–83, Jan 2001.

[45] Peter Fulde and Richard A. Ferrell. Superconductivity in a strong spin-exchange field. *Phys. Rev.*, 135:A550–A563, Aug 1964.

[46] J. P. Gaebler, J. T. Stewart, J. L. Bohn, and D. S. Jin. $p$-wave feshbach molecules. *Phys. Rev. Lett.*, 98:200403, May 2007.

[47] Stefano Giorgini, Lev P. Pitaevskii, and Sandro Stringari. Theory of ultracold atomic fermi gases. *Rev. Mod. Phys.*, 80:1215–1274, Oct 2008.

[48] Paola Gori-Giorgi, Francesco Sacchetti, and Giovanni B. Bachelet. Analytic static structure factors and pair-correlation functions for the unpolarized homogeneous electron gas. *Phys. Rev. B*, 61:7353–7363, Mar 2000.

[49] V. Gurarie and L. Radzihovsky. Resonantly paired fermionic superfluids. *Annals of Physics*, 322(1):2 – 119, 2007.

[50] Kerson Huang and C. N. Yang. Quantum-mechanical many-body problem with hard-sphere interaction. *Phys. Rev.*, 105:767–775, Feb 1957.

[51] S. Inouye, M. R. Andrews, J. Stenger, H. J. Miesner, D. M. Stamper-Kurn, and W. Ketterle. Observation of feshbach resonances in a boseeinstein condensate. *Nature*, 392:151, 1998.

[52] J. Joseph, B. Clancy, L. Luo, J. Kinast, A. Turlapov, and J. E. Thomas. Measurement of sound velocity in a fermi gas near a feshbach resonance. *Phys. Rev. Lett.*, 98:170401, Apr 2007.

[53] E. D. Kuhnle, H. Hu, X.-J. Liu, P. Dyke, M. Mark, P. D. Drummond, P. Hannaford, and C. J. Vale. Universal behavior of pair correlations in a strongly interacting fermi gas. *Phys. Rev. Lett.*, 105:070402, Aug 2010.

[54] L. D. Landau. *Sov. Phys. JETP*, 3:920, 1957.

[55] L. D. Landau. *Sov. Phys. JETP*, 5:101, 1957.

[56] L. D. Landau. *Sov. Phys. JETP*, 8:70, 1958.

[57] A. I. Larkin and Ovchinnikov Yu. N. Inhomogeneous state of superconductors. *Sov. Phys. JETP.*, 20:762–769, Mar 1965.

[58] Dean Lee. Ground state energy at unitarity. *Phys. Rev. C*, 78:024001, Aug 2008.

[59] T. D. Lee and C. N. Yang. Many-body problem in quantum mechanics and quantum statistical mechanics. *Phys. Rev.*, 105:1119–1120, Feb 1957.

[60] X. Leyronas and R. Combescot. Superfluid equation of state of dilute composite bosons. *Phys. Rev. Lett.*, 99:170402, Oct 2007.

[61] Xin Li, Jindřich Kolorenč, and Lubos Mitas. Atomic fermi gas in the unitary limit by quantum monte carlo methods: Effects of the interaction range. *Phys. Rev. A*, 84:023615, Aug 2011.

[62] Le Luo and J. Thomas. Thermodynamic measurements in a strongly interacting fermi gas. *Journal of Low Temperature Physics*, 154:1–29, 2009. 10.1007/s10909-008-9850-2.

[63] A. J. Moerdijk and B. J. Verhaar. Prospects for bose-einstein condensation in atomic $^{7}$Li and $^{23}$Na. *Phys. Rev. Lett.*, 73:518–521, Jul 1994.

[64] Andrew J. Morris, P. López Ríos, and R. J. Needs. Ultracold atoms at unitarity within quantum monte carlo methods. *Phys. Rev. A*, 81:033619, Mar 2010.

[65] N. Navon, S. Nascimbne, F. Chevy, and C. Salomon. The equation of state of a low-temperature fermi gas with tunable interactions. *Science*, 328(5979):729–732, 2010.

[66] Marshall N. Rosenbluth Augusta H. Teller Nicholas Metropolis, Arianna W. Rosenbluth1 and Edward Teller. Equation of state calculations by fast computing machines. *J. Chem. Phys.*, 21:1087–1092, 1953.

[67] K. M. O'Hara, S. L. Hemmer, M. E. Gehm, S. R. Granade, and J. E. Thomas. Observation of a strongly interacting degenerate fermi gas of atoms. *Science*, 298(5601):2179–2182, 2002.

[68] D. D. Osheroff, R. C. Richardson, and D. M. Lee. Evidence for a new phase of solid $he^3$. *Phys. Rev. Lett.*, 28:885–888, Apr 1972.

[69] Guthrie B. Partridge, Wenhui Li, Ramsey I. Kamar, Yean-an Liao, and Randall G. Hulet. Pairing and phase separation in a polarized fermi gas. *Science*, 311(5760):503–505, 2006.

[70] P. Reynolds, D. M. Ceperley, Berni. Alder, and A. L. William. Fixednode quantum monte carlo for molecules. *Journal of Chemical Physics*, 77:5593, 1982.

[71] Gautam Rupak and Thomas Sch˙Density functional theory for non-relativistic fermions in the unitarity limit. *Nuclear Physics A*, 816(14):52 – 64, 2009.

[72] Shina Tan. Energetics of a strongly correlated fermi gas. *Annals of Physics*, 323(12):2952 – 2970, 2008.

[73] Shina Tan. Generalized virial theorem and pressure relation for a strongly correlated fermi gas. *Annals of Physics*, 323(12):2987 – 2990, 2008.

[74] Shina Tan. Large momentum part of a strongly correlated fermi gas. *Annals of Physics*, 323(12):2971 – 2986, 2008.

[75] C. J. Umrigar. Accelerated metropolis method. *Phys. Rev. Lett.*, 71:408–411, Jul 1993.

[76] C. J. Umrigar and Claudia Filippi. Energy and variance optimization of many-body wave functions. *Phys. Rev. Lett.*, 94:150201, Apr 2005.

[77] J. von Stecher, Chris H. Greene, and D. Blume. Energetics and structural properties of trapped two-component fermi gases. *Phys. Rev. A*, 77:043619, Apr 2008.

[78] Félix Werner and Yvan Castin. Unitary gas in an isotropic harmonic trap: Symmetry properties and applications. *Phys. Rev. A*, 74:053604, Nov 2006.

[79] C. N. Yang. Concept of off-diagonal long-range order and the quantum phases of liquid he and of superconductors. *Rev. Mod. Phys.*, 34:694–704, Oct 1962.

[80] Shiwei Zhang and D. M. Ceperley. Hartree-fock ground state of the three-dimensional electron gas. *Phys. Rev. Lett.*, 100:236404, Jun 2008.

[81] M. Zwierlein. Unpulished.

# APPENDICES

# Appendix A

# Conversion factor table for unpolarized Fermi gas

In the calculation of the non-interaction energy for unpolarized Fermi gas in a periodic box, two different methods are used and sometimes can cause confusion. In our work, we directly fill the k points for a periodic box and denote the resulting energy $E_{\mathrm{NI}}$. In the literature, the approximated energy by considering the k points as continuous is also used,

$$E_{\mathrm{NIthermo}} = \frac{3}{5} N E_F, \tag{A.1}$$

where $E_{\mathrm{NIthermo}}$ is the non-interacting energy for the thermodynamic limit, $N$ is the atom number and $E_F$ is the Fermi energy which can be written as Fermi wave vector,

$$E_F = \frac{\hbar^2 k_F^2}{2m} = \frac{\hbar^2}{2m}(3\pi^2 N/V)^{2/3}. \tag{A.2}$$

The conversion factor for the Bertsch parameter from two methods can be readily obtained as

$$\frac{\xi}{\xi_{\mathrm{thermo}}} = \frac{E_{\mathrm{NIthermo}}}{E_{\mathrm{NI}}}. \tag{A.3}$$

The conversion factor up to 66 atoms is shown in Table A.1. For larger number of atoms the difference is rather minor .

Table A.1: Conversion factor for unpolarized Fermi gas. For simplicity, the calculation is performed in a periodic box with size $L = 1$

| N | $E_{\mathrm{NI}}$ | $E_{\mathrm{NIthermo}}$ | $\frac{E_{\mathrm{NIthermo}}}{E_{\mathrm{NI}}}$ |
|---|---|---|---|
| 4 | 39.4784 | 28.9402 | 0.7331 |
| 6 | 78.9568 | 56.8836 | 0.7204 |
| 8 | 118.435 | 91.8795 | 0.7758 |
| 10 | 157.913 | 133.271 | 0.8440 |
| 12 | 197.392 | 180.594 | 0.9149 |
| 14 | 236.871 | 233.497 | 0.9858 |
| 16 | 315.828 | 291.699 | 0.9236 |
| 18 | 394.784 | 354.968 | 0.8991 |
| 20 | 473.742 | 423.109 | 0.8931 |
| 22 | 552.698 | 495.952 | 0.8967 |
| 24 | 631.655 | 573.351 | 0.9077 |
| 26 | 710.612 | 655.175 | 0.9220 |
| 38 | 1184.35 | 1233.22 | 1.0413 |
| 54 | 2131.83 | 2215.09 | 1.0391 |
| 66 | 3079.31 | 3094.87 | 1.0047 |

# Appendix B

# Energy of non-interacting Fermi gas in isotropic and anisotropic harmonic traps

This Appendix provides non-interacting energies for small number of atoms in isotropic and anisotropic harmonic traps for quick look-up. For the anisotropic harmonic trap, we assume $\omega_x = \omega_y \ll \omega_z$. Due to the frequency difference in z direction, the shell number for isotropic and anisotropic harmonic traps are different. The atom number for first several shells for symmetric harmonic trap is 2, 8, 20, 40, 70, etc., and for ansymmetric harmonic trap is 2, 6, 12, 20, 30, 42, etc.

Table B.1: Energy of N non-interacting unpolarized Fermi atoms in isotropic harmonic trap ($\hbar = 1$, $\omega_x = \omega_y = \omega_z = \omega$).

| N | $E_{NI}$ |
|---|---|
| 2 | $(1/2\omega_x + 1/2\omega_y + 1/2\omega_z) * 2 = 3\omega$ |
| 4 | $E_2 + ((1 + 1/2)\omega_x + 1/2\omega_y + 1/2\omega_z) * 2) = 8\omega$ |
| 6 | $E_4 + (1/2\omega_x + (1 + 1/2)\omega_y + 1/2\omega_z) * 2) = 13\omega$ |
| 8 | $E_6 + (1/2\omega_x + 1/2\omega_y + (1 + 1/2)\omega_z) * 2 = 18\omega$ |
| 10 | $E_8 + ((1 + 1/2)\omega_x + (1 + 1/2)\omega_y + 1/2\omega_z) * 2 = 25\omega$ |
| 12 | $E_{10} + ((1 + 1/2)\omega_x + 1/2\omega_y + (1 + 1/2)\omega_z) * 2 = 32\omega$ |
| 16 | $E_{12} + 2 * ((2 + 1/2)\omega_x + 1/2\omega_y + 1/2\omega_z) * 2 = 46\omega$ |
| 20 | $E_{16} + (1/2\omega_x + (2 + 1/2)\omega_y + 1/2\omega_z) * 2 + (1/2\omega_x + 1/2\omega_y + (2 + 1/2)\omega_z) * 2 = 60\omega$ |
| 24 | $E_{20} + ((3 + 1/2)\omega_x + 1/2\omega_y + 1/2\omega_z) * 2 + (1/2\omega_x + (3 + 1/2)\omega_y + 1/2\omega_z) * 2 = 78\omega$ |
| 36 | $E_{24} + 6 * (1/2\omega_x + 1/2\omega_y + (3 + 1/2)\omega_z) * 2 = 132\omega$ |
| 40 | $E_{36} + 2 * (1 + 1/2)\omega_x + (1 + 1/2)\omega_y + (1 + 1/2)\omega_z) * 2 = 150\omega$ |

Table B.2: Energy of N non-interacting unpolarized Fermi atoms in anisotropic harmonic trap ($\hbar = 1$, $\omega_x = \omega_y = \omega_\perp \ll \omega_z$).

| N | $E_{NI}$ |
|---|---|
| 2 | $(1/2\omega_x + 1/2\omega_y + 1/2\omega_z) * 2 = 2\omega_\perp + \omega_z$ |
| 4 | $E_2 + ((1 + 1/2)\omega_x + 1/2\omega_y + 1/2\omega_z) * 2) = 6\omega_\perp + 2\omega_z$ |
| 6 | $E_4 + (1/2\omega_x + (1 + 1/2)\omega_y + 1/2\omega_z) * 2) = 10\omega_\perp + 3\omega_z$ |
| 8 | $E_6 + ((2 + 1/2)\omega_x + 1/2\omega_y + 1/2\omega_z) * 2 = 16\omega_\perp + 4\omega_z$ |
| 10 | $E_8 + (1/2\omega_x + (2 + 1/2)\omega_y + 1/2\omega_z) * 2 = 22\omega_\perp + 5\omega_z$ |
| 12 | $E_{10} + ((1 + 1/2)\omega_x + (1 + 1/2)\omega_y + 1/2\omega_z) * 2 = 28\omega_\perp + 6\omega_z$ |
| 16 | $E_{12} + 2 * ((3 + 1/2)\omega_x + 1/2\omega_y + 1/2\omega_z) * 2 = 44\omega_\perp + 8\omega_z$ |
| 20 | $E_{16} + 2 * ((2 + 1/2)\omega_x + (1 + 1/2)\omega_y + 1/2\omega_z) * 2 = 60\omega_\perp + 10\omega_z$ |
| 24 | $E_{20} + 2 * (1/2\omega_x + (4 + 1/2)\omega_y + 1/2\omega_z) * 2 = 80\omega_\perp + 12\omega_z$ |
| 36 | $E_{24} + 6 * ((3 + 1/2)\omega_x + (1 + 1/2)\omega_y + \omega_z) * 2 = 146\omega_\perp + 18\omega_z$ |
| 40 | $E_{36} + (1 + 1/2)\omega_x + (1 + 1/2)\omega_y + (1 + 1/2)\omega_z) * 2 = 170\omega_\perp + 20\omega_z$ |